T-3834

MECHANISMS OF COATING FAILURES DURING DEEP DRAWING OF COATED SHEET STEELS

BY:

SCOTT HOWARD DEITS

A thesis submitted to the faculty and the Board of Trustees of the Colorado School of Mines in partial fulfillment of the requirements for the degree of Masters of Science, Metallurgical Engineering.

Golden, Colorado

Date MARCH 2, 1990

Signed

Scott H. Deits

Approved:

Dr. David K. Matlock

Thesis Advisor

Golden, Colorado

Date MARCH 2, 1990

Dr. John J. Moore

Department Chairman

Metallurgical and Materials Engineering

ABSTRACT

The deformation characteristics of pure zinc and zinc-iron alloy coatings were investigated during laboratory deep drawing of coated sheet steels. The coatings investigated were: three electrogalvanized, a hot dip, a galvannealed and a electrodeposited zinc-iron alloy. The lubricated sheet steels were drawn into cylindrical flat bottom cups, two inches in diameter. Cup drawing provided a change in stress and strain states which were utilized to characterize the deformation behavior of the coating.

A FEM analysis that simulated cup drawing as a function of position through the thickness of the sheet characterized the stress states on both surfaces of the sheet during deformation. This analysis shows significant stress gradients through the sheet thickness, observations which are different from conventional membrane analysis. The calculated surface stresses of the sheet steel were used in conjunction with the scanning electron microscopic observations of the deformed coating to evaluate the deformation characteristics of the coatings.

The deformation behaviors of the pure zinc coatings were dependent on the coating texture. Two electrogalvanized coatings with similar textures

plastically deformed to accommodate substrate strain. However, the third electrogalvanized coating with significantly different texture cracked to accommodate substrate strain. Different crystallographic texture orientation within spangles of the hot dip coating resulted in inter- and intra-spangular cracking to accommodate substrate strain.

The zinc-iron alloys accommodated tensile strains by cracking and subsequent compressive strains enhanced flaking. The cracks in the coating nucleated at the coating/substrate interface and propagated towards the surface.

Four modes of coating failure were observed and identified as Powdering, Flaking, Galling and Cracking. Enhanced definitions of each failure mode were developed.

TABLE OF CONTENTS

LIST OF FIGURES

	Description	Page

Description Page

LIST OF TABLES

ACKNOWLEDGMENTS

The author would like to express his sincere appreciation to the following people associated with his thesis:

to Dr. Matlock for his intuitive guidance throughout this thesis and for the drive to educate students,

to Dr. Van Tyne for his work with the FEM analysis and suggestions,

to Dr. Krauss for his refreshing attitude and suggestions,

to Steve Donaldson for fabricating the testing apparatus,

to the computing center for their cooperation with the FEM analysis,

and to Linda for all of her support.

1.0 INTRODUCTION

1.1 Sheet Metal Formability and Testing

Sheet steels are used for many applications, however the major usage is for automotive body panels. Sheet metal is desirable for these products because the original flat sheet can be formed into complex shapes at high forming rates. When formed sheets are used on a product, such as an automobile, the product can encounter adverse environments which deteriorate the sheet steel. The environmental deterioration, or corrosion of the sheet, can lead to premature failure. To decrease the rate of corrosion, coatings are applied to prolong the useful life of the sheet metal product. The primary coatings of interest include organic products which provide a barrier protection and metallic coatings which provide both barrier and galvanic protection. Several metallic coatings will protect the iron substrate, however, zinc has been found to be a favorable coating due to good galvanic protection and formability [1]. While corrosion protection is the main objective of coated sheet steels, other factors such as formability, weldability, press shop performance and finish characteristics need to be considered.

Application of the coatings is performed as a final step in the production of the sheet steel prior to coiling. As a result of the presence of the coatings, press shop performance of the sheet during forming has been altered in comparison to the uncoated sheet steel [1,2]. Otterberg [3], showed the effects of different coatings on the drawability of coated sheet steels. The maximum deep drawing depth of several coated sheet steels is plotted against the hardness of the coatings in Figure 1 as determined by Otterberg. Harder zinc-alloy coatings result in reduced drawing depths. The changes in formability due to the presence of the coating can be attributed to differences in thermal and mechanical processing, frictional characteristics and coating damage [4].

The mechanisms responsible for coating damage during forming are the primary focus of this thesis. Before evaluating the effects of differences in formability of coated sheet steel it is important to understand the processing and formability of the uncoated substrate. The sheet steel substrate influences overall formability due to mechanical properties such as ductility, work hardening, and plastic anisotropy, which determine the ability of the steel to withstand strain during forming. The characteristics of the coating can influence forming because the coating can affect metal flow over tool and die

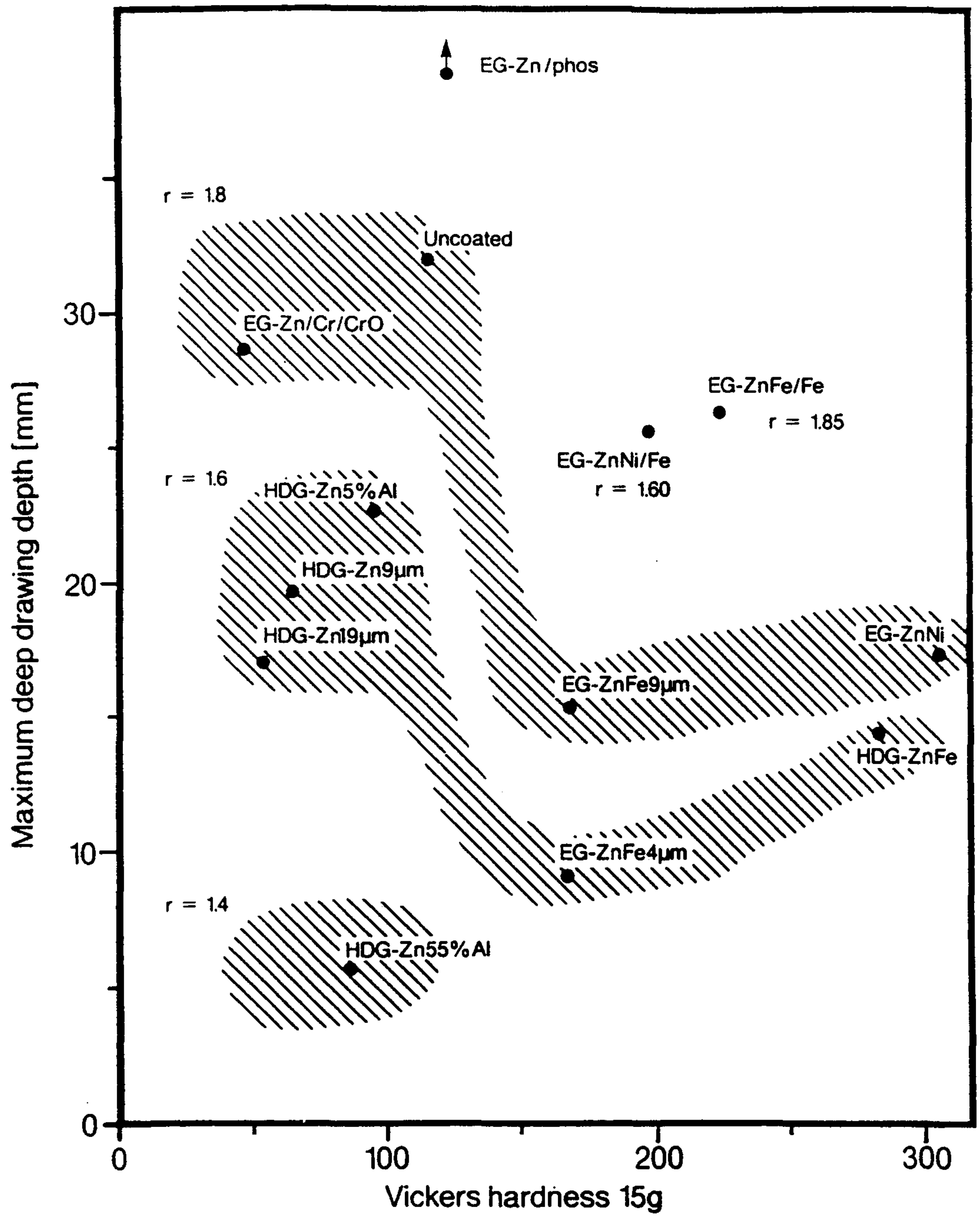

Figure 1 Relationship of maximum drawing depth of sheet steels with various coatings as a function of the coating hardness [3].

surfaces [1].

Sheet steel substrates with specific compositions and processing conditions can be separated into four general categories: commercial quality (CQ), drawing quality (DQ), drawing quality special-killed or aluminum-killed (DQSK or DQAK), and High Strength [1]. The CQ sheet steel has the least restrictions during processing. These steels are produced from either ingot-cast rimmed and capped steels or from ingot- or continuously- cast aluminum-killed steels. The DQ steels are made to compositions and processing conditions more restrictive than those used for CQ steels. The DQAK sheet steels can be subdivided into categories based on carbon content. Low carbon steels (0.015 to 0.15 percent carbon) are either in-line annealed or pre-box annealed and post box annealed. Extra low carbon steels (0.002 to 0.015 percent carbon) are either stabilized (interstitial-free) or non-stabilized steels. The interstitial-free steels have alloy additions which combine with the relatively few carbon atoms. The high strength steels have additions of strengthening agents such as phosphorus, manganese, niobium, vanadium or titanium, resulting in higher yield strengths, tensile strengths and lower ductility. Coatings are applied to all types of substrate to provide corrosion protection.

1.1.1 Factors Affecting Formability.

Formability may be defined as the ability of a material to assume a specified form, shape or pattern [5]. This broad definition of formability indicates that many underlying factors influence the ability of a sheet to be formed into a desired shape. This section will discuss the parameters affecting formability.

A standard test which evaluates mechanical properties affecting formability is the tensile test in which sheet steel with specified dimensions is deformed in uniaxial tension. During the test, load and displacement are monitored simultaneously. The shape of the resulting load versus displacement curve can vary depending on the material properties. Usually, five material properties are reported from tensile testing; the yield stress, ultimate tensile strength, percent uniform elongation, percent total elongation and strain hardening exponent. The ultimate tensile strength and percent uniform elongation are determined at the onset of instability. If the material being formed exceeds the instability criteria, non-uniform thinning or necking will occur. The onset of necking will begin with diffuse necking followed by localized necking. Diffuse necking is a process in which the material nonuniformly thins over a broad region. Localized necking however, is limited to a small area usually related to a reduction in thickness and progresses rapidly to failure [6].

Tensile test results are for uniaxial tensile stress and strain states. However, most forming operations have more complex stress and strain states. To evaluate the formability of a material under the more complex strain states, the forming limit diagram has been developed. The forming limit diagram is a representation of the strain state to which a material can be deformed prior to localized necking. The strain values are plotted as the minor strain e_2 versus the major strain e_1. A typical forming limit diagram for aluminum-killed sheet steel is shown in Figure 2. A combination of strain values above the solid line in Figure 2 results in failure of the sheet steel.

To prevent the the onset of localized necking it is important to have a material with a strength in the thickness direction greater than the strength in the plane of the sheet. The plastic strain ratio, r, is a measure of resistance to through thickness thinning and is defined by the following relationship;

$$r=\ln(w_o/w)/\ln(h_o/h) \qquad (1)$$

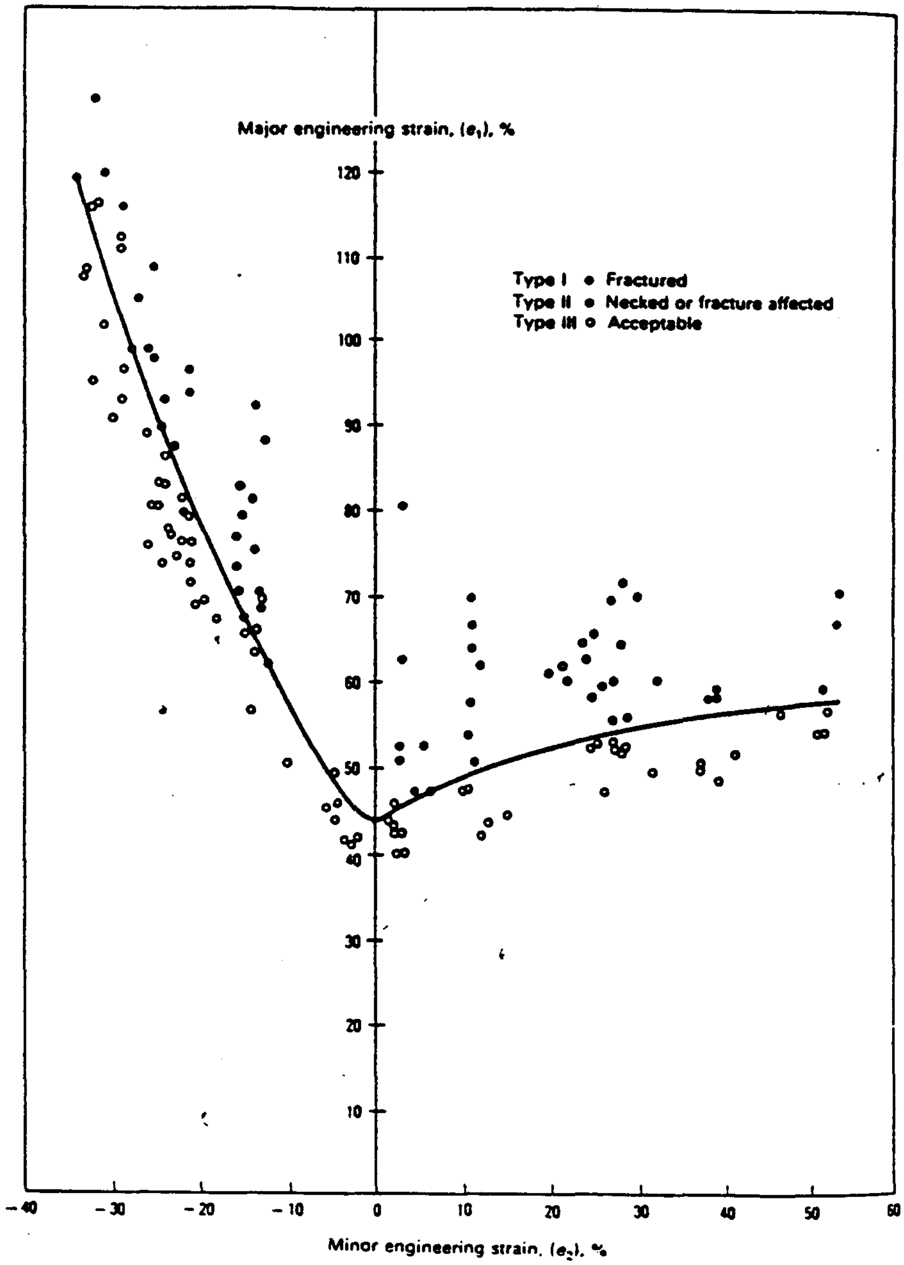

Figure 2 Forming limit diagram for aluminum-killed sheet steel [7].

where, w_o and w are the initial and final width and h_o and h are the initial and final thickness.

For conditions of deep drawing, high r-values are desired (r>1.5)[8]. The values of r can change with respect to orientation in the plane of the rolled sheet. To obtain a representative plastic strain ratio, r-values are obtained in different orientations in the sheet and reported as an average plastic strain ratio or $\bar{r}$,

$$\bar{r}=1/4(r_0+2r_{45}+r_{90}) \tag{2}$$

where, r_0 is determined in the rolling direction, r_{45} is determined 45 degrees to the rolling direction, and r_{90} is determined transverse to the rolling direction. To obtain high $\bar{r}$ values in aluminum-killed steels, the hot rolling of the sheet must be performed in the austenitic phase above the recrystallization temperature, followed by rapid cooling to low coiling temperatures and final cold reductions of 60-75% [8]. Annealing below the A_1 temperature after cold work causes the precipitation of AlN at cell and ferrite grain boundaries. The precipitation of AlN inhibits nucleation sites for recrystallization and causes anisotropic growth of recrystallized grains. This process develops a texture or preferred orientation of {111} planes parallel to the sheet with a slip direction <110> parallel to the rolling direction, a texture which optimizes $\bar{r}$ and enhances formability [8,9].

Another important relationship with the orientation of properties within the sheet is a measure of the planar anisotropy, Δr,

$$\Delta r=(r_0-2r_{45}+r_{90})/2 \quad (3)$$

where r_0, r_{45}, and r_{90} have been defined previously. This parameter is important in drawing operations and describes the type of earing which will develop. Earing is a result of preferential sheet steel elongation in one direction more than others during drawing. The effects of earing are shown in Figure 3. When $\Delta r>0$, ears form at 0 and 90 degrees to the rolling direction. When $\Delta r<0$, ears form at orientations close to 45 degrees to the rolling direction. A Δr of zero indicates an isotropic material which will not develop earing [10]. Depending on the geometry of the final part, earing may require excessive trimming of the sheet to obtain the required shape. Even though the $\bar{r}$ value may be high, if Δr deviates substantially from zero the sheet steel may not be appropriate for proper formability.

The flow behavior during plastic deformation will also effect formability. If a sheet steel exhibits continuous yielding during deformation the flow characteristics can be

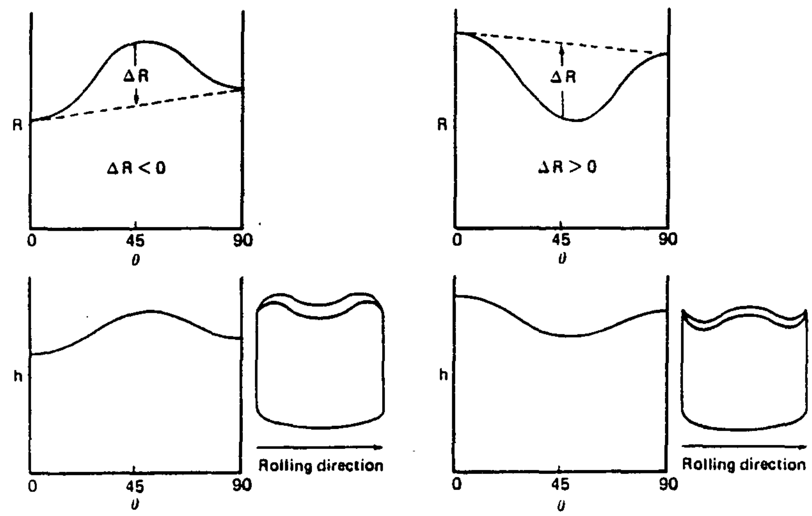

Figure 3 Relationship between planar anisotropy and the development of earing during drawing for two ranges in Δr [10].

approximated by a power law function. The strain hardening exponent of the power law function, n, is equal to the uniform elongation. However, some materials exhibit discontinuous yielding or Luders strain. Deformation past Luders strain will follow a strain hardening behavior. Luders strain can leave surface defects undesirable for finish characteristics, and eliminate Luders strain the sheet steel can be temper rolled to a strain level where continuous yielding will occur with subsequent deformation.

The flow characteristics of sheet steels may also be affected by the rate at which the sheet is deformed. The parameter which describes material characteristics as a function of deformation rate is known as the strain rate sensitivity, m. Usually the strain rate sensitivity only affects materials when a substantial change in stain rate occurs (i.e. greater than an order of magnitude). At room temperature the strain rate sensitivity of steels is usually low ($m<0.1$), however as materials approach one-half of their absolute melting temperatures, the strain rate sensitivity increases. The higher the value of m, the more resistant a material will be to instability or thinning. An extreme example of the effect of m on formability, is hot glass ($m=1$) which can be drawn from the melt into glass fibers without localized necking [6].

1.1.2 Effects of Coatings on Sheet Steel Formability.

The introduction of a thin coating alters the formability of sheet steels. Several authors [2,4,11] have investigated the mechanisms behind the inferior performance of the coated sheet steels compared to the formability of the bare substrate during pressing. The effects of coatings alter press performance through both a change in mechanical properties and a modification to the interactions between the sheet and the tooling.

Differences in mechanical properties between coated and uncoated sheet steels arise from differences in the thermal processing history of the sheet steel and also from the interaction of the sheet and the coating. The differences in thermal processing will be addressed in Section 1.2.1

The consequences of the interaction between the sheet and tooling on formability, arise due to the localized frictional effects. Interactions at the coating-tooling interface will affect strain distribution and punch loads as the frictional properties of the coating either retard or aid metal movement over the tooling [4]. Friction arises due to microscopic asperities of both the coating and tooling interacting together to retard sliding between the two surfaces.

Frictional values are a function of the normal contact pressure between the coating and tooling. At low contact pressures, Coulombic friction dominates and has a linear relationship to the applied pressure. The frictional stress, τ, to overcome Coulombic friction is given as

$$\tau=\mu p \tag{4}$$

where, μ is the coefficient of friction and p is the normal contact pressure. At low contact pressures, Coulombic friction is valid; however, as the contact pressure increases, the material may plastically deform. When the material plastically deforms, Coulombic friction is not valid and the friction behavior is related to the shear strength of the material, thus creating a constant frictional stress. The constant frictional stress, τ, is defined as

$$\tau=mk \tag{5}$$

where m is the interface friction factor, and k is the shear yield strength of the material ($k=\sigma_O/\sqrt{3}$, where σ_O is the flow strength). The relationship between the two frictional conditions as a function of contact pressure is shown in Figure 4. A transition from Coulombic behavior to constant friction incorporates the material flow properties, asperity deformation, and corresponding variations of true contact area [13].

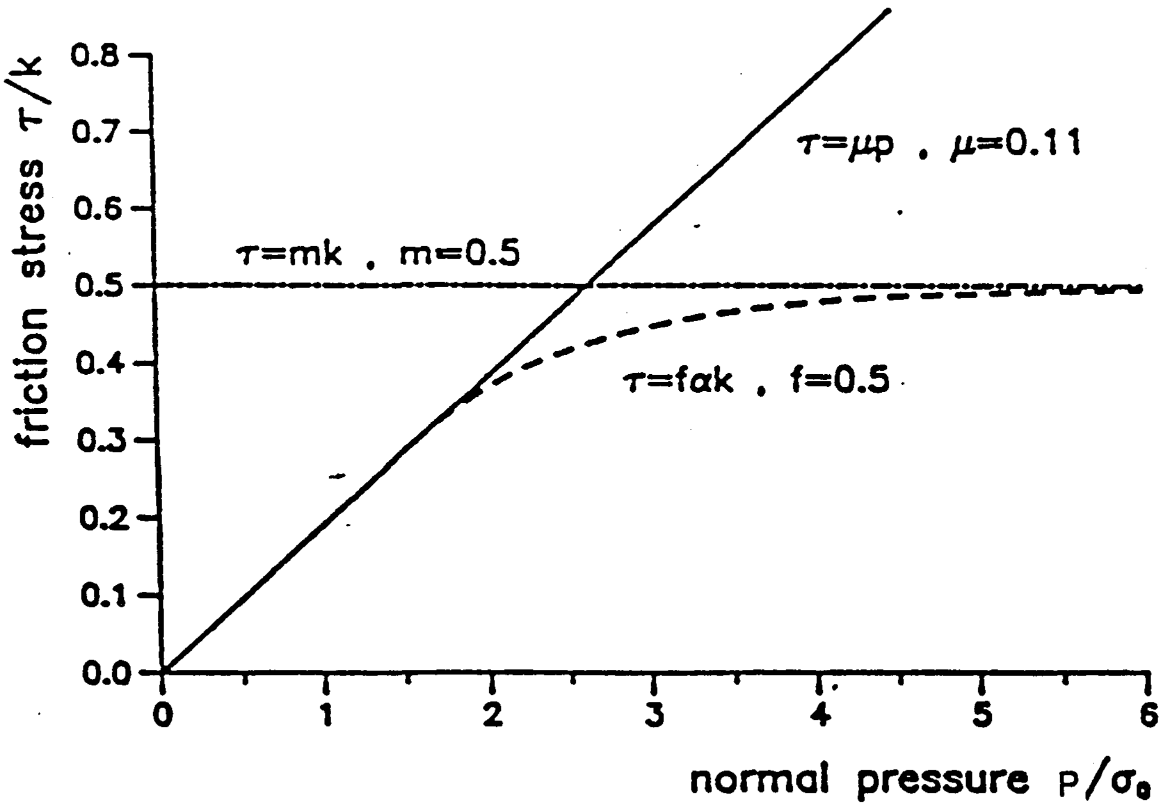

Figure 4 Relationship between Coulombic ($\tau=\mu p$) and constant friction ($\tau=mk$) as a function of normal contact pressure [12]. Also shown by the dashed line is the experimentally observed variations in friction stress.

The importance of friction on formability significantly increases as the relative movement between the tooling and coating increases. Formability testing using limiting dome height and angular stretch-bend tests have shown that the type of coating in contact with the punch has little influence on the sheet formability [3,4,14]. The limiting dome height and angular stretch-bend tests, stretch and bend the sheet with limited sliding between the sheet and the tooling. In these tests, friction is important only on how the strain is locally distributed between the tooling and sheet. In contrast, tests such as the draw bead, limiting draw ratio, and bending under tension have large displacements during deformation of the sheet over the tooling. For testing conditions with large displacements, formability of coated sheet steel is affected by the frictional stresses [4,15,16]. Metallic coatings usually decrease the overall sheet formability; however, some pure zinc coatings act as a lubricant, increasing formability during cup drawing.

The formation of asperities on the coating surface which are responsible for the frictional stresses can be influenced by the type of coating, processing parameters and growth of the coating on the substrate. These parameters can be controlled during the coating deposition and processing techniques prior to stamping. The effect of processing techniques also changes the overall formability of the coated sheet steel and will be discussed as a function of the particular coating process.

1.2 Development of Coated Sheet Steels.

Steels coated with a protective zinc layer were produced as early as 1742 [17]. The deposition process of zinc coatings evolved to incorporate control of the coating thickness, weldability and corrosion performance. Coatings are applied either via diffusional bonding or electrochemical bonding to the substrate. Differences in the two coating processes are evaluated in this section for zinc and zinc-iron coatings.

1.2.1 Hot Dip Galvanizing.

The original zinc deposition process on sheet steel was performed by dipping the sheet into a molten zinc bath allowing the zinc to solidify on the sheet surface. This process is known as galvanizing or hot dip galvanizing. The substrate to be coated with zinc must first be degreased and then cleaned or pickled to remove iron oxide scale or contamination resulting from prior processing. Fluxes are then applied to the surface to remove all impurities as well as prevent oxide formation and assist in wetting the zinc to the substrate. The fluxes can be applied prior to submersing or can reside as a surface layer in the zinc bath [17].

The galvanizing process proceeds according to the following reactions. As the sheet enters the molten zinc bath, the iron and zinc combine through diffusion to form iron/zinc compounds with a distinct phase distribution dependent upon the relative amount of iron and zinc. As the sheet exits the bath, the free zinc solidifies on the surface as it cools [17]. The application of the coating to the substrate is a two step process, the first depends on diffusion of iron and zinc, and the second depends on the solidification of the molten zinc.

Four phases have been shown to develop in the hot dip zinc coating. These are indicated on the iron-zinc phase diagram presented in Figure 5. The intermetallic phase located closest to the iron substrate is the γ (Gamma) phase (75 at.% Zn, 25 at.% Fe). The δ (Delta) phase (90 at.% Zn, 10 at.% Fe) is the next to develop followed by the ζ (Zeta) phase (94 at.% Zn, 6 at.% Fe) [19]. These three intermetallic phases depend on the diffusion of iron into the zinc coating. The last phase found on the surface of the coating is the η (Eta) phase (100% Zn) which

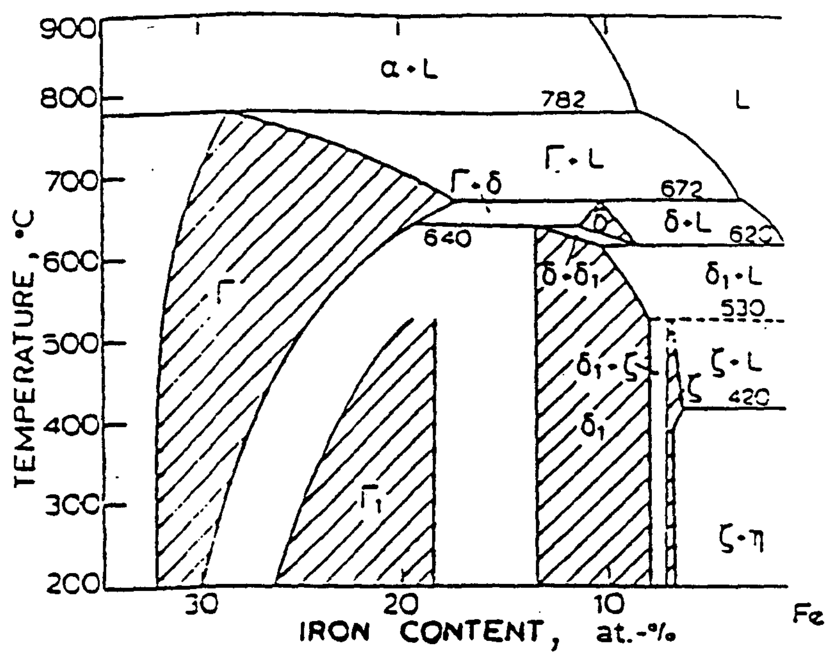

Figure 5 Zinc rich portion of the zinc-iron phase diagram [18].

solidifies as a cast dendritic structure. The relative thicknesses of the intermetallic phases are functions of the bath temperature and the time in the bath. Higher bath temperatures and longer soaking times will result in thicker intermetallic layers. Usually, the continuous hot dip application for sheet steels is relatively short, so that the intermetallic phases do not continue to grow. However, for batch galvanizing, the intermetallic layer will grow due to longer soaking times.

Continuous galvanizing of sheet steels promotes formation of thin intermetallic layers. The subsequent exiting from the zinc bath, allows the molten free zinc to rapidly solidify on the intermetallic layer. Solidification of the zinc starts at either random or controlled nuclei followed by the radial growth of grain clusters [19]. The type of solidification structure is a function of the alloying elements that are present within the zinc bath. Typically, the solidification structure that develops is referred to as a spangle. A spangle is a fan like structure with sections that have grains of similar orientations. The orientation of grains from section to section varies around the structure. This pattern is made up of alternating bright mirror-like sectors and frosty areas each of which may contain more than one grain [19]. Primary spangle forming alloy additions in the zinc bath are tin, lead, aluminum, antimony and copper. The presence of aluminum also assists in limiting the growth of the intermetallic layer [1]. A investigation by Cameron et al. [20] showed that spangles did not form with the addition of a single alloying element such as lead, but required an additional alloying element which had some solubility in both the liquid and solid zinc. The spangle structure that most prominently formed was one with the basal planes nearly parallel to the sheet surface and with a dendritic structure based on the hexagonal structure of zinc.

Alloying elements in the zinc bath along with cooling rates can control the spangle size. However, controlling the number of nucleation events dominates the resulting spangle size. To increase the number of nucleation sites impingement on the molten surface by steam, diammonium phosphate, and zinc dust will result in smaller spangle sizes due to the impingement of several neighboring spangles. Smaller spangle sizes are more desirable for deep draws and severe forming operations due to the elimination of reduction in thickness at spangle boundaries associated with large spangles. The reduction in thickness at spangle boundaries creates a rough surface which is detrimental to drawing [21].

The temperature of the zinc bath is usually around 460°C. The incoming sheet to be galvanized can be preheated to one of two temperature ranges depending on the prior processing history. Cold rolled steel that has been box annealed for good formability is heated to a temperature range close to that of the zinc bath. To replace the box anneal, the sheet is in-line annealed at temperatures between 680 to 870°C. Because the in-line anneal has a relatively short duration compared to the box anneal, the formability of the sheet is reduced. The decrease in formability is due to excess carbon remaining in solution resulting from the quick cooling. Post-box annealing is required to precipitate the carbon and restore formability [1].

1.2.2 Galvannealed Coatings

The presence of a zinc coating on automotive sheet steels alters the resistance spot welding parameters and decreases electrode life. During welding the zinc diffuses into the copper electrode, creating brass which causes the electrode tip to break down and mushroom, generally decreasing its life [22]. Because of the inferior weldability, and also to improve paint adhesion zinc-alloy coatings were developed [4]. One of the alloy coatings developed was galvanneal, a zinc-iron intermetallic alloy produced from the hot dip galvanizing technology.

To produce galvannealed coatings, the substrate to be coated is prepared identical to that for hot dip coatings and is submersed into the molten zinc bath. A intermetallic coating develops as in the hot dip, however one of two methods can be used to develop fully a zinc-iron coating. Instead of removing the sheet from the zinc bath and allowing the free zinc to solidify, one method of galvannealing leaves the sheet in the zinc bath for longer times. The relatively longer soaking times allows the intermetallic layer to grow by diffusion. Once the intermetallic layer has grown to the required thickness, the sheet is removed from the bath and the free molten zinc is removed with air knives [23]. A second method used to fabricate galvannealed coatings involves producing a hot dip coating and then subjecting that coating to a continuous heating cycle allowing the intermetallic layer to grow by diffusion. In either procedure, the primary mechanism of coating development is diffusion of iron into the zinc coating creating a zinc-iron alloy [24].

Formability investigations have shown that the zinc-iron alloy coatings produced by the galvannealing process are brittle and crack during deformation [11,23,24]. These investigations have also shown that the ductility, r-values, n-values, and drawability of the coated sheet steels decrease. The major reason for the decrease in properties is due to the presence of the zinc-iron alloy. The degradation in properties increases with increasing alloy thickness.

1.2.3 Electrogalvanized Coatings.

The hot dip coating process subjects the substrate to a different thermal processing history than conventional heat treating of uncoated sheet steels. To eliminate this different thermal processing history and have the coated sheet properties similar to the uncoated substrate, electrodeposition techniques to apply the coating were developed. The electrodeposition of relatively pure zinc to the substrate is referred to as electrogalvanizing.

Electrogalvanizing requires similar cleaning and surface preparation of the sheet steel as hot dip processing. Electrolytic cells deposit the zinc to the substrate by passing an electrical current through a zinc electrolyte from an anode, either soluble zinc slabs or insoluble anodes made of lead, lead alloys or platinized titanium, to the cathode or sheet steel. This process bonds the zinc to the steel electrochemically. Electrogalvanizing is conducted at temperatures close to room temperature, and thus, the mechanical properties of the coated sheet steel are similar to that of uncoated steel [1].

Several parameters in the electrogalvanizing process can affect the morphology of the zinc coating. The electrical overpotential (current density) supplied during deposition is one factor that controls the resulting morphology. Depending on the type of electrolyte, limiting current densities were found to provide smooth coatings. Below these limiting current densities, unfavorable macroscopic striated deposits were formed. In a study on electrodeposited zinc morphologies Jirincy et al. [25] explained that the nucleation and growth rates of zinc crystals depend on current density, and both rates increase with increasing current density. However, at low current densities the growth rate of zinc crystals is greater than the nucleation rate, creating the striated morphology. At high current densities, more nuclei are formed and the growth of zinc crystals impinge on one another resulting in a smooth deposit. Oscillation of the current density has also been shown to improve the morphology of the zinc coating [25,26].

The composition of the electrolyte affects the resulting morphology of the coating. Small additions of antimony, nickel, cobalt and organics, either in conjunction or separately, have been shown to affect greatly the coating morphology [25,26]. Depending on the additives used, the structures developed can range in appearance from plate like to blocky with voids. The change in morphology with alloy additions was shown to be true regardless if the electrolyte was acidic or neutral [25]. The speed of the sheet passing through the electrolyte creates either laminar or turbulent fluid flow in the electrolyte. Speeds that produce laminar fluid flow of the electrolyte create sharply defined plate-like microstructures, where as turbulent fluid flow results in less defined microstructures.

Kamei and Ohmori [26] conducted an experiment on hetero-epitaxial growth of zinc electrodeposits and found that the condition of the substrate prior to electrogalvanizing greatly affects the growth of zinc crystals. An increase in the thickness of an oxide layer on the iron surface prevents the hetero-epitaxial growth of zinc crystals from the ferrite substrate. Thin oxide layer dissolution may occur in the early stage of electrodeposition providing the direct interaction of zinc atoms with the ferrite lattice. The surface roughness introduced during rolling and pickling of the sheet will induce local disturbances in hetero-epitaxial growth of zinc crystals. The lattice match found by Kamei et al. [26], shows that when the (110) ferrite is parallel to the (0001) zinc, a orientation relationship between the crystals along the [111] ferrite and [$\bar{2}$110] zinc is obtained explaining the epitaxial growth of zinc on iron.

The electrogalvanizing process is complex and several factors including surface preparation of the steel, electrolyte composition, current density and relative speed of the sheet steel in the plating cell will determine the resulting morphology of the coating. It has also been shown that the texture of the substrate can effect the coating morphology [26].

1.2.4 Zinc-Iron Electrodeposited Coatings.

Electrodeposited zinc-iron coatings can be systematically controlled to deposit iron contents between 0% and 100%, where typically galvanneal coatings contain 15% iron. The control of iron content of electrodeposited coatings allows for optimization of the desired coating properties. Electrodeposition of alloy coatings also provides a relatively unaffected substrate due to similar reasons stated for electrogalvanized coatings. As with electrogalvanized coatings, substrate preparation is important for alloy coatings.

The plating conditions for zinc-iron coatings are vital to the quality of the product. It is especially important to prevent bath deterioration due to the formation of Fe^{+3} [27]. Fe^{+3} ions are precipitated in the form of $Fe(OH)_3$, which causes deterioration of coating adherence on steel. The current density, ph of the solution, and the speed of the sheet are also important parameters that must be optimized for proper development of the coating.

Investigations [27-29] have shown that the coating phases developed with electrodeposition shift in compositional range with respect to that found for hot dip alloy development. A relationship of the phases found by the hot dip coating process is compared to the phases found by electrodeposition in Figure 6 as a function of iron content. Electrolytic deposition showed that the single phase, alpha, extends down to about 50% iron (Figure 6b) compared to a lower limit of 80% iron for hot dip deposition (Figure 6a). Other phases are also shown to shift relative to iron content between the two deposition techniques. The shift in the phase distribution may be important if a particular phase is detrimental to the

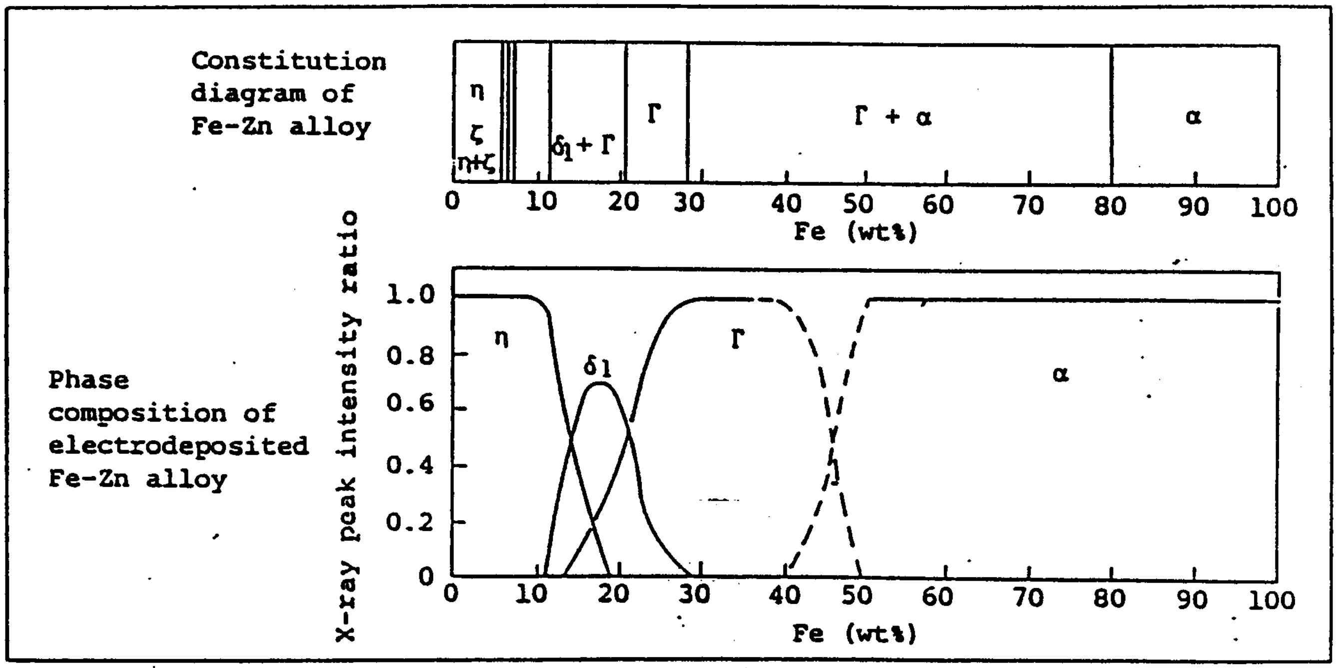

Figure 6 Comparison of phases determined by x-ray analysis as a function of iron content for hot dip and electroplated coatings [27].

coating properties.

An investigation by Kojima et al. [30] on the properties resulting from changes in the iron content of electroplated zinc-iron alloy coatings showed that an iron composition of 40% resulted in the maximum coating loss on the inside of a sheet bent 180 degrees. The coating loss measured in this test did not change below an iron content of 20% or above 60%. A similar investigation of the effects of iron content and coating properties by Adaniya et al. [27] shows a range of acceptable iron content between 15 to 25% iron (Figure 7) for the properties evaluated The weldability rating in Figure 7 increases with increasing iron content up to 30% iron and levels off. The workability, however, decreased with increasing iron content, and thus resulted in a range of acceptable iron content in the coating.

The previous sections have discussed coating deposition on sheet steels and the various parameters affecting the development of the coating. A generalized flow chart summarizing the differences in processing between coated and uncoated sheet steel is depicted in Figure 8. From these differences in processing and the different types of coatings used, the formability of the sheet steels has changed. Thus, investigations to establish the differences

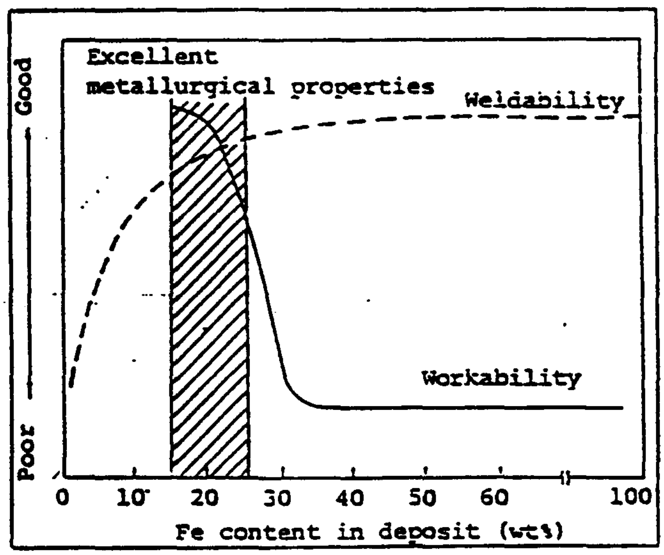

Figure 7 Schematic diagram which illustrates relative weldability and workability of electrodeposited zinc-iron alloy coatings as a function of iron content [27].

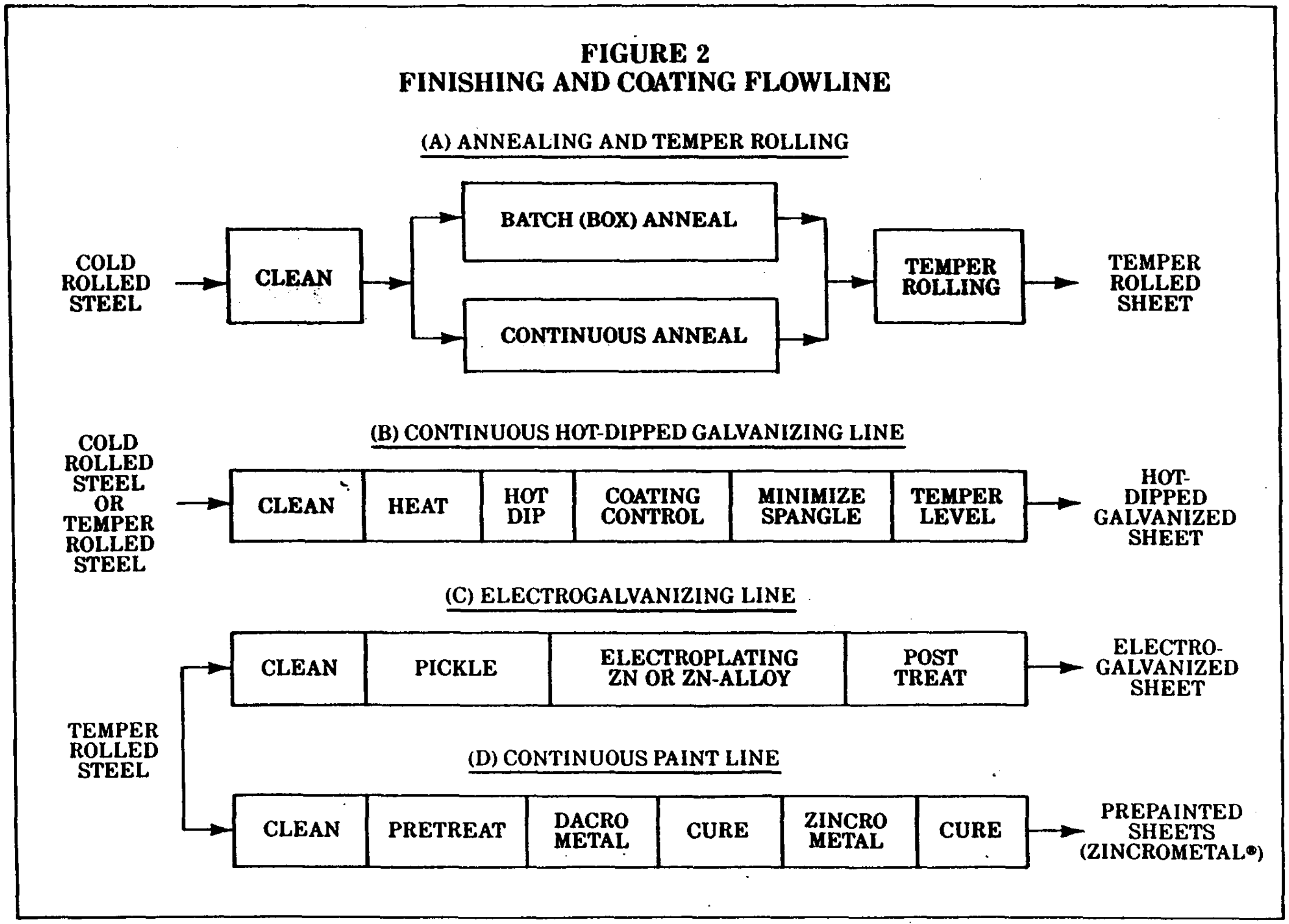

Figure 8 Summary of processing steps to produce coated sheet steels [1].

in formability of the coated sheet steels have been performed. One aspect of the inferior coated sheet steel performance is related to the coating damage that occurs during deformation.

1.3 Definitions of Coating Failures

Coating damage during stamping can lead to problems with corrosion protection and can cause surface defects on subsequent stampings if the coating is removed from the sheet and remains attached to the die surface [21]. Typically, coatings fail in one of three modes: powdering, flaking, or galling [28,29,31]. Unfortunately, a literature review revealed numerous definitions of each type of failure. Table 1 compares the definitions of powdering, flaking and galling which were utilized in three recent publications [28,29,31].

Ike [31] concluded that powdering resulted from any form of plastic deformation in which a hard and brittle surface coating is incapable of following the bulk deformation. Ike also concluded that flaking is entirely prevented by eliminating sliding between the tool and sheet. Makimatilla and Ranta-Eskola [28], however, stated that flaking could occur with or without sliding contact by the die surface. The definition of galling is the only

Table 1 Definitions of coating failures

Failures	Authors: Ike [31]	Makimatilla [28]	Ejima [29]
Powdering	Particle removal due to brittle fracture in coating.	Asperities of tool surface ploughing through coating.	Type of coating failure which results from deep drawing.
Flaking	Large fragments pulled off by sliding contact with die.	Failure of fragments by shearing at zinc/iron interface.	Large fragments removed by sliding under high pressure.
Galling	Ploughing by fragments adhering to the tool.	Ploughing by fragments adhering to the tool, size of adhere particle grows with sliding distance.	Ploughing by accumulation of material on die.

definition which appears to be similar among the authors.

From the variations in the definitions of powdering, flaking and galling, it was determined that a universal definition of the failures should be developed. The following definitions of powdering, flaking, galling and cracking were determined partially from those found in the literature and from experimental observations contained in future sections of this report. Powdering consists of particle formation by intracoating failure to produce particles with sizes less than the coating thickness. Flaking consists of flat particle formation by decohesion of the coating/substrate interface to produce particles with sizes similar to the coating thickness. Galling results from adhesion of zinc particles to the tool surface. The adhered particles plough through the coating or bond to the coating resulting in additional coating damage with subsequent forming operations. Cracking consists of through thickness fracture without particle decohesion from the substrate. Summarizing the differences in the definitions, flaking occurs at the coating/substrate interface, galling occurs at the coating/tooling interface, and powdering occurs within the coating itself between the substrate and tooling interfaces.

1.4 Purpose and Objective of Research.

Several formability tests mentioned earlier have been used to evaluate the formability of coated sheet steel. Formability tests such as the angular notch bend, limiting dome height and tensile test either stretch, or stretch and bend the sheet steel. These tests do not involve changes in strain state during deformation. Formability tests such as cup drawing and draw bead simulation do involve changes in strain state and have shown that different coated sheet steels have different formabilities. Usually, stamping operations involve both stretching, drawing and changes in strain state. The thrust of this investigation is to evaluate the formability of the coatings in response to changes in stress and strain state. For example, do the coating deformation characteristics differ if a compressive strain is applied followed by a tensile strain or vice versa? A formability test that induces changes in stress and strain state is cup drawing. Cup drawing has been used to evaluate coating behavior [2,28,29,31]; however most of these investigations have used corrosion testing or tape tests to evaluate the damage to the coating. This investigation determines the mechanisms of the coating failures related to the stress and strain histories subjected to the coating. Six coatings are evaluated: three electrogalvanized, a hot dip, a galvanneal and a zinc-iron electrodeposited alloy. The three electrogalvanized coatings are manufactured by different suppliers and thus differences in formability should be a consequence of differences in coating microstructures which depend on application parameters used by each supplier. The hot dip coating can be compared against the electrogalvanized coatings showing differences in deposition techniques such as diffusional bonding and cast microstructure for the hot dip coating verses electrochemical bonding and epitaxial microstructures for the electrogalvanized coatings. The zinc-iron alloy coatings investigated have different bonding mechanisms to the substrate. The galvanneal coating has diffusional bonding and the electrodeposited zinc-iron alloy coating has electrochemical bonding. Comparisons between the formability of the alloy coatings can be related to the type of bonding used to deposit the coatings.

2.0 EXPERIMENTAL PROCEDURE

2.1 Coatings Evaluated.

A test matrix consisting of six coated sheet steel products was evaluated to determine the response of the coatings under deep drawing forming applications. Three of the six sheet products are pure zinc electrogalvanized coatings designated by the following convention, I70G70G, S70G70G, and R60G60G. The first letter designates the supplier; Inland, Stelco, or Rouge; the numbers designate the coating weight in g/m^2 on each side of the sheet. The letter G designates the coating type, electrogalvanized in this case. The second type of coated product evaluated was the S60HD, a hot dip zinc coating with 60 g/m^2 on each side supplied by Stelco. Two zinc-iron alloy coatings were also evaluated; a galvannealed product supplied by Inland, I60N40N, with differential coating weights on each side and a zinc-iron electrodeposited coating supplied by Rouge, R40A40A. The coating weight of the materials selected for testing was essentially constant, 60 g/m^2, minimizing any effects that would arise due to different coating thicknesses.

2.2 Cup Drawing Apparatus.

A deep drawing system for producing 2-inch diameter flat bottom cups was designed and fabricated for this program. The system, shown schematically in Figure 9, consists of a cylindrical top and bottom frame containing dies and springs that are changed to accommodate drawing requirements. Two cylindrical bottom dies were interchanged to accommodate sheet thicknesses of 0.030 and 0.050 inches. The dies have a one-quarter inch drawing radius. The bottom dies were bolted to the bottom frame preventing movement of the die during drawing.

The cylindrical top platen and top frame were machined to specifications allowing the top platen to move up as the sheet steel disk thickens during drawing. The top platen and the bottom die were machined from D-2 tool steel, hardened to HRc-62 and finished to a maximum surface roughness of 5μ-inches, which are the same specifications used in fabricating the limiting dome height testing apparatus utilized by Burford [32]. The dies allow for a 5.125 inch maximum diameter disk to be drawn or a draw ratio of 2.56.

Six springs positioned axisymetrically in the top frame transmit a hold down force through the top platen to the disk preventing wrinkling during drawing. The hold down

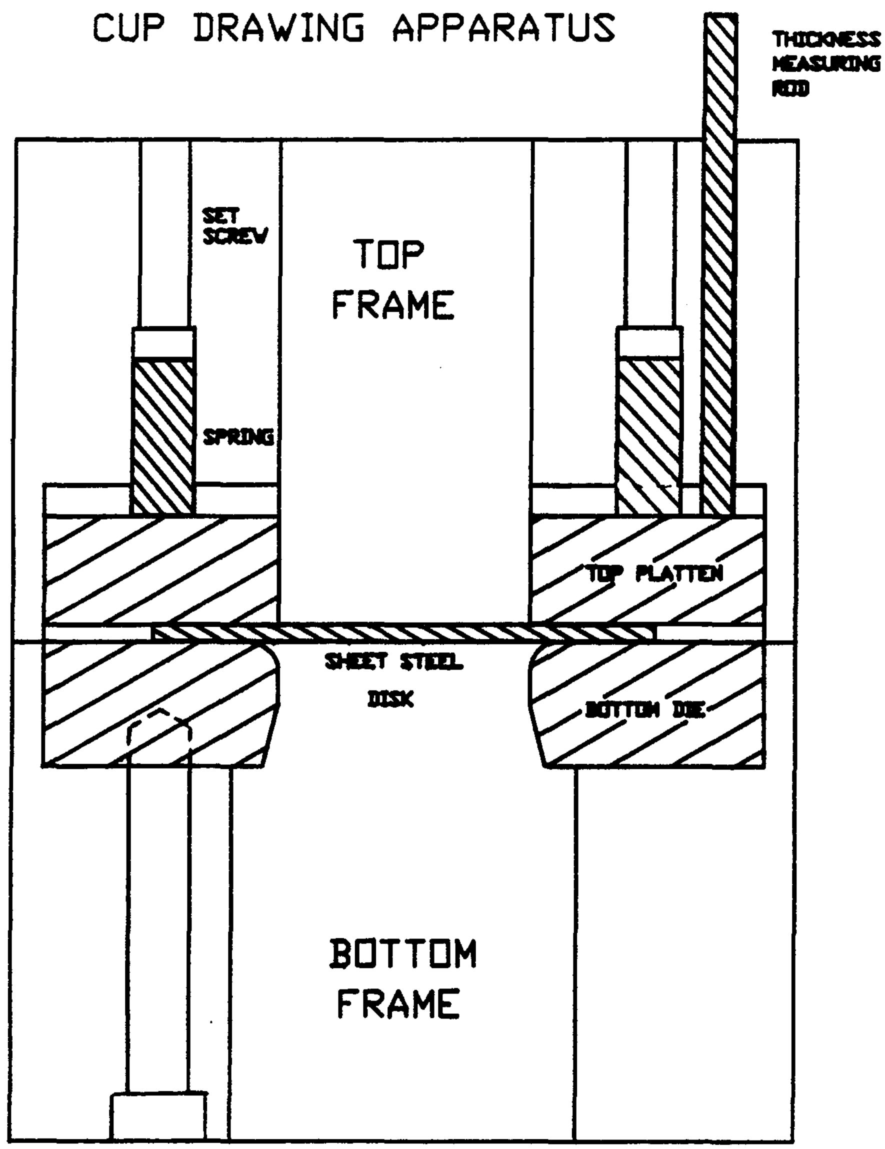

Figure 9 Schematic representation of experimental apparatus used for deep drawing.

force was controlled by compressing the springs with set screws located in the top frame. Required spring displacements were predetermined by calculations with the specified spring constants supplied by the manufacturer. The spring constant was experimentally verified with load versus displacement data for the system. Calibration of the effective spring constant for the system showed that when the springs were fully compressed, the spring constant significantly increased. The required hold-down forces during drawing were determined experimentally and were found to be that required to eliminate wrinkling during drawing. To monitor the displacement of the top platen during drawing, a one-quarter inch diameter rod was inserted through a hole in the top frame. The top platen was pushed up during drawing due to sheet thickening which in turn displaces the one-quarter inch diameter rod. The maximum thickness of the sheet was indirectly monitored by attaching an extensometer to the top frame and rod.

The top and bottom frame were bolted together after a properly prepared disk was inserted between the bottom die and top platen. Preparation of the coated sheet products required shearing 4 inch diameter disks and removal of any shear burr with a lubricated 240 grit belt sander. The disk was cleaned with acetone to remove the protective oil coating applied by the supplier. "LubriMatic" multi-service grease produced by the Lubrimatic Division of Witco Corporation was applied to both sides of the blank with a brush to provide a thin and uniform lubricant coating.

The lubricated disk was inserted between the top platen and bottom die. The top and bottom frame were bolted together and the springs were adjusted to the desired hold down force. The two inch cylindrical punch, with a one-quarter inch nose radius, was inserted in a hole in the top frame until it contacted the disk. The self contained apparatus was then inserted between two compression platens on either a 100 kip or 20 kip MTS load frame. A punch velocity of two inches per minute was used for cup drawing. Both fully drawn and partially drawn cups were produced on this system. Computerized data acquisition simultaneously monitored punch force, punch displacement, and disk thickening during drawing.

After removal of the cup from the punch, the lubricating grease was wiped off with acetone. Sections were cut from the cup with water cooled cutoff saws for further examination. The sectioned pieces of the cup were ultrasonically cleaned in acetone prior to microscopic or other examinations.

2.3 Microscopic Examination

The surface morphologies of the coated products prior to deformation and after deformation were examined with a JEOL 840-JXA scanning electron microscope (SEM). Qualitative and quantitative chemical analysis of the coatings were performed with software provided in conjunction with the Tracor-Northern energy dispersive x-ray spectroscopy (EDS) analysis on the SEM.

The grain sizes of the substrate steels were determined with standard polishing and etching procedures. The most effective ferrite grain boundary etch determined was 5% nital. The polished and etched specimens were examined with a Leco Neophot 21 microscope. A linear intercept method was used to determine ferrite grain size.

The examination of the microstructure of the hot dip coating was accomplished by first polishing normal to the coating surface with 1μm diamond paste suspended in polishing oil on a rotating cloth disk. The polished surface was then etched with a solution containing 25 g. of CrO_3, 5 g. Na_2SO_4 and 100 ml H_2O for 3 to 10 seconds. The sample was immediately rinsed in running water to prevent staining.

2.4 Microhardness Evaluation

The microhardnesses of the coatings and the substrates were determined with a diamond pyramid indentor and various loads. Due to difficulties in reading the size of the indention on the original rough surface of the coatings, it was necessary to polish the coating. The coated sheet steel was sheared into disks, approximately 25mm in diameter and cold mounted onto a aluminum stud. The shear burr was removed, and the specimen was polished using only one micron diamond paste on a rotating polishing wheel lubricated with polishing oil. The micro-hardness was monitored during polishing and did not change due to the polishing procedure. The depth of indenter penetration was determined by measuring the diagonals of the pyramid hardness indention and then calculating the depth of penetration from the known geometry of the pyramid indenter.

2.5 Texture Evaluation

The textures of the coatings were evaluated with a Rigaku rotating anode x-ray diffractometer. Diffraction patterns were generated in this diffractometer from filtered Cu-Kα radiation with a wavelength of 1.5405 Å. Only the planes parallel to the sheet surface contributed to the diffracted intensities. Comparisons of intensity between the planes parallel to the sheet surface was accomplished by measuring the relative peak heights. Orientation of the diffracted peak intensities was monitored parallel to and transverse to the rolling direction for the as-received samples. This technique has been used by other investigators [33]. The Rigaku diffractometer requires a flat sample surface for accurate orientation relationships. Due to this requirement, only sections from the flange of partially drawn cups were evaluated.

3.0 EVALUATION OF STRESS AND STRAIN STATES.

The deformation characteristics of coated sheet steels depend both on the material properties of the steel and the imposed stress/strain states. The stress and strain states associated with cup drawing are complex and were analyzed with finite element (FEM) and slab equilibrium modeling techniques. The stress states determined from the two modeling techniques are compared in this section along with complete stress histories determined from the FEM analysis for the sheet steel during drawing.

Sachs [34] determined the stress states typically associated with cup drawing and his results are shown in Figure 10a [6]. The stress state in the flange region of the sheet consists of a compressive stress in the hoop direction, a tensile stress in the radial direction, and a compressive stress through the thickness due to an applied hold down pressure. The stress state in the cup wall is primarily biaxial tension with a possible compressive stress resulting from contact with the punch in the thickness of the sheet. The stress state in the sheet under the punch nose is biaxial tension in the plane of the sheet. The stress states shown in Figure 10a indicate that during drawing a change in stress state occurs at the die

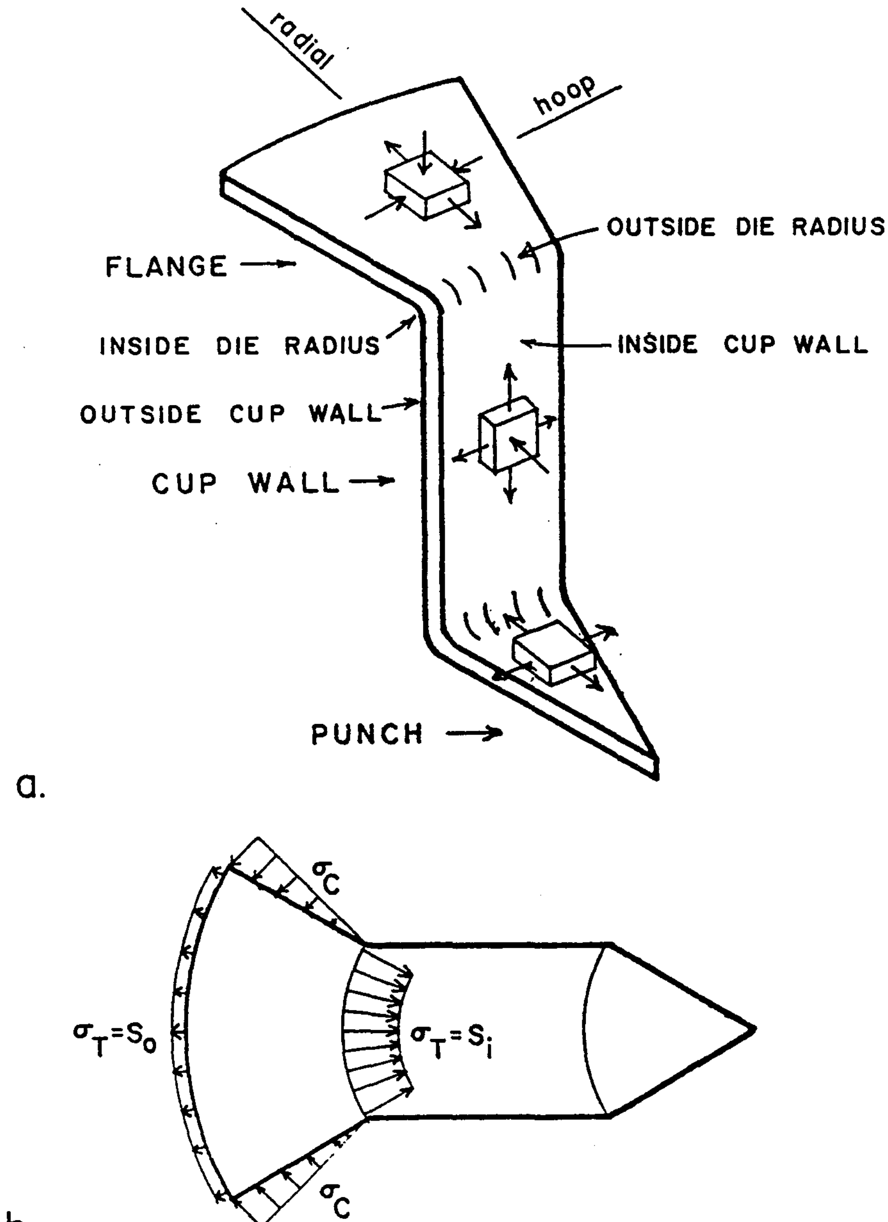

Figure 10 Schematic representation of stress states during cup drawing, a) stress cubes in the three regions, b) relationship of stress gradients in the flange as determined by slab equilibrium analysis [34,6].

radius. Furthermore, the stress state of the sheet at the die radius varies through the sheet thickness. Due to the bending of the sheet steel around the die radius the inside die radius side of the sheet undergoes a compressive stress in the radial direction while the outside of the sheet develops a tensile stress.

Two theoretical analyses were used to predict the stress states during deep drawing: a slab method similar to that determined by Sachs [34] and an analysis based on finite element modeling. The simplified slab method solution is based on uniform deformation and force equilibrium. The slab equilibrium technique utilized by Sachs has several limitations as only stresses in the flange of the cup drawing process are evaluated. The stresses included in the force balance are shown schematically in Figure 10b. A compressive stress gradient in the hoop direction in the flange exists with a maximum compressive stress at the outermost fibers and a minimum at the die radius. A tensile stress gradient which is a maximum at the die radius exists in the radial direction. The slab equilibrium analysis assumes perfectly plastic material deformation behavior. Although this assumption simplifies the analysis, it is violated for the materials under investigation. Secondly, the analysis considers plane strain, as the sheet thickness is assumed constant (i.e. thickening of the sheet during deformation is ignored). Finally, the stresses predicted by this analysis are only valid for a particular instant of time (i.e. position) during the drawing process. To generate a complete stress history in the flange during the drawing process, and thus predict punch load versus displacement, the analysis must be computed incrementally for each displacement of the punch.

Due to the limitations of the slab method a FEM technique was also utilized to evaluate the stress states in the sheet steel during cup drawing. The following sections will compare stresses determined from the FEM technique with those of a slab equilibrium technique.

3.1 Finite Element Analysis of Stress States.

The FEM code utilized in this investigation was Nike2D from the Lawrence Livermore National Labs [35]. The analysis used 1863 nodes and 1528 elements and the dimensions of this model matched the physical dimensions of the experimental apparatus. Cross sections through the axisymmetric mesh in the initial configuration is shown in Figure 11 while the mesh at a punch displacement of 0.75 inches is shown in Figure 12. Due to axisymmetry, the

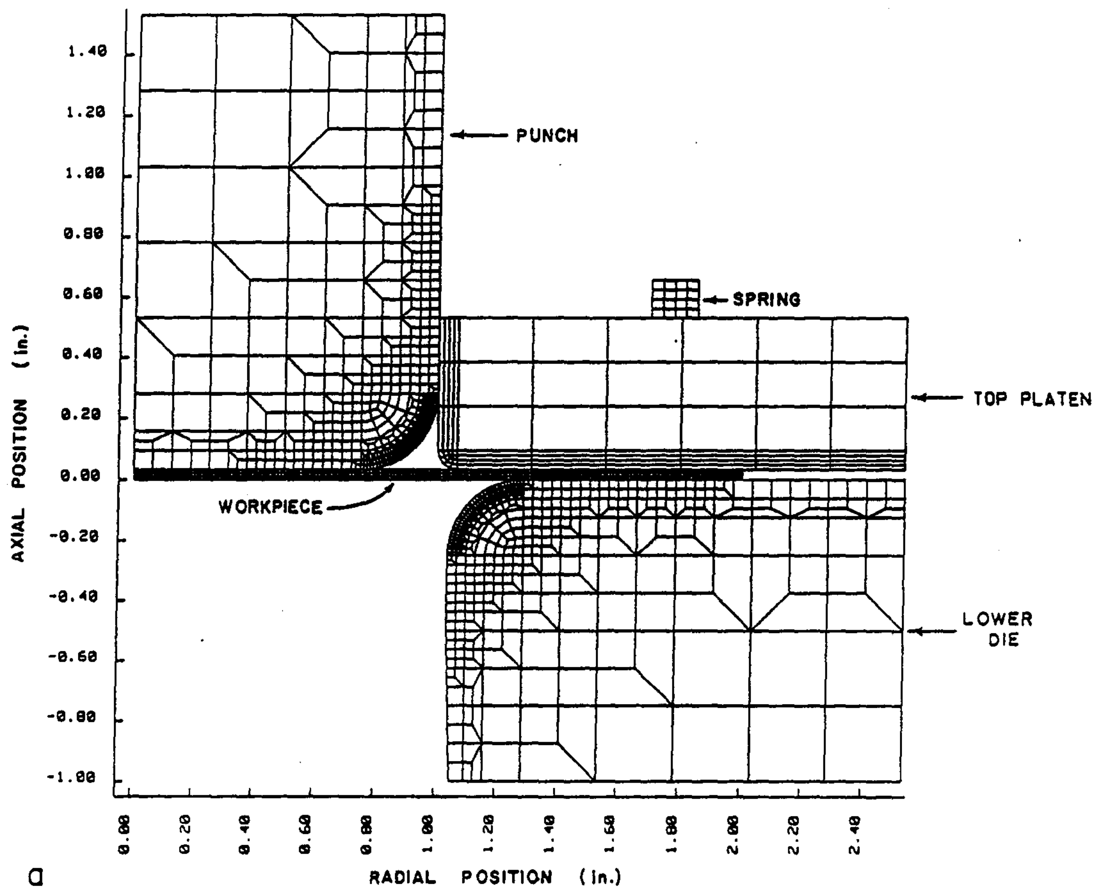

a

Figure 11 Schematic representation of the FEM mesh showing original grid configuration of the workpiece and tooling.

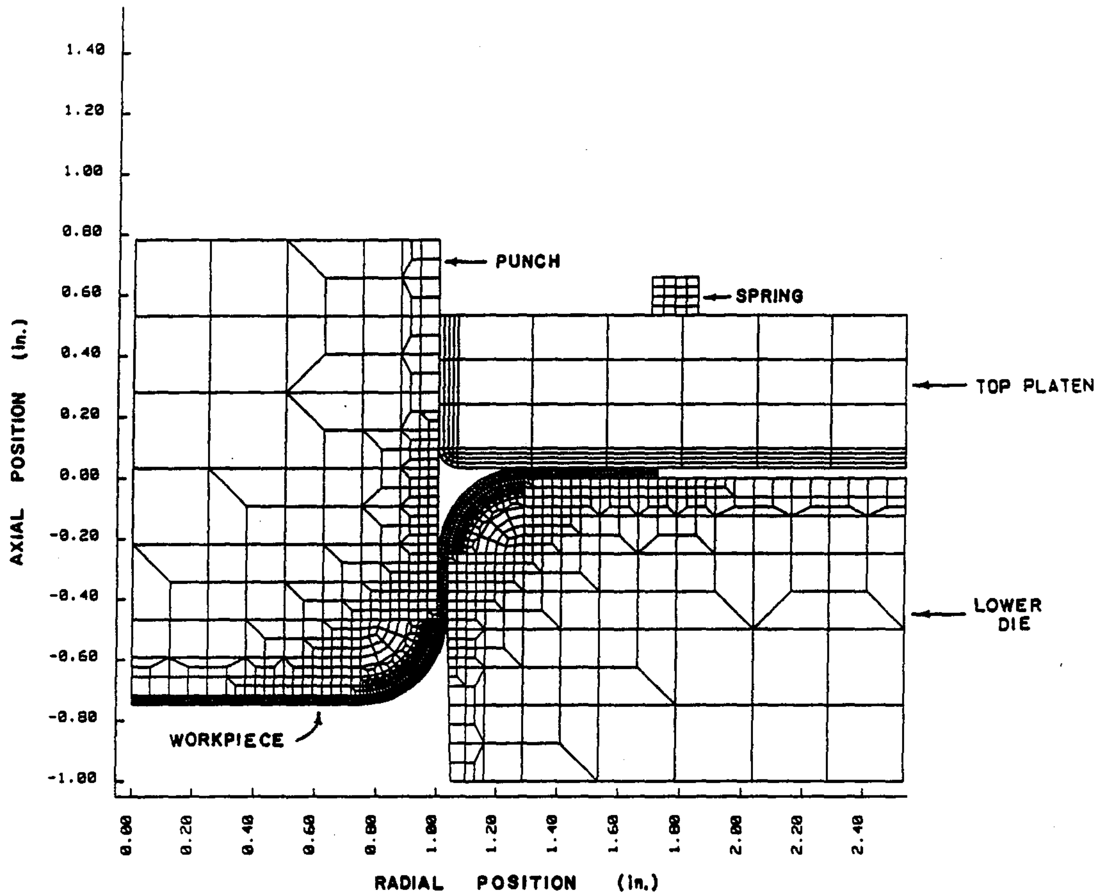

Figure 12 Schematic representation of the FEM mesh at a punch displacement of 0.75 inches.

radial coordinate starts at the center line of the punch and thus only half of the cross section is depicted in Figure 11. The mesh of each component of the system was configured to maximize the results of the analysis. The 0.030 inch thick, 4.00 inch diameter disk workpiece was divided into 600 square elements, each with a width of 0.010 inches resulting in three elements through the thickness. With this mesh, through thickness stress gradients were determined. The use of multiple elements through the thickness was in contrast to other investigations where a single element was utilized through the thickness [36]. Since the stresses in the workpiece are of primary interest, the workpiece elements were smaller than the tooling elements resulting in higher resolution of the workpiece stresses. The small elements in the punch radius and bottom die radius were configured to accommodate the expected maximum tooling stresses at these locations. As with the experimental apparatus, the top platen was allowed to displace to accommodate workpiece thickening during drawing. The four by four element spring located on top of the top platen accounted for the hold down force imposed by the six springs in the apparatus. Perfectly elastic material properties for the punch, bottom die, top platen, and spring in the FEM analysis were assumed to be that of steel with an elastic modulus of 30,000 ksi, poisson's ratio of 0.3 and a density of 490 pounds per cubic foot.

The Nike 2D program allows for several types of deformation analyses such as elastic, elastic perfectly plastic, elastic-plastic etc. This analysis used elastic-plastic properties to model the deformation of the workpiece. For the FEM analysis, the strain hardening behavior of actual stress/strain data was approximated by eight piece wise linear segments. The piece wise linear approximation for I60N40N sheet steel tensile tests performed by Wilson [14] is shown in Figure 13. This approximation incorporates elastic and plastic flow behavior and is assumed to be strain rate independent for the analysis.

A constant hold down force of 900 pounds was specified as a boundary condition applied to the top of the "spring" for the FEM analysis. Since springs were used in the experimental apparatus, thickening of the disk workpiece caused the top platen to move up, further compressing the springs and thus increasing the hold down force. Because a constant hold down force could not be maintained experimentally, initial hold down forces between 750 and 800 pounds were used experimentally as a comparison to the

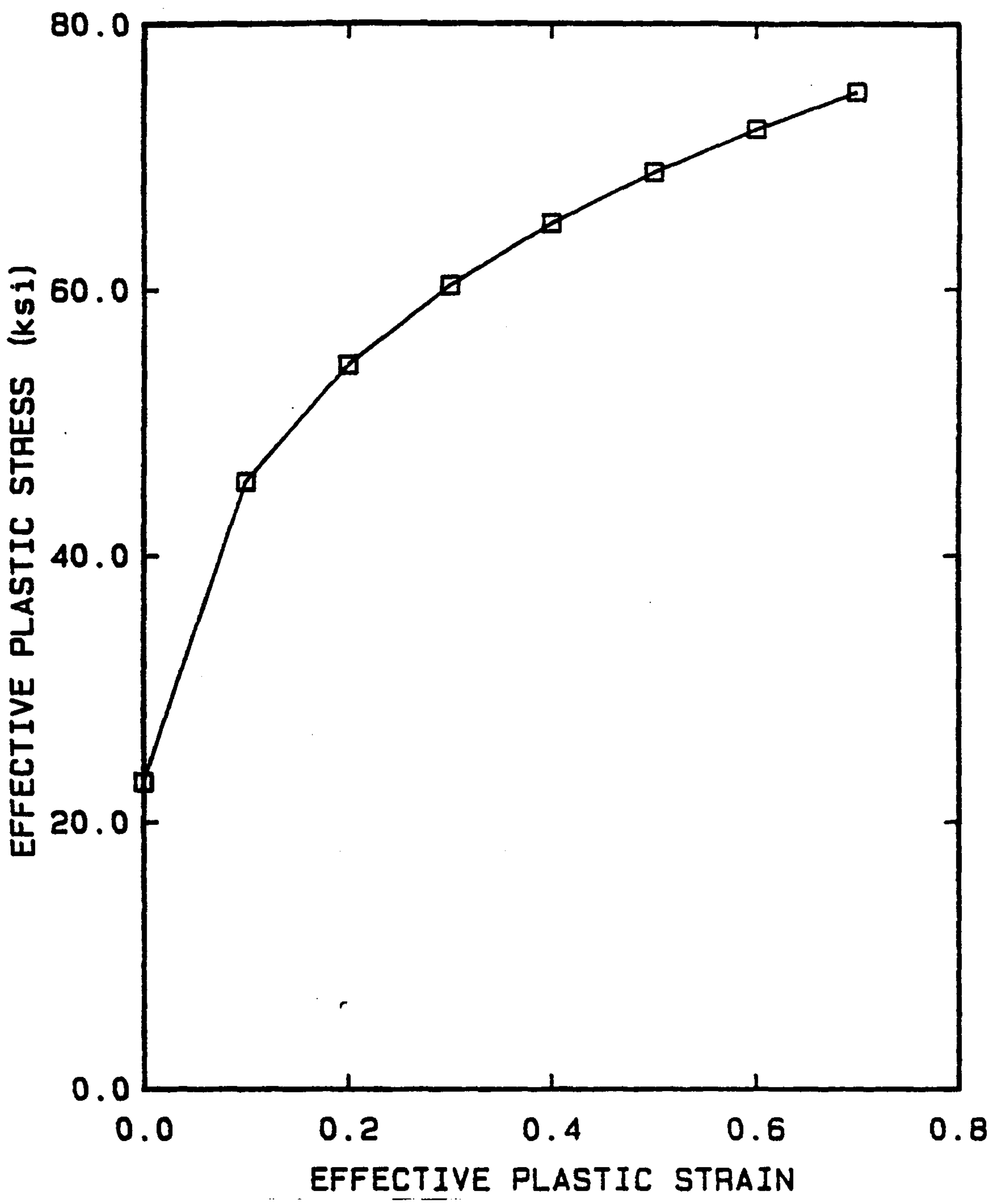

Figure 13 The piecewise linear approximation of the measured stress-strain behavior of the I60N40N sheet steel.

FEM analysis. The coefficient of friction for the drawing apparatus and lubricant was approximated based on the results of several investigations. A separate investigation [37], determined a friction coefficient of 0.15 using almag mineral oil on a bending under tension friction testing apparatus for the same coated sheet steel. Other investigations using lubricants have determined friction coefficients as low as 0.04 [38]. The grease lubricant used in this thesis probably has a corresponding friction coefficient between 0.15 and 0.04, thus a estimated friction coefficient of 0.10 was used in the FEM analysis. The frictional surfaces were between 1) the sheet and punch, 2) the top platen and sheet, and 3) the bottom die and sheet. The FEM analysis was run on a VAX 8600 computer and took 480 cpu hours to displace the punch 1.50 inches. The results of this analysis and the comparison of the results with experimental tests are presented in the next several sections.

3.1.1 Comparison with Experiments.

Two sets of experimental data were used to evaluate the accuracy of the FEM analysis. The first set was the punch load versus punch displacement curve obtained during the deep drawing experiment and the second was the binder plate displacement, measured as a function of the punch displacement during the experiment.

The comparison between the load-displacement curves from duplicate experimental runs and from the FEM analysis is shown in Figure 14. Since a constant hold down force cannot be maintained with the experimental apparatus, two tests were performed with initial hold down forces of 750 and 800 pounds. The agreement in form between the experimental data and the results from the FEM analysis is excellent. The peak load value for the FEM analysis is lower than the experimental data. The likely reason for this discrepancy is due to the choice of friction coefficients. The use of a friction coefficient greater than 0.1 would have increased the peak load. Evaluation of the friction value can be incorporated in future studies. The FEM analysis shows that the beginning of a second peak in load is due to ironing of the sheet between the punch and the inner vertical surface of the bottom die. The experimental curves also show this ironing peak, but at larger displacements. The FEM analysis assumes isotropic deformation, however the sheet steel tested developed slight earing resulting from anisotropic deformation. The anisotropy of the sheet steel probably results in the delay of the formation of the ironing peaks compared to the FEM

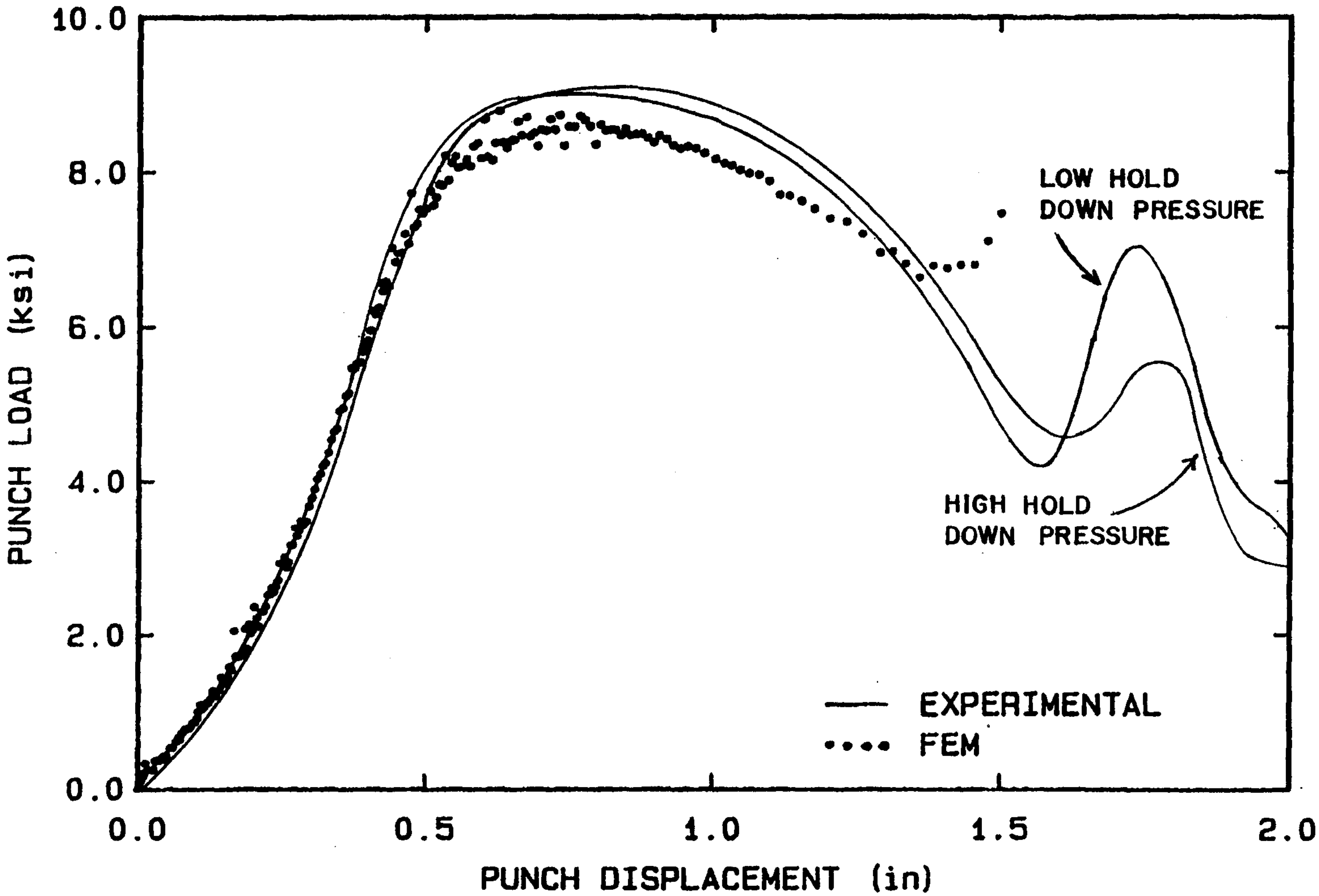

Figure 14 Punch load versus punch displacement data for two experimental tests, with high andlow hold down pressures, compared to the results from the FEM analysis 56

analysis as shown in Figure 14. In addition, the drawn cups exhibited slight wrinkling which was not part of the FEM analysis.

Figure 15 illustrates the top platen displacement, a measure of thickening in the flange region during drawing as a function of the punch displacement for the same two experimental tests that were shown in Figure 14. The top platen displacement predicted by the FEM analysis is also shown in Figure 15. There is good correlation between the experimental data and the FEM results. An interesting feature, evident in all three curves at a punch displacement of approximately 1.25 inches, is a marked slope change or increase in top platen displacement. This is due to elastic bending of the final material in the flange as it is pulled over the lower die. A cross section through the dies and sheet steel at a punch displacement of approximately 1.4 inches is shown in Figure 16. The tail of the sheet steel has lifted off of the bottom die causing the top platen to move upward in excess of the sheet thickening because of elastic bending around the die radius. The lifting results in the dramatic increase in binder plate displacement which is observed in Figure 15.

Overall there is very good correlation between the FEM analysis and the experimental tests. This lends credence

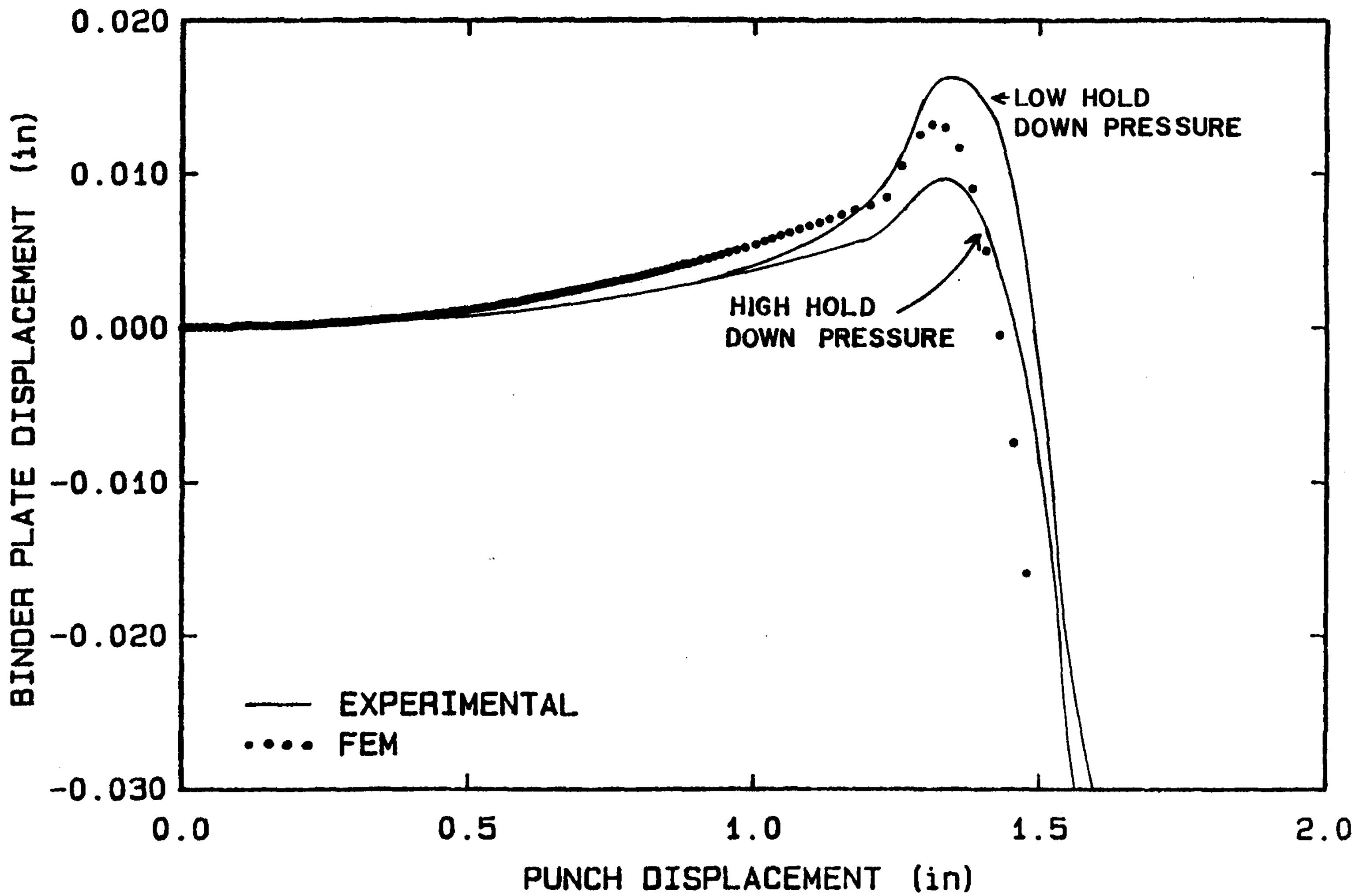

Figure 15 Top platen displacement versus punch displacement data for two experimental tests, with high and low hold down pressures, compared to the results fromthe FEM analysis.

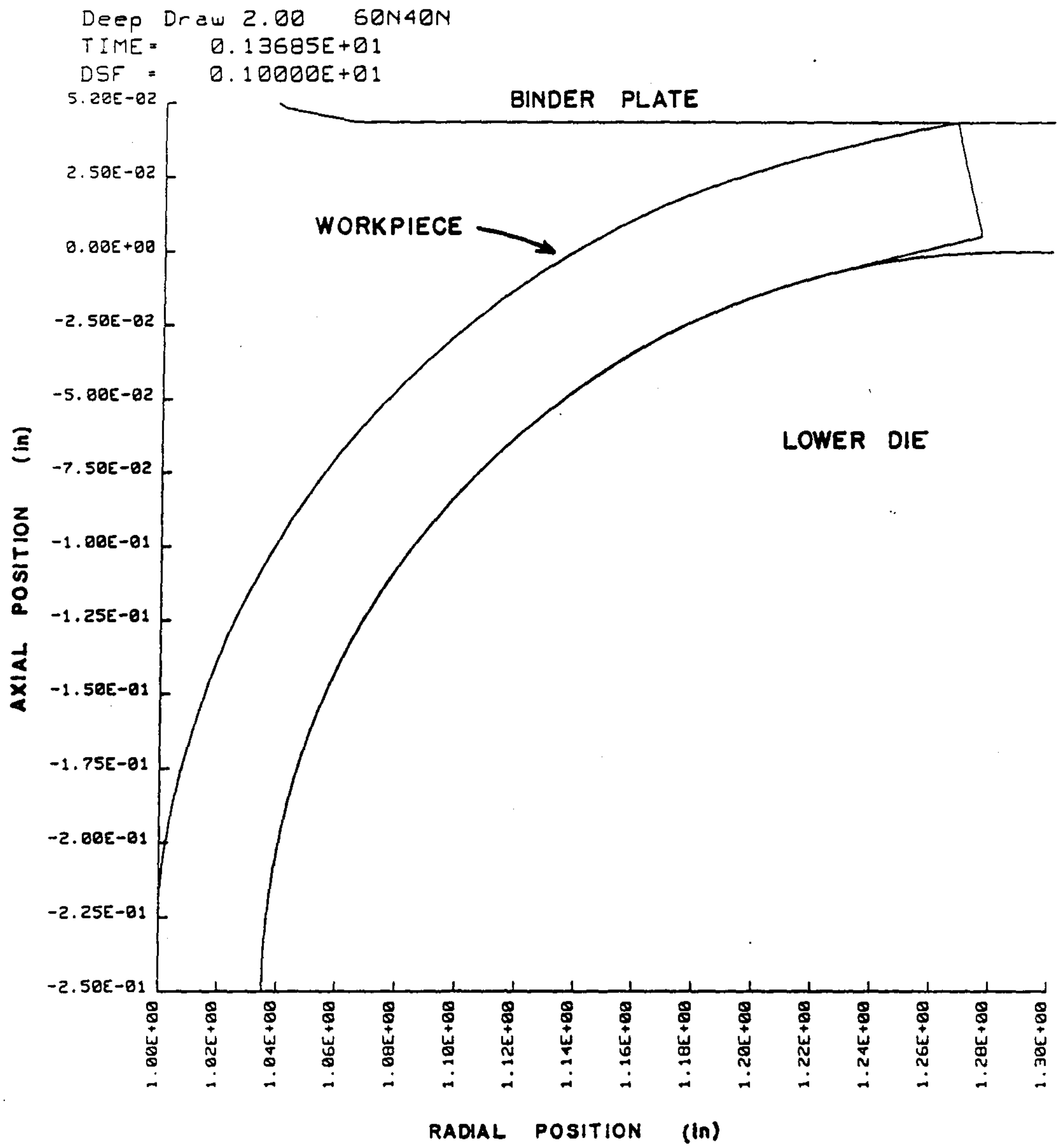

Figure 16 Predicted geometry of the workpiece and tooling from the FEM analysis at a punch displacement of 1.4 inches. The edge of the workpiece has lifted off of the lower die.

to the other aspects of the FEM analysis which are presented below.

3.1.2 Stresses in the Flange.

The stresses in the flange determined by a slab equilibrium analysis which is similar to Sachs's shown in Figure 10 are compared to the stresses determined by the FEM analysis. The radial, hoop and thickness stresses in the flange of a partially drawn workpiece were determined at a punch displacement of 0.75 inches. The stresses were evaluated at the mid-thickness of the sheet along a line starting at a radial position (referenced from the center of the disk) of 1.40 inches and extending to a radial position of 1.72 inches, which is within the flange region. The stress values at each point along this mid-thickness line, as determined by the FEM analysis, are shown in Figure 17. Also shown in Figure 17 are the corresponding values of the slab method analysis outlined below.

From a simple slab equilibrium analysis for the flange region of the sheet, it can be shown [40] from the summation of forces in the radial direction that:

$$\sigma_R + R d\sigma_R/dR - \sigma_\theta = 0 \qquad (6)$$

If the friction coefficient is assumed to be zero, the hold

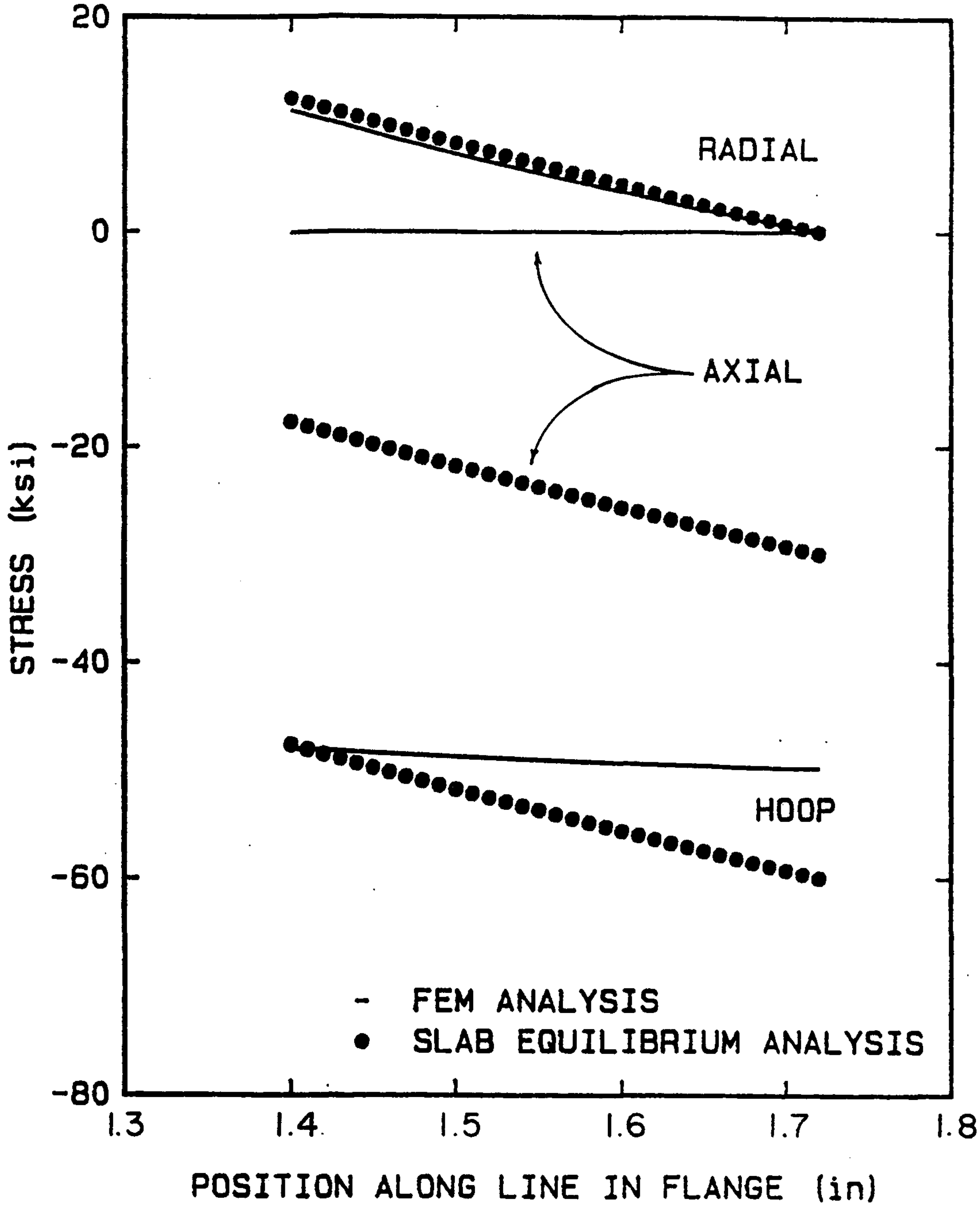

Figure 17 Comparison, based on FEM and slab equilibrium analyses, of stresses at the mid-thickness of the flange at a punch displacement of 0.75 inches.

down pressure is neglected and the thickness of the flange remains constant (implying a plane-strain condition), then with the use of the Von-Mises yield criteria the stress state at any point in the flange is [39]:

$$\sigma_R = -(2/\sqrt{3})(\sigma_o \ln(R/R_o) \quad (7)$$

$$\sigma_\theta = -(2/\sqrt{3})\sigma_o(1 + \ln(R/R_o)) \quad (8)$$

$$\sigma_Z = -(2/\sqrt{3})\sigma_o(1/2 + \ln(R/R_o)) \quad (9)$$

where R is the radial coordinate,
θ is the hoop coordinate,
Z is the axial coordinate,
σ_o is the flow stress of the material, and
R_o is the outer radius of the flange.

The slab equilibrium analysis assumed perfectly plastic material flow behavior. The FEM analysis assumed a step wise linear approximation of a strain hardening material. For a valid comparison between the two analyses, the flow stress of the sheet steel used in the analyses should be similar for a given value of plastic strain. At a punch displacement of 0.75 inches, the effective plastic strain in the flange region used in Figure 17 ranges from 0.20 to 0.14 as predicted by the FEM analysis. The average value of the effective plastic strain was 0.172. This value of effective plastic strain was used to estimate the corresponding effective plastic stress in the piecewise linear material flow stress approximation depicted in Figure 13. An effective plastic strain of 0.172 resulted in a approximate effective plastic stress of 51.9 ksi which was used as the flow stress for the slab equilibrium analysis. Using this value for σ_o in Equations (7)-(9), one can determine the stress states from the slab equilibrium analysis. The calculated values based on these equations also appear in Figure 17.

There is very good correlation between the slab equilibrium analysis and the FEM analysis for the radial stress as shown in Figure 17. The hoop stress from the FEM analysis is also in reasonable agreement with Equation (8). The largest discrepancy is the thickness stress. The thickness stresses determined by the FEM analysis are almost zero (a plane stress situation), but the corresponding compressive stresses determined by the slab equilibrium analysis range from about 20 to 30 ksi. The top platen in the FEM analysis was free to move upward due to the sheet thickening during deformation, however, the slab equilibrium analysis constrained the top platen from moving up to accommodate sheet thickening. The constraining of the sheet from thickening resulted in higher compressive stresses in the thickness as determined by the slab equilibrium analysis.

3.1.3 Evaluation of Stress Paths.

The FEM analysis not only determined the stresses in the flange region but also determined the workpiece stresses throughout the drawing process. The FEM analysis predicted stress states as a function of position through the thickness of the workpiece during drawing. The top, middle, and bottom elements located at a position which is initially in the flange region of the disk were monitored for the various stress states that occur during drawing. The radial, hoop and thickness stresses in the sheet steel were determined by the FEM analysis for top, middle, and bottom elements initially located at a radial position of 1.625 inches from the center of the punch. The stress states for the element were monitored as a function of punch displacement during the entire drawing process. The resulting hoop, radial and thickness stresses as a function of punch displacement are depicted in Figure 18a, 18b and 18c representing the top, middle and bottom elements respectively. The stress states in the flange region for all three thickness positions of the workpiece are similar. The hoop stresses are compressive and the radial

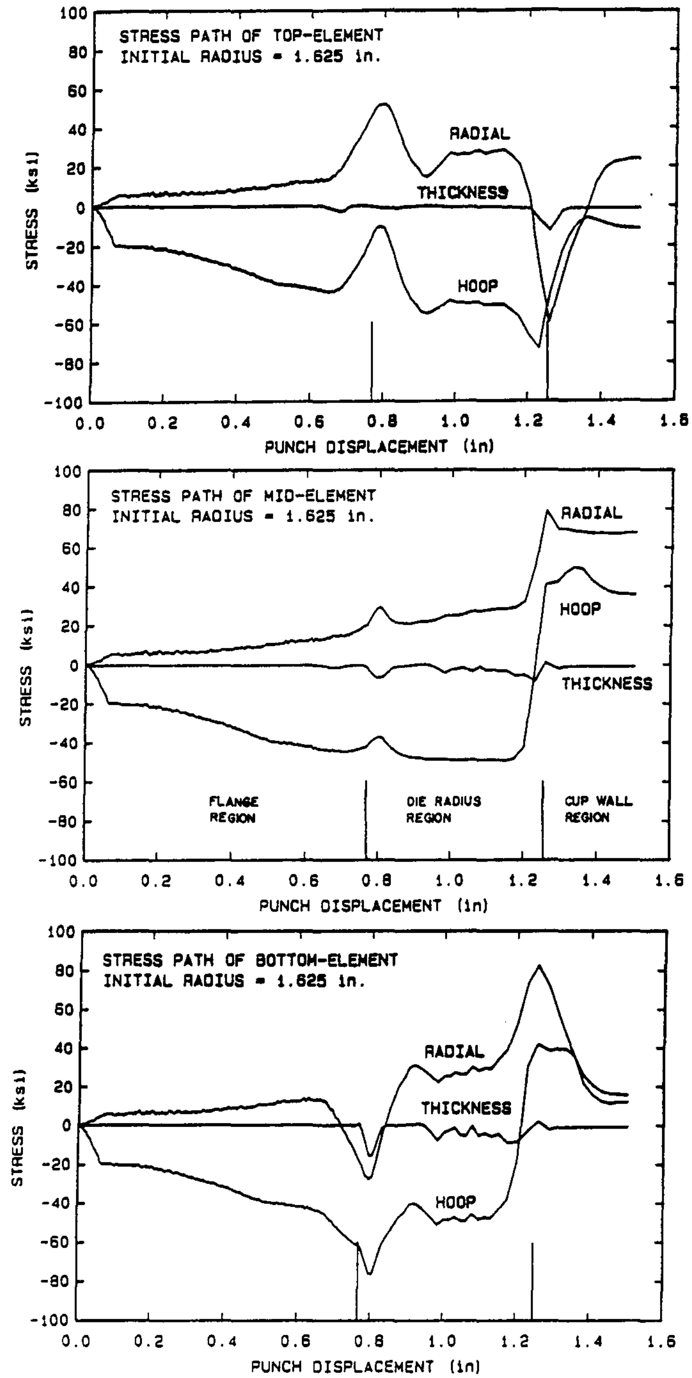

Figure 18 Stress history for elements on the a) top, b) middle, and c) bottom of the sheet which were initially at a radial position of 1.625 inches.

stresses are tensile. As the three elements enter the bottom die radius, the stress states vary as a function of sheet thickness. The tensile radial stress at the top of the sheet increases while the hoop stress becomes less compressive initially in the die radius region. The radial stress in the bottom of the sheet changes from tensile to compressive and the hoop stresses become increasingly compressive in the initial die radius region. The changes in stress states of the top and bottom elements of the sheet are typical of the bending process of a sheet around a radius, where the top of the sheet is in tension and the bottom of the sheet is in compression.

The stress states in Figures 18a-18c change at the transition between the die radius and cup wall regions. The radial stress of the top element changes from tensile to compressive and then back to tensile while, the hoop stress becomes less compressive. The radial stress of the bottom element remains tensile, however, the hoop stress changes from compressive to tensile. The stress states of the mid-element (Figure 18b) represent the uniform stress state predicted by slab equilibrium shown in Figure 10a for the flange and cup wall regions.

3.1.4 Stress in the Cup Wall.

Since the FEM analysis was performed with a sheet that had three elements across its thickness, the stress gradients across the sheet can be approximated. Figure 19 shows the hoop and radial stresses that exist across the thickness of the sheet at two different locations in the cup wall for a punch displacement of 1.20 inches. In contrast to the biaxial tensile state which is usually specified for the cup wall, these plots indicate that the inner surface of the cup is in biaxial compression. The radial and hoop stresses, which are compressive in this region, are in contrast to the rest of the cup wall thickness. This biaxial compression on the inner cup wall can be explained as follows. First, hoop compression is caused by the material being on the inside of a curved sheet conforming to the punch diameter. Second, the radial compression is due to the bending and unbending process associated with deformation at the die radius and material contacting the punch. It has not been determined if these stress states remain compressive once the drawn cup is removed from the punch.

The FEM analysis of the stress states during deep drawing provide critical information to help interpret the formability of the coatings. The calculated stress states

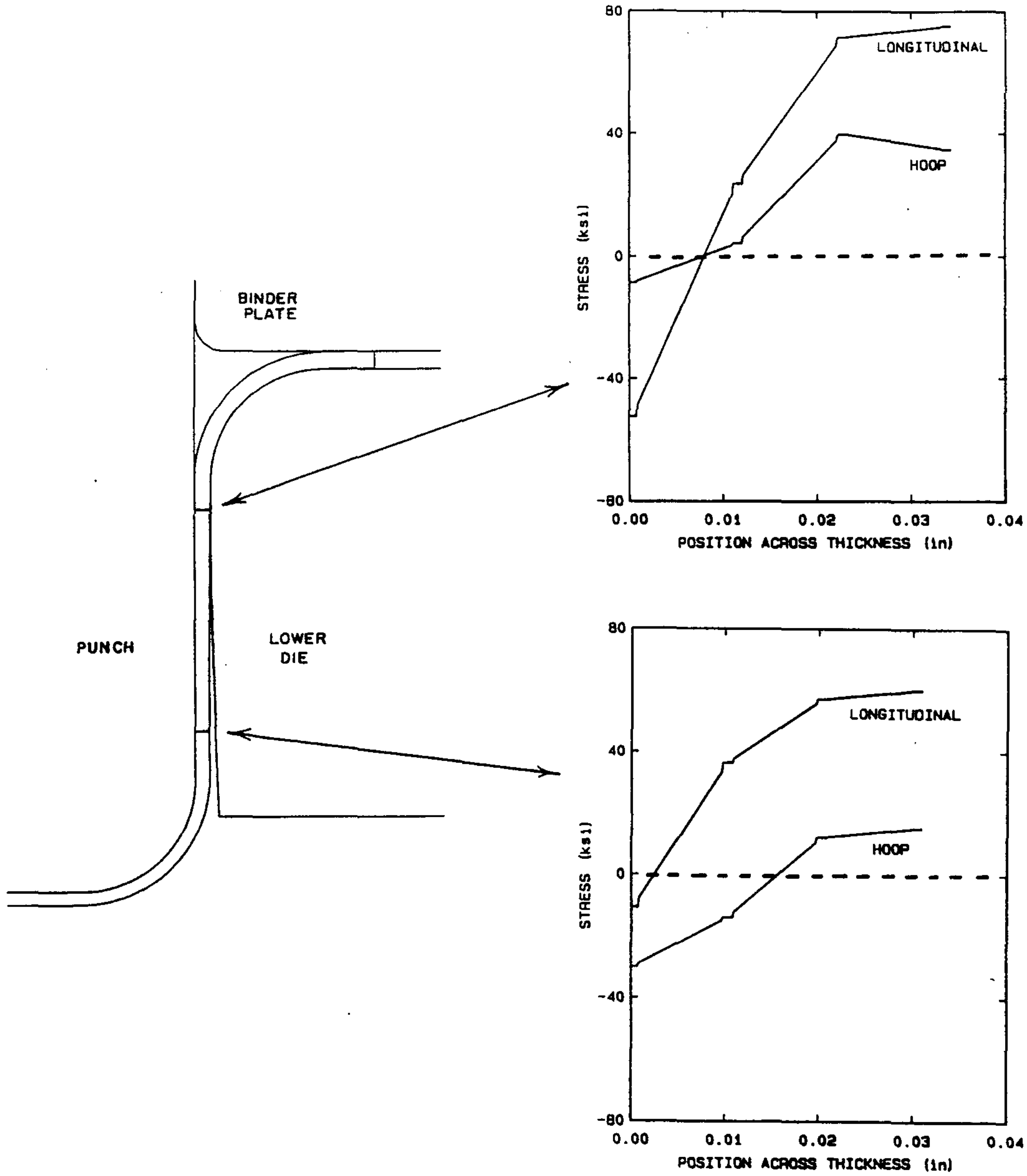

Figure 19 FEM analysis predictions for the hoop and longitudinal stresses across the thickness of the sheet in the cup wall at a punch displacement of 1.20 inches.

along with observations of the deformed coating will be used to evaluate the flow and fracture behavior of the coatings in the next section.

4.0 RESULTS AND DISCUSSION

The coating deformation characteristics of six coated sheet steels were examined utilizing cup drawing as the formability test. Responses of the coatings to stress and strain states during drawing were the major criteria used in evaluating the deformation of the coatings. Comparisons between the mechanical properties of the substrate are presented first in this section, followed by comparisons of the mechanical properties of the coatings. The changes in surface morphologies of the coatings due to deformation are then presented and discussed. Finally, models which depict the coating deformation processes are discussed.

4.1 Mechanical Properties of the Substrates and Coatings.

The mechanical properties of the substrate controls the overall formability of coated sheet steels [1]. Before evaluating the formability of the coatings, it is important to understand the overall formability of the coated sheet steels. Wilson [14], evaluated the uniaxial tensile mechanical properties of the six coated sheet products used in this investigation and his results are summarized in Table 2. The yield strengths of the coated sheet steels range from 22 to 31 ksi and the ultimate tensile strengths

Table 2 Summary of mechanical properties for the six coated sheet steels investigated [14].

Supplier	Sample*	Gage (in.)	Surface Roughness Ra	Yield Strength (ksi)	Ultimate Tensile Strength (ksi)	Percent Total Elongation
Stelco	70G70G	.028	33	31	48.6	42.2
Stelco	60HD	.032	54	30	49.9	41.0
Rouge	60G60G	.030	49	24	42.9	46.4
Rouge	40A40A	.049	**	22	41.2	44.2
Inland	70G70G	.028	34	30	46.5	41.3
Inland	60N40N	.030	63	23	43.6	42.4

Substrate ferrite grain size

Supplier	Sample*	Grain size (μm)
Stelco	70G70G	30
Stelco	60HD	22
Rouge	60G60G	46
Rouge	40A40A	44
Inland	70G70G	29
Inland	60N60N	39

* - Number indicates coating weight in g/m^2
G - Electrogalvanized coating
A - Zinc-iron electrodeposited alloy coating
HD- Hot dip coating
N - Galvannealed coating
**- Data not available
Ra- was determined by the Stelco arithmatic mean roughness values for the top side of the sheets

range from 41.2 to 49.9 ksi. The materials exhibited continuous yielding and similar deformation characteristics.

The ferrite grain size of each substrate material was measured by standard metallographic techniques, and the results (which are also summarized in Table 2) were correlated with Wilson's tensile data in the Hall-Petch plot presented in Figure 20. As expected from the Hall-Petch relationship, the yield strength increases with decreasing grain size.

The effect of grain size on the ultimate tensile strength was also evaluated on a Hall-Petch plot. The ultimate tensile strength versus the inverse square root of the grain size for the six coated products is shown in Figure 21. The ultimate tensile strength increases with a decrease in grain size. The Hall-Petch plots illustrate the strengthening contribution of grain boundaries.

The mechanical properties of the coatings are difficult to determine due to the nature of the coatings applied to the substrate. For composite materials, a rule of mixtures can be used to correlate composite strength with that of each component based on the summation of the volume fraction of each component multiplied by its corresponding strength. However, for the composite coated sheet steel,

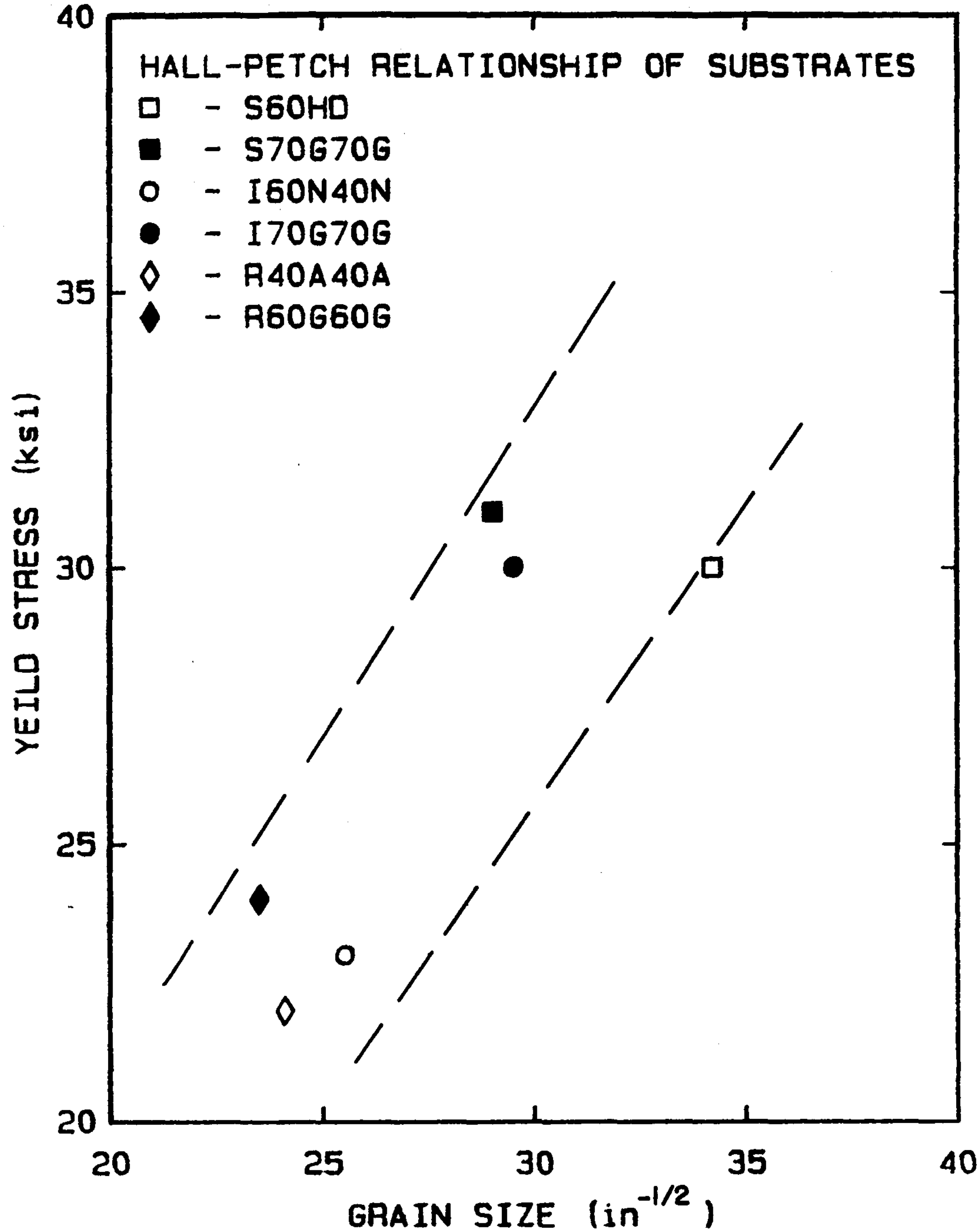

Figure 20 Hall-Petch relationship of yield stress versus inverse square root of ferrite grain size for the six sheet steels.

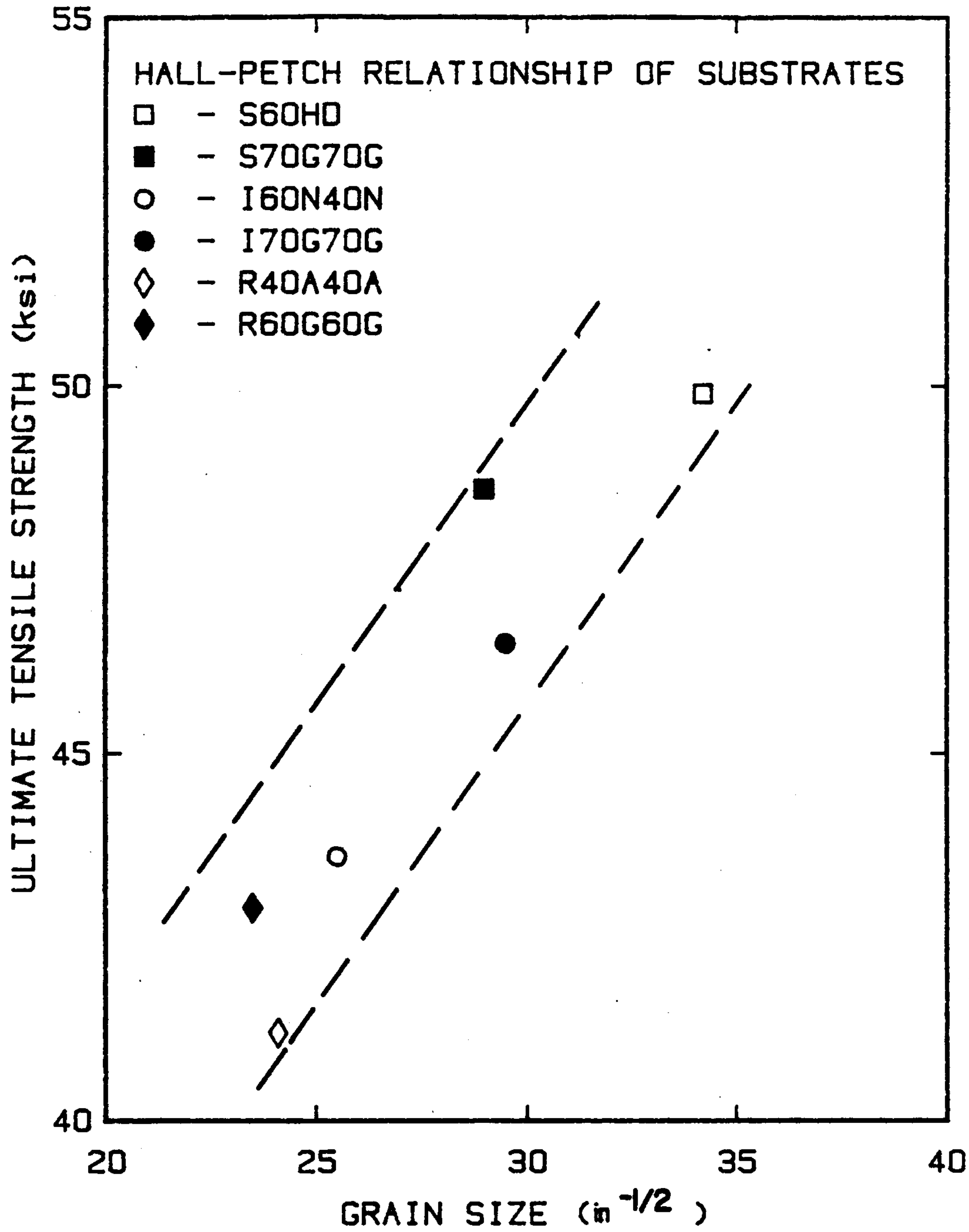

Figure 21 Hall-Petch relationship of ultimate tensile strength versus inverse square root of ferrite grain size for the six sheet steels.

the thin thickness of the coatings (about 10μm) limits the ability to determine the coating properties by the rule of mixtures. Because of the problems associated with the thin nature of the coatings, microhardness testing was utilized to evaluate the strengths of the coatings and to compare coating strength with that of the substrate. Hardness measurements are generally proportional to the ultimate tensile strength but also depend on the yield strength and plastic flow behavior. The plastic flow behavior is a function of the interaction volume generated during the test. Because of the plastic zone size resulting from the indention, it is recommended that the thickness of the material should be at least ten times the depth of penetration [6]. Since the thickness of the coatings is only 10μm, the microhardness of the substrates needs to be determined along with the corresponding hardness of the coatings.

The coating and substrate hardnesses of the six sheet steels under investigation were evaluated with a diamond pyramid micro-hardness tester. All tests were normal to the sheet surface. The microhardnesses of the polished substrates are plotted as a function of the depth of penetration in Figure 22. The microhardness values range from 100 DPH to 145 DPH. With an increase in applied load

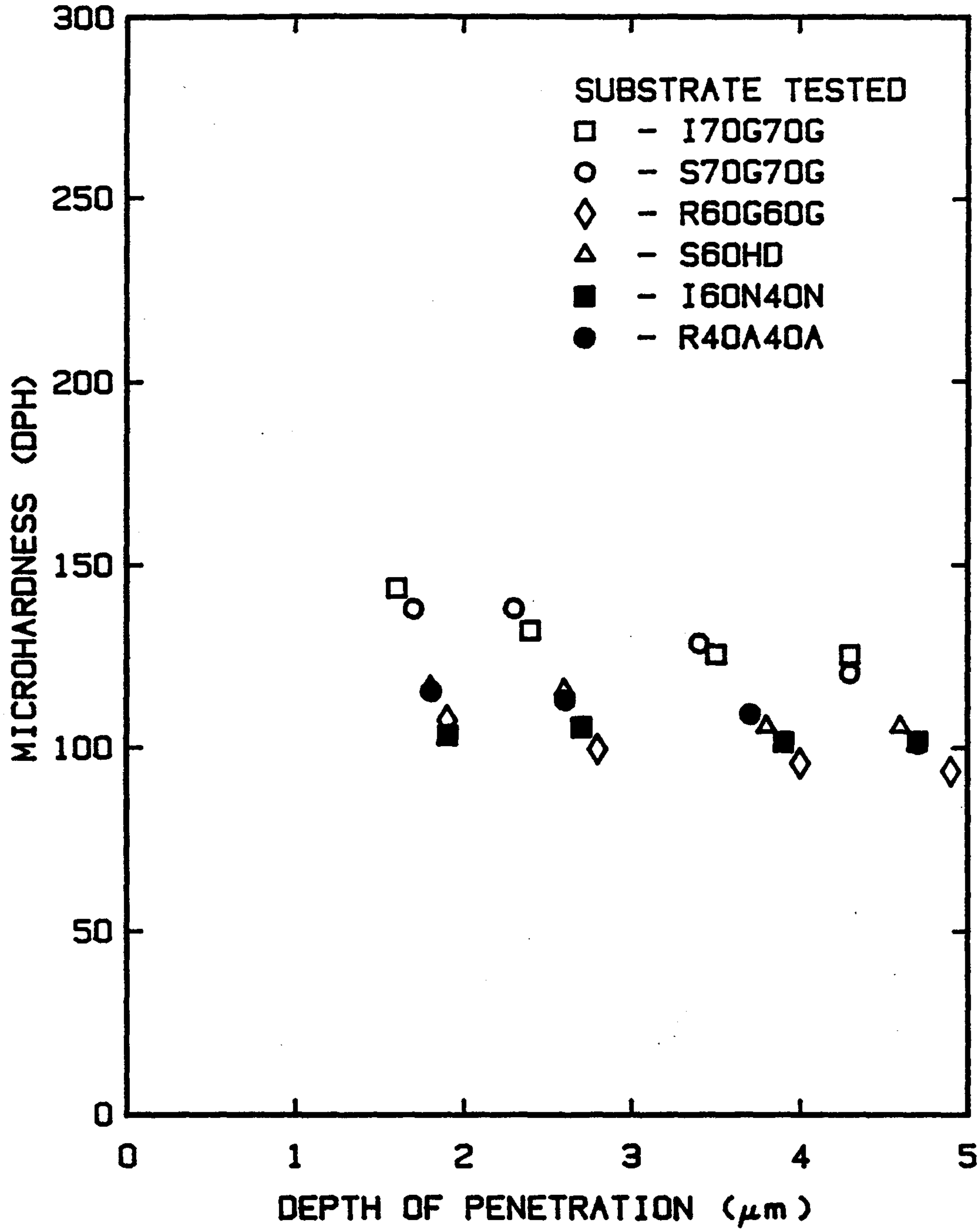

Figure 22 The substrate microhardness versus depth of penetration of the six coated sheet steels after the coating was removed by polishing.

the depth of indenter penetration increased. However, the microhardness was essentially independent of penetration depth.

The microhardnesses of the coatings were also evaluated as a function of depth of penetration of the indentor. Hardness tests were conducted on the as received material. Due to the rough surfaces of the coatings, it was difficult to evaluate the size of the indentions. The samples were polished with 1μm diamond paste and the hardness was monitored as a function of polishing, until a smooth surface was obtained. The values of the microhardness of the as received materials were within the standard deviation of the values obtained on the polished specimens. The resulting microhardnesses of the polished coatings versus depth of indentor penetration are shown in Figure 23. The microhardness values grouped into two separate ranges: pure zinc and alloy coatings. The zinc-iron alloy coatings exhibited higher microhardness than the pure zinc electrogalvanized and hot dip coatings.

As the depth of penetration approaches the coating thickness, the microhardness values of the alloy coatings approach the microhardness of the substrates indicating that the plastic zone size of the indention is dominated by the substrate. However, at low indenter penetration depths

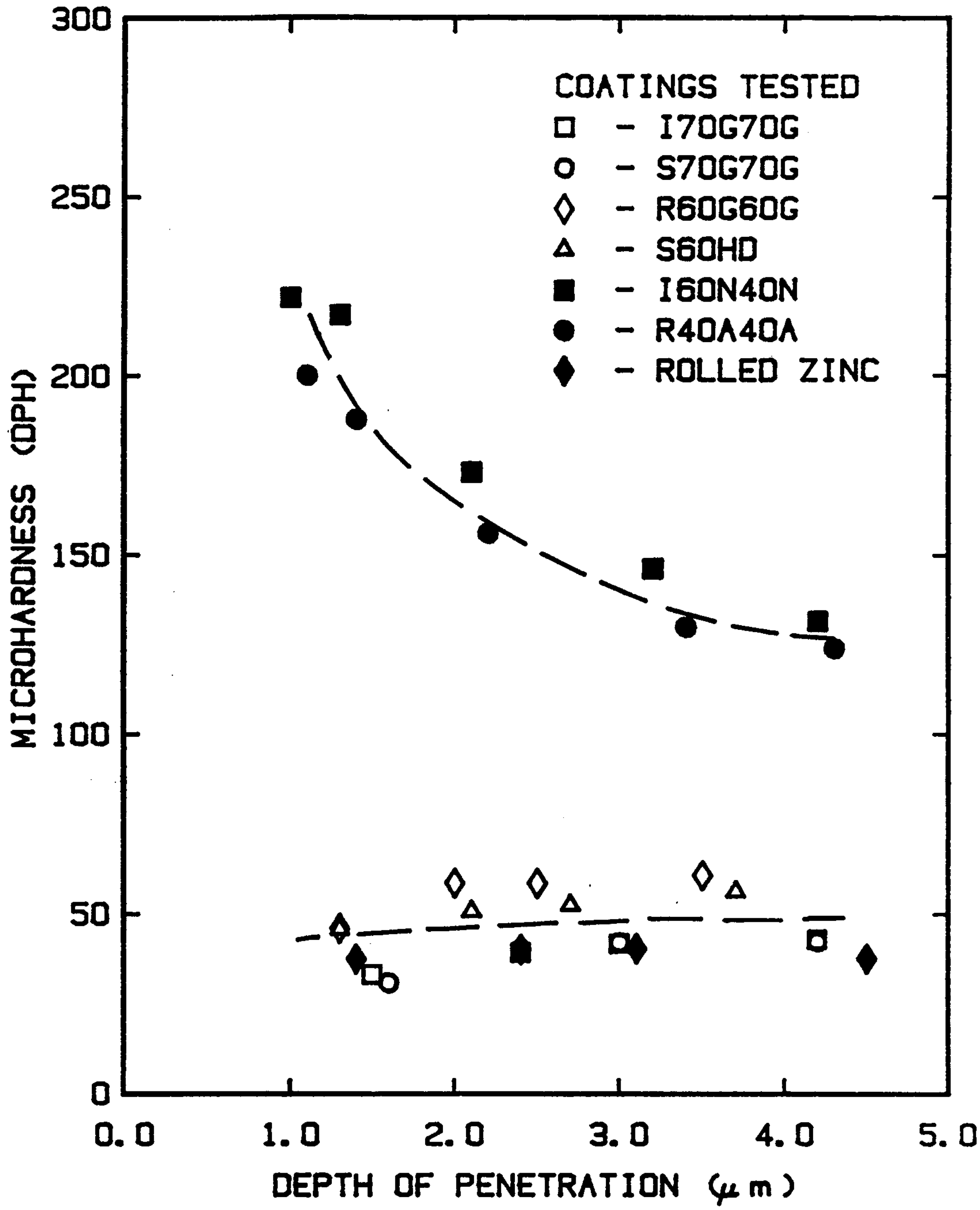

Figure 23 The coating microhardness versus depth of penetration for the six coated sheet steels. Hardness measurements on lightly polished surfaces.

the alloy coatings have a microhardness significantly higher than the substrate. The alloy coatings cracked at indentor penetration depths greater than 3μm indicating that the materials were brittle. The cracking of the alloy coatings may have also contributed to the reduction in hardness.

The pure zinc coatings have microhardness lower than the substrates. The pure zinc coatings did not crack during the microhardness testing.

In addition to the coating hardness values, Figure 21 included data on a bulk sample of recrystallized commercially pure zinc (zinc alloy Z-10, with a composition of 99% zinc and trace amounts of aluminum, rolled and annealed for two hours at 150°C). The hardness data on the bulk sample were similar to the pure zinc coatings. The similarity in hardness values for the pure zinc coatings and alloy Z-10, indicate that alloy Z-10 tensile data can be used to approximate the flow behavior of the coatings. The true stress versus true strain tensile data for alloy Z-10 as a function of testing temperature is shown in Figure 24. The alloy Z-10 exhibited brittle fracture characteristics at low test temperatures (77 K). However, as the test temperature increased, the yield strengths, ultimate tensile strengths, and strain hardening

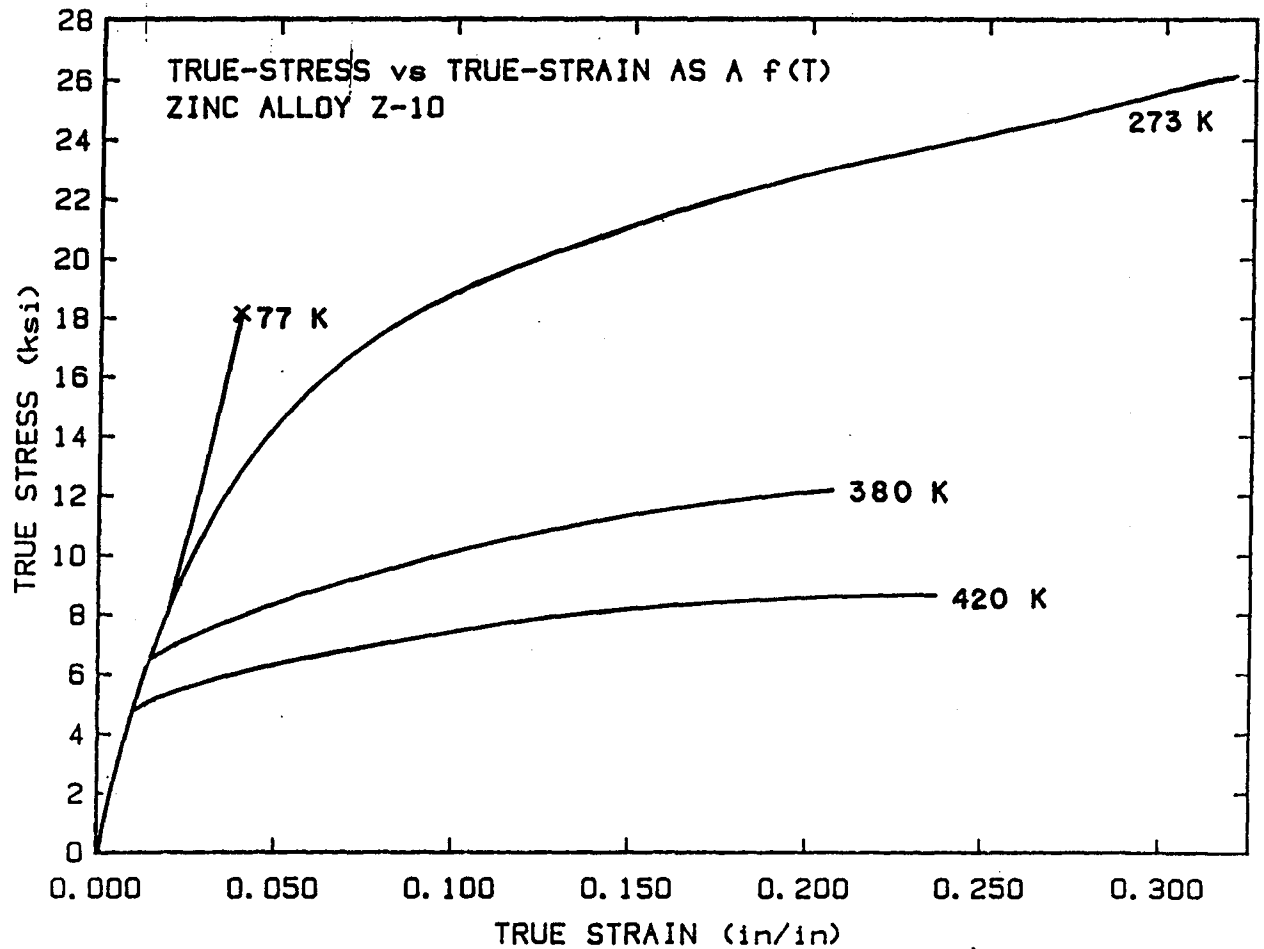

Figure 24 Effect of temperature on tensile stress/strain behavior of zinc alloy Z-10 at a strain rate of $0.027s^{-1}$.

behavior decreased, while the total elongation increased.

The strain rate sensitivity of alloy Z-10 was also monitored as a function of test temperature. The strain rate sensitivity was calculated by changing the strain rate, from $\dot{e}_1=0.027s^{-1}$ to $\dot{e}_2=0.0027s^{-1}$ during the tensile tests. The resulting values of strain rate sensitivity as a function of the test temperature normalized by the absolute melting temperature of zinc (T_{mp}=419.5°C) are shown in Figure 25. The strain rate sensitivity starts to increase at temperatures below room temperature and starts to level off at temperatures above 100°C. The higher the value of strain rate sensitivity, the more resistant the material is to localized necking [6]. The material will deform with diffuse necking and hence the post uniform deformation will increase. The strain-rate sensitive data and tensile data indicate that the plastic deformation behavior of the zinc coatings may change as a result of localized heating due to friction during stamping.

The mechanical properties of the substrates and coatings have been evaluated in this section. The differences between the mechanical properties will be incorporated with observations of the deformation characteristics of the coatings evaluated during cup

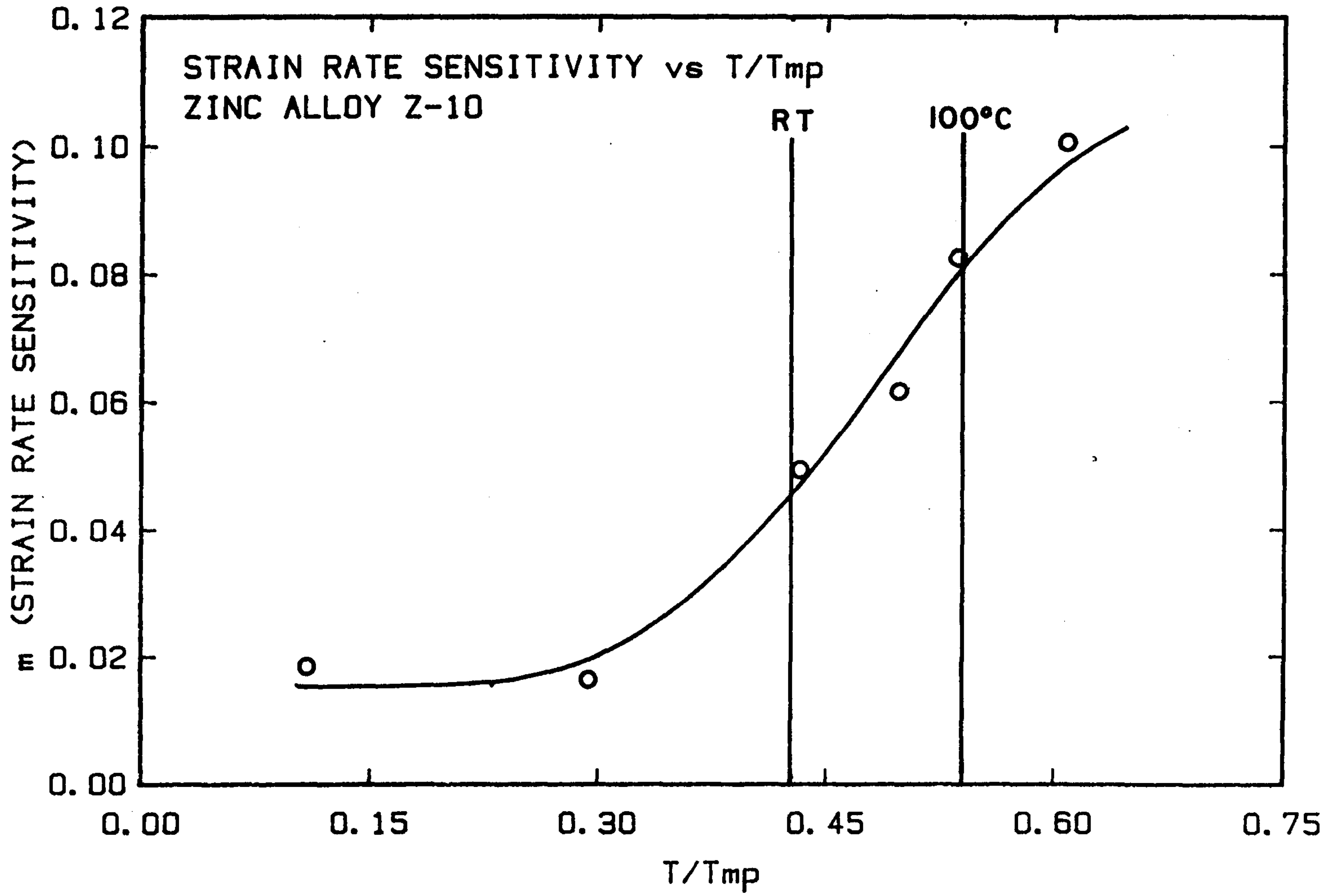

Figure 25 Strain rate sensitivity of zinc alloy Z-10 as a function of test temperature normalized by the melting temperature of zinc. Data obtained at a average strain rate of $0.077s^{-1}$.

drawing.

4.2 Changes in Surface Morphologies of Coatings.

The coating deformation characteristics resulting from cup drawing of the six coated sheets are presented and discussed in this section. The formability of the electrogalvanized coatings are presented first, followed by the hot dip, galvannealed and electrodeposited zinc-iron alloy coatings.

4.2.1 Changes in Surface Morphologies of Electrogalvanized Coatings.

The coating deformation characteristics of three pure zinc electrogalvanized coatings were investigated. The coated sheet steels tested under deep drawing conditions were: I70G70G, S70G70G, and R60G60G (Table 2). The undeformed surface microstructures of the three electrogalvanized coatings at two magnifications are shown in Figure 26 where; 26a and 26b, 26c and 26d, and 26e and 26f, represent Inland, Stelco and Rouge products respectively. The surface morphologies of the Inland and Stelco electrogalvanized coatings are similar, with plate like structures resulting from growth planes representing the majority of the microstructure. Surface grains are

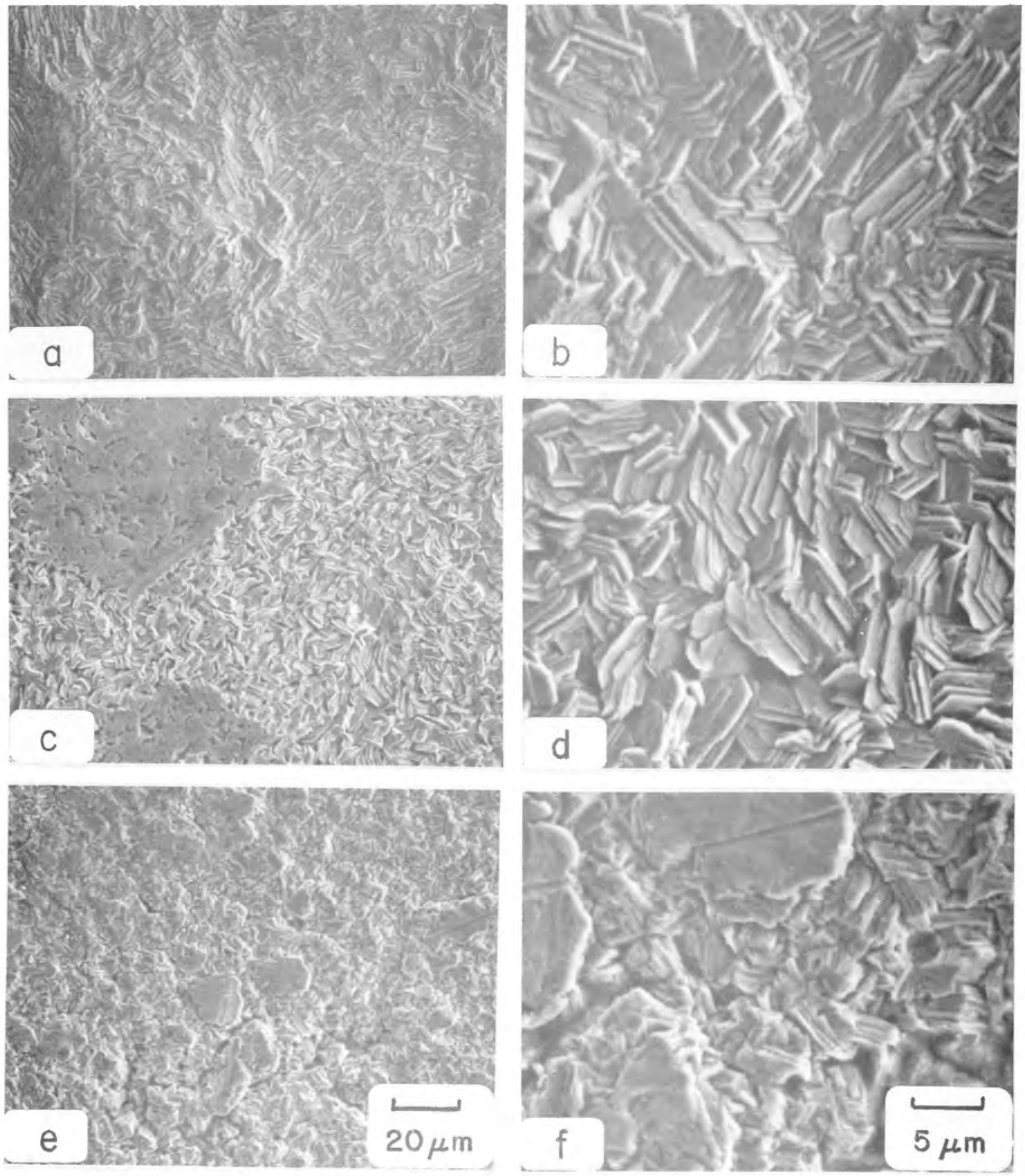

Figure 26 The surface morphologies of the as-received electrogalvanized coatings: a) and b) I70G70G, c) and d) S70G70G, and e) and f) R60G60G at two magnifications (SEM micrographs).

distinguished by orientation changes in the parallel growth planes. The plate structure of I70G70G has sharply defined corners compared to the plate structure of S70G70G which has fewer defined corners. Portions of the S70G70G electrogalvanized coating were flattened (Figure 26d) during the coating process. The coating morphology of the Rouge product was distinctly different than that of the other two suppliers. The surface morphology of R60G60G resembles a randomly oriented crystal structure. The differences in coatings microstructures is a result of the different depositional techniques used by each supplier.

The coating deformation characteristics of I70G70G and S70G70G were similar during cup drawing. Both coatings plastically deformed to accommodate the extensive strains during drawing. Because of the similarities in plastic deformation between the two coatings, only the deformed microstructures of the I70G70G will be presented.

Changes which develop during drawing in surface microstructures of the I70G70G are shown in Figure 27. Surface micrographs illustrate deformation in the flange (Figure 27a), the outside die mid-radius (Figure 27b) of partially drawn cups, and the inside cup wall (Figures 27c and 27d) of fully drawn cups. The drawing direction of the micrographs is horizontal and to the right in Figure 27.

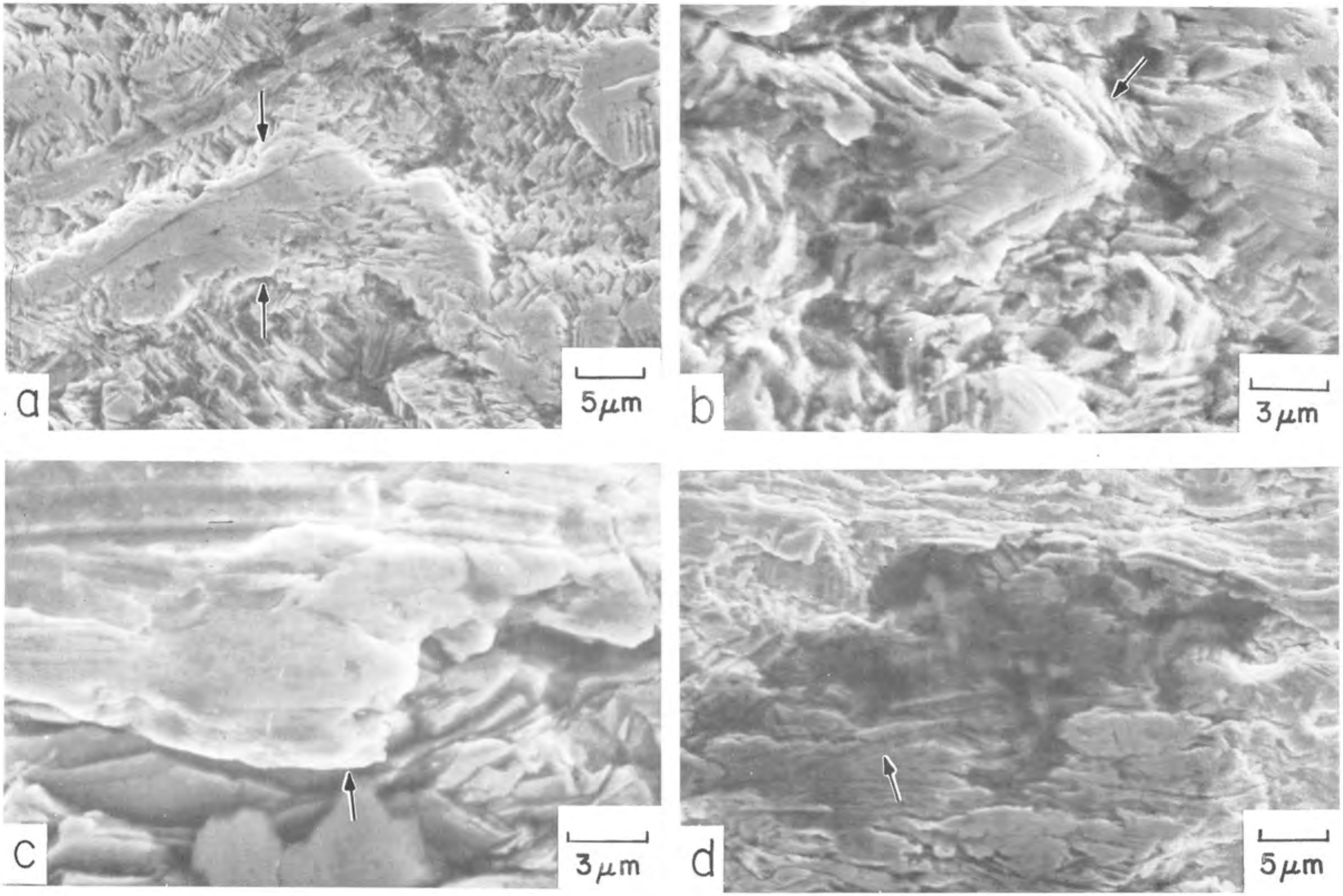

Figure 27 The deformed surface morphology of I70G70G at a) flange region, b) outside die radius of partially drawn cups, c) and d) inside cup wall of fully drawn cups (SEM micrographs).

Coating deformation in the flange region must accommodate compressive strains in the hoop direction and tensile strains in the drawing direction. To accommodate the compressive strains, zinc crystals preferentially oriented for slip perpendicular to the sheet surface thicken, which relieves the compressive stresses on adjacent crystals. Preferential crystal thickening is shown between the arrows in Figure 27a, where a zinc grain or group of grains have thickened and contacted the binder plate resulting in a smeared microstructure. The surrounding grains still maintain a similar microstructure to that observed in the undeformed state. Figure 27b shows coating deformation typically observed at the outside die radius of a partially drawn cup. During deformation, some coating grains thickened and elongated in the drawing direction due to tensile strains associated with the bending process (see Figure 18a). The coating in this area is not in contact with the binder plate or the punch so free surface deformation is possible.

The I70G70G and S70G70G coatings are capable of accommodating extensive strain without fracture. The extensive plastic flow characteristics of the I70G70G coating is shown in Figure 27c with a microstructure typically found on the inside cup wall of a fully drawn sheet. The arrow points to a region which was flattened by contact with the binder plates and punch. The observed morphology results in overlapping of deformed zinc crystals. The thickened structure observed on the inside surface in Figure 27c represents the final structure of the feature identified in the partially deformed flange in Figure 27a.

The hole in the coating shown in Figure 27d represents a region where zinc was removed in the forming operation. Observations of the surface features on the zinc within the hole indicated that failure, in some areas, occurred by cleavage. It is probable that the hole shown in Figure 27d resulted from the removal of a thickened zone, like that shown in Figure 27c. Energy dispersive spectroscopy (EDS) analysis showed that the material at the bottom of the hole was zinc. Removal of the coating in this fashion is considered powdering. The coating microstructures on the outside cup wall of fully drawn cups were smeared smooth due to sliding around the die radius. The smearing of the coating is probably a consequence of the high contact pressures associated with deformation over the die radius.

The R60G60G coating exhibited substantially different deformation characteristics to that observed for the I70G70G and S70G70G coatings. The deformation characteristics of the R60G60G coating in the flange of a partially drawn cup and along the inside cup wall of a fully drawn cup are shown in Figures 28a and 28b respectively. The drawing direction is horizontal and to the left for the micrographs in Figure 28. The deformed coating in Figure 28a has cracked to accommodate the plastic tensile strains during drawing. The cracked coating exposed the substrate. The cracks in the coating are perpendicular to the maximum tensile stress orientation which is consistent with brittle fracture in tension. The microstructure of the coating between the cracks is relatively undeformed and almost identical to that observed in the as received condition (Figure 26e and 26f). This suggests that the coating simply cracks to accommodate substrate deformation.

The coating morphology observed on the inside cup wall of a fully drawn cup is shown in Figure 28b. The coating has smeared in some areas due to contact with either the top platen or the punch. The other coating morphologies appear to have been compressed in the hoop direction. The cracked coating and exposed substrate is still evident in the fully drawn condition.

The microhardness data presented in Figure 23 along with the tensile data provided by the zinc alloy Z-10

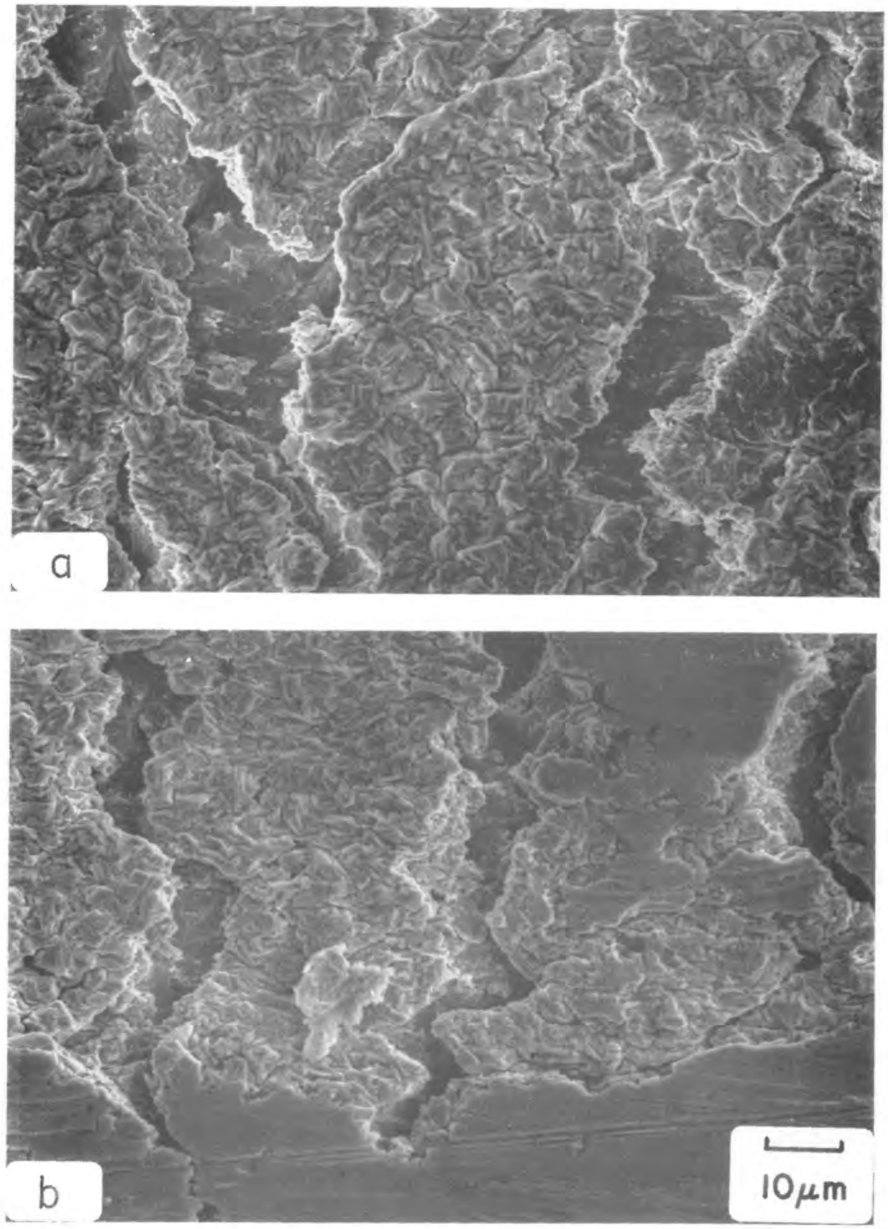

Figure 28 The deformed surface morphology of R60G60G at the a) flange region and b) inside cup wall (SEM micrographs).

suggested that all of the electrogalvanized coatings should deform similarly and have good ductility. The previous figures showed that two of the coatings exhibited good ductility but the third coating exhibited brittle characteristics. To explain the differences in coating deformation characteristics between the ductile I70G70G and S70G70G coatings and the brittle R60G60G coating, x-ray diffraction was performed on the as-received and deformed coatings to evaluate the crystallographic texture of the zinc coatings. The results of the coating texture analysis are presented in Table 3. The first column in Table 3 represents the crystal plane that satisfied Bragg's law of diffraction at an orientation parallel to the sheet surface. The second column represents the orientation of the basal plane from the diffracted plane shown in column 1. The remaining columns represent the relative peak intensities normalized by the maximum diffracted intensity for the plane indicated. The results show that I70G70G and S70G70G have similar as-received textures with a maximum intensity corresponding to the $(10\bar{1}3)$ plane. However, the maximum intensity of the as received R60G60G corresponds to the $(10\bar{1}1)$ plane which is the same as the random powder pattern. The texture analysis of partially drawn cups in the flange region show that for I70G70G the

Table 3 Texture analysis of electrogalvanized coatings.

Diffracted Plane[1]	Orientation of Basal Plane[2]	I70G60G	I70G70G Flange	S70G70G	R60G60G	R60G60G Flange	Random Powder[3]
(0001)	0°	69	100	15	19	21	53
$(10\bar{1}0)$	90°	3	4	5	24	25	40
$(10\bar{1}1)$	65°	26	21	91	100	100	100
$(10\bar{1}2)$	47°	22	37	66	10	10	28
$(10\bar{1}3)$	35°	100	67	100	13	9	35
$(11\bar{2}0)$	90°	54	--	55	21	14	21
$(11\bar{2}2)$	62°	7	--	30	7	8	23

[1]-The zinc crystallographic plane that satisfied diffraction requirements parallel to the sheet.
[2]-The orientation of the basal plane from the sheet surface for the diffracted plane.
[3]-Diffracted intensities for a random powder sample from scraping the coating off of the sheet [33].

crystallographic plane with the maximum intensity has shifted from $(10\bar{1}3)$ to (0001) zinc. This is consistent with other work performed on electrogalvanized coatings deformed in uniaxial tension resulting in a rotation of the basal plane towards the tensile axis indicating deformation by slip [33]. However, texture analysis on the partially drawn R60G60G coating showed that the intensities of the diffracted planes did not change from the as received condition. The absence of change in texture corresponds to the absence of plastic deformation of the coating observed in the microstructures of the as received and deformed coating shown in Figure 26f and Figure 28a.

The deformation behavior of the coating can be related to the average orientations of zinc basal planes in the coating. The diffraction peak with the maximum intensity corresponds to a coating with a sufficient number of planes with the same orientation that will affect the formability of the coating. The crystallographic plane corresponding to the maximum intensity is the $(10\bar{1}0)$ for R60G60G and the $(10\bar{1}3)$ for I70G70G and S70G70G coatings. If it is assumed that the measured intensities relate to the number of grains with orientations described by the diffracting plane, then it can be assumed that a significant fraction of basal planes in R60G60G are inclined at about 65 degrees to the surface and I70G70G and S70G70G have basal planes inclined at about 35 degrees. For the thin coating on the sheet steel, the deformation axis of the coating is parallel to the sheet surface. Safranek [40], reported that the ductility of single-crystal zinc depends upon the orientation of the basal plane of the zinc with respect to the deformation axis. If the basal plane is between 40 and 60 degrees of the deformation axis, the zinc crystal is ductile and will deform by slip. At angles below 40 degrees the zinc crystal will deform by either slip or twinning. At angles above 60 degrees the zinc crystal cleaves along the basal plane. Therefore, based on Safranek results, the ductility of electrodeposited zinc will depend upon the predominate orientation of the deposited zinc crystals. If sufficient zinc crystals are oriented such that the basal plane is at least 60 degrees from the sheet surface, then the coatings would crack which was observed with the R60G60G coating.

Inspection of the dies after forming the three electrogalvanized coated sheet steels revealed extremely small fragments of zinc that were removed from the coatings. The die radius appeared to have the highest concentration of fragments, which also corresponds to the region of highest contact pressures. The zinc fragments were easily wiped off of the dies and showed no indication that galling had occurred. Other investigations [41,42] have shown that electrogalvanized coatings will gall if the contact pressure between the coating and die reaches a critical value which is dependent on the lubricant used during forming. Unlubricated forming tests performed on the I70G70G, S70G70G and R60G60G have shown that these materials will gall under certain conditions [43]. Since the substrates of the electrogalvanized coatings were not exposed (other than by crack widening) which would indicate flaking, the fragments of zinc found on the die are believed to be a result of powdering. The limited amount of coating loss observed during drawing is consistent with that found by others using tape tests to evaluated powdering and flaking of electrogalvanized coatings [28,29].

In summary, the deformation characteristics of the electrogalvanized coatings investigated during cup drawing were dependent on the texture of the as deposited coating. Deposition techniques resulting in unfavorable crystal orientation for slip, can result in cracking of the coating during deformation.

4.2.2 Changes in Surface Morphologies of a Hot Dip Coating.

The deformation characteristics of a hot dip pure zinc coating (S60HD) were evaluated during cup drawing. The surface morphology of the as-received coating is shown in Figure 29 at two magnifications. The surface morphology of the hot dip coating consists of broad valleys and plateaus in place of the well defined crystal structures of the electrogalvanized coatings shown in Figure 26. The adhesion of the hot dip coating to the substrate is via diffusional bonding of the molten zinc with the iron. The intermetallic formed through the bonding process grows until the sheet exits the molten zinc bath. The liquid zinc remaining on the intermetallic surface solidifies. Air knives are used to control the thickness of the coating. The size and type of the resulting solidification structure or spangle along with the use of air knives results in the type of surface morphology of the coating. The as-received coating exhibited a few microcracks which is consistent with other investigations on hot dip coatings [28,44].

The deformation characteristics of the hot dip coating are shown at three locations of fully and partially drawn cups in Figure 30. The drawing direction is horizontal and

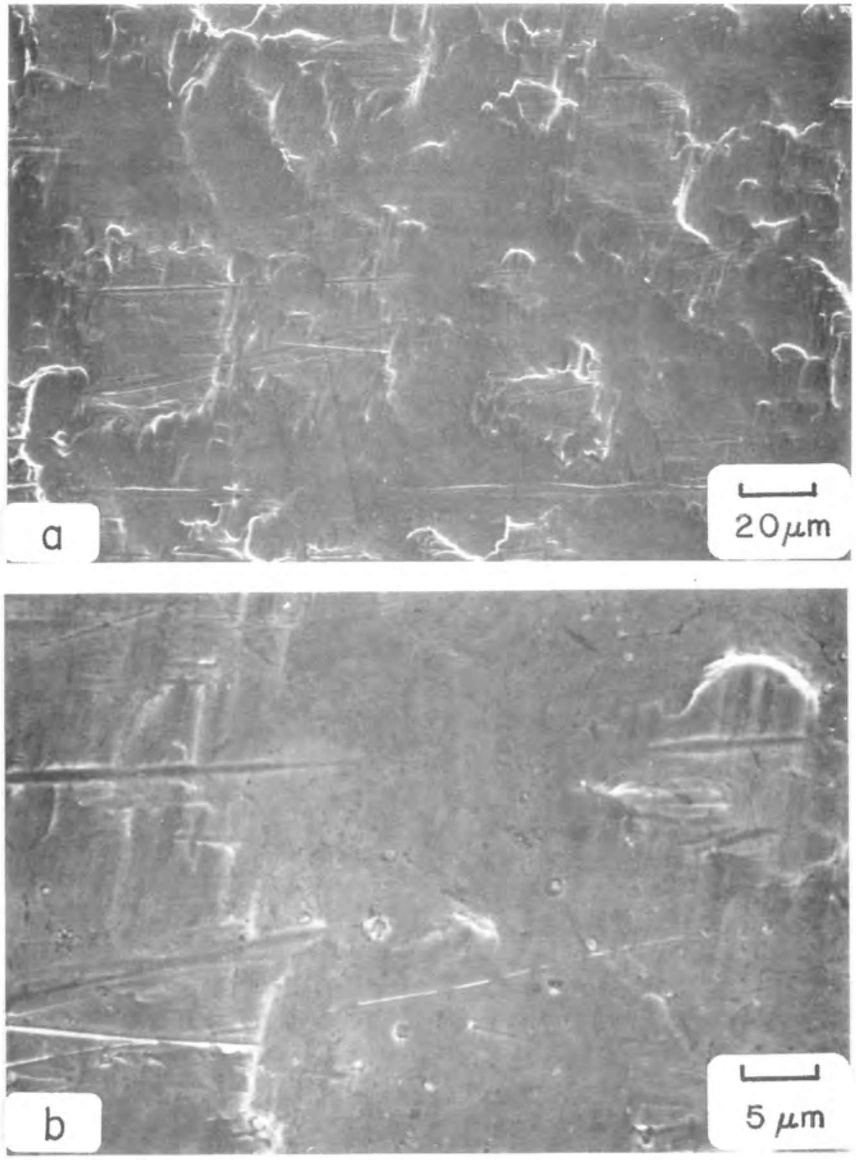

Figure 29 The surface morphologies of as-received S60HD at two magnifications (SEM micrographs).

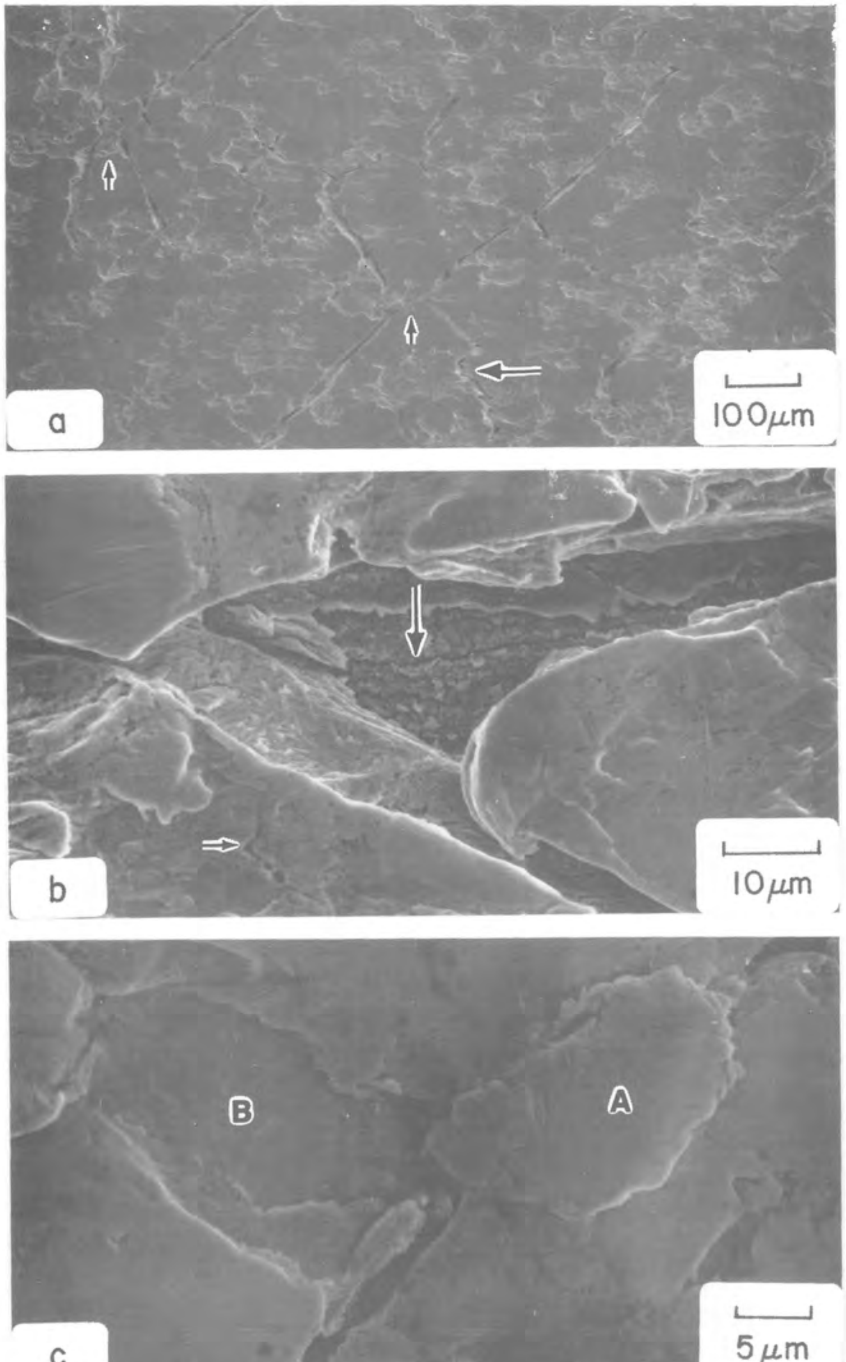

Figure 30 The deformed microstructure of S60HD on the outside cup wall of fully drawn cups (a) and (b), and the inside die radius region of a partially drawn cup (c) (SEM micrographs).

to the left for all of the micrographs in Figure 30. Figure 30a shows a typical coating morphology found on the outer surface of a fully drawn cup. This micrograph was taken at the mid-height of the cup wall. The small arrows point to cracks in the coating that resemble "x's". The large arrow points to a crack which changes direction several times; nevertheless, the crack tries to maintain an orientation similar to the "x" pattern. X-type cracks with similar orientations were observed throughout the cup wall. However, the geometry of the x-patterns varied with position. Near the punch nose the x-patterns were slightly compressed in the drawing direction, while at the top of the cup the x-patterns were elongated in the drawing direction. Regions between the major cracks exhibited microcracking to accommodate the imposed strain.

Figure 30b shows the center of an "x" type crack. This micrograph was taken at the 3/4 height of the outside cup wall and shows how the crack geometry has elongated in the drawing direction, as mentioned above. The large arrow points to a crack located in the zinc-iron interface. It has been reported that hot dip coating cracks may nucleate from cracks obtained in the relatively brittle zinc-iron interface [11,45]. It appears from this micrograph that the crack nucleation point for the coating would arise from the crack found in the intermetallic interface. However, upon examination of the stress states for this micrograph, the tensile stress is horizontal and parallel to the crack in the intermetallic interface. This crack orientation is not what would be expected for the imposed stress state. A crack oriented perpendicular to the tensile stress state would be expected.

Particle A in Figure 30c was interpreted to be located originally in the area denoted by the letter B. Inspection of the surface area B shows characteristics of a cleavage fracture plane which is the basal plane (0001) for zinc. This micrograph was taken on the outer cup wall of a partially drawn cup at the die mid-radius where a maximum compressive stress state in the radial direction is obtained due to bending. Removal of a particle of this size would be considered powdering. Other small particles similar to that found in Figure 30c were observed on the dies.

The flange of a partially drawn cup was inspected to determine the mechanisms of crack nucleation observed in the coating. Figure 31 shows a series of cracks located in the flange of a partially drawn cup. The drawing direction is horizontal and to the left. The letter "i" designates aluminum-rich inclusions identified by EDS analysis with

Figure 31 The deformed microstructure of S60HD in the flange region of a partially drawn cup (SEM micrograph).

the SEM. It should be noted that aluminum inclusions were not found in every crack in the flange. However, the cracking adjacent to the inclusions is oriented perpendicular to the radial direction or maximum tensile stress. The cracks near inclusions have opened more in the radial direction than the cracks without inclusions. Inclusions have been shown to be sites of crack initiation where decohesion of the particle and matrix occurs [45]. Metallographic inspection of cryogenic fracture surfaces for fully drawn specimens determined that the aluminum inclusions were found near or on top of the zinc-iron interface.

Aluminum is an alloying element added to the zinc bath to restrict the thickness of the intermetallic alloy layer, which optimizes coating adherence [1,19]. Cameron and Harvey [20] reported that aluminum exhibited some solubility in both the liquid and solid zinc. This limited solubility of aluminum in zinc would account for the presence of aluminum-rich inclusions in the zinc bath which could becomes trapped in the coating during solidification. The zinc crystals solidify in a direction parallel to the sheet. During solidification, impinging grains could continue to grow on top of each other [19]. This type of growth could explain how the inclusions become entrapped during the hot dip processing.

The small arrows in Figure 31 point to regions where one side of the coating appears to be pushing up over the top of the coating on the other side of the crack. The compressive strain is oriented vertically in Figure 31. If the coating is ductile and the zinc-iron interface provides sufficient bonding, the coating can accommodate the compressive strain by thickening, and although cracking may occur, the coating will not flake off. If the coating is relatively brittle and the bonding to the substrate is insufficient, then flaking will occur and large areas of substrate will be exposed. Flaking of the hot dip coating was not observed during deep drawing. However, surface examination with stereo-microscope of a partially drawn cup revealed what appeared to be cracks in the coating that started to separate the coating from the substrate due to the applied compressive strains. The separation of the coating from the substrate was not observed in the flange region but appeared to begin in the die radius region on the inside of the cup or tensile side of the bending sheet. The cracks appeared to heal themselves upon straightening of the cup wall after deforming over the die radius.

Inclusions found in the coating are responsible for crack nucleation for cracks which propagate perpendicular to the maximum tensile stress. However the crack orientation changes direction and results in x shaped cracks. The orientation of x shaped cracks corresponds to planes of maximum shear stress parallel to the sheet surface. The crack orientations along planes of maximum shear stress indicate that preferentially oriented inherent weaknesses in the coating result in crack propagation.

To examine possible inherent weaknesses in the coating, deformed and undeformed coatings were polished and etched. Figure 32 shows the undeformed microstructure of the hot dip coating at two magnifications. Figure 32a shows the typical spangle structure of the coating with shinny and frosty regions. Figure 32b shows a magnified view at a spangle boundary of the structure in Figure 32a. Some spangles had a dendritic structure that would be expected, but other spangles contained what appeared to be individual grains that resembled a wrought structure. The spangle boundaries are clearly defined in Figures 32.

The flange of a partially drawn cup was polished and etched. The resulting microstructures of the partially drawn cup are shown in Figure 33. The drawing direction is oriented vertically and to the top of Figure 33. Figure 33a shows the cracks in the coating of a polished but

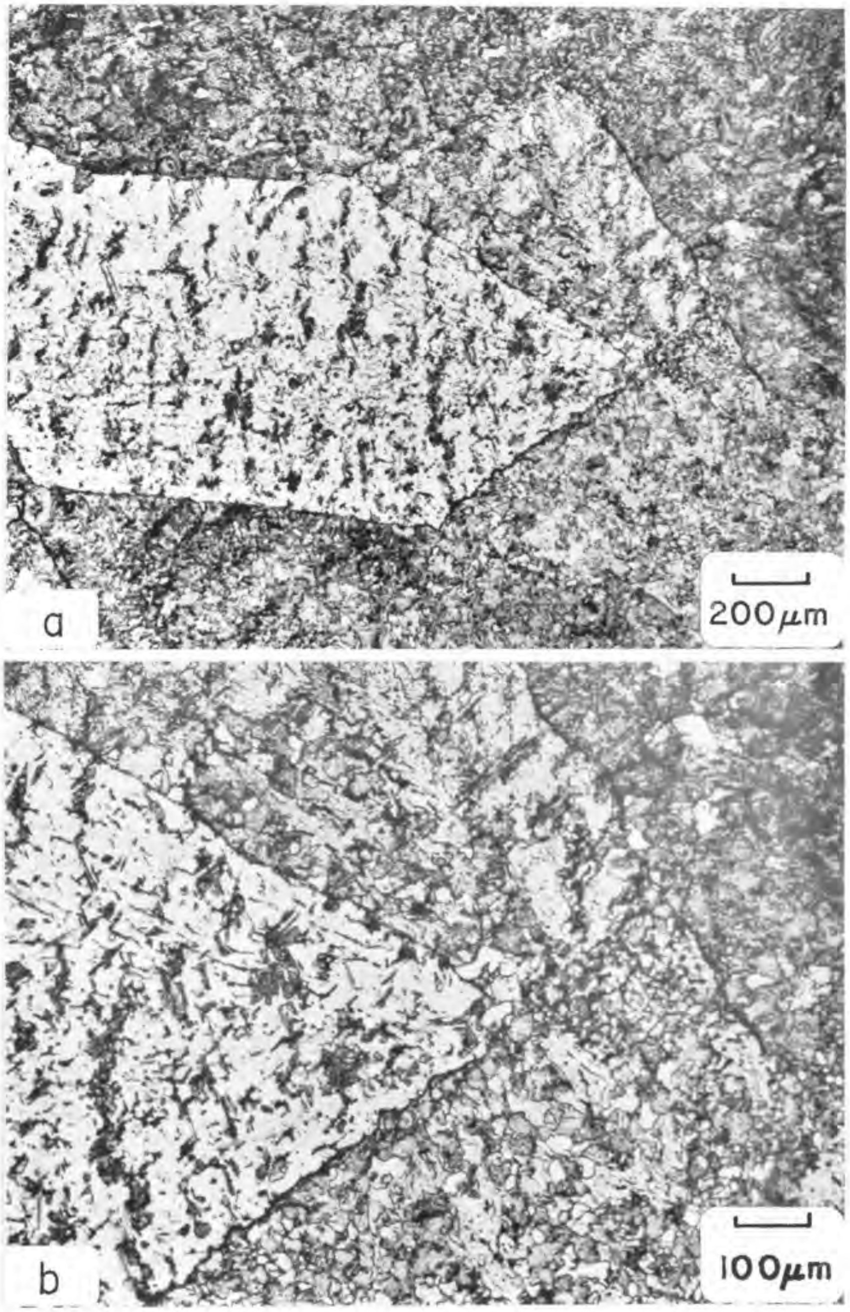

Figure 32 The as-received microstructure of S60HD coating showing spangle boundaries at two magnifications (Light micrographs, CrO_3, Na_2SO_4 aqueous etch).

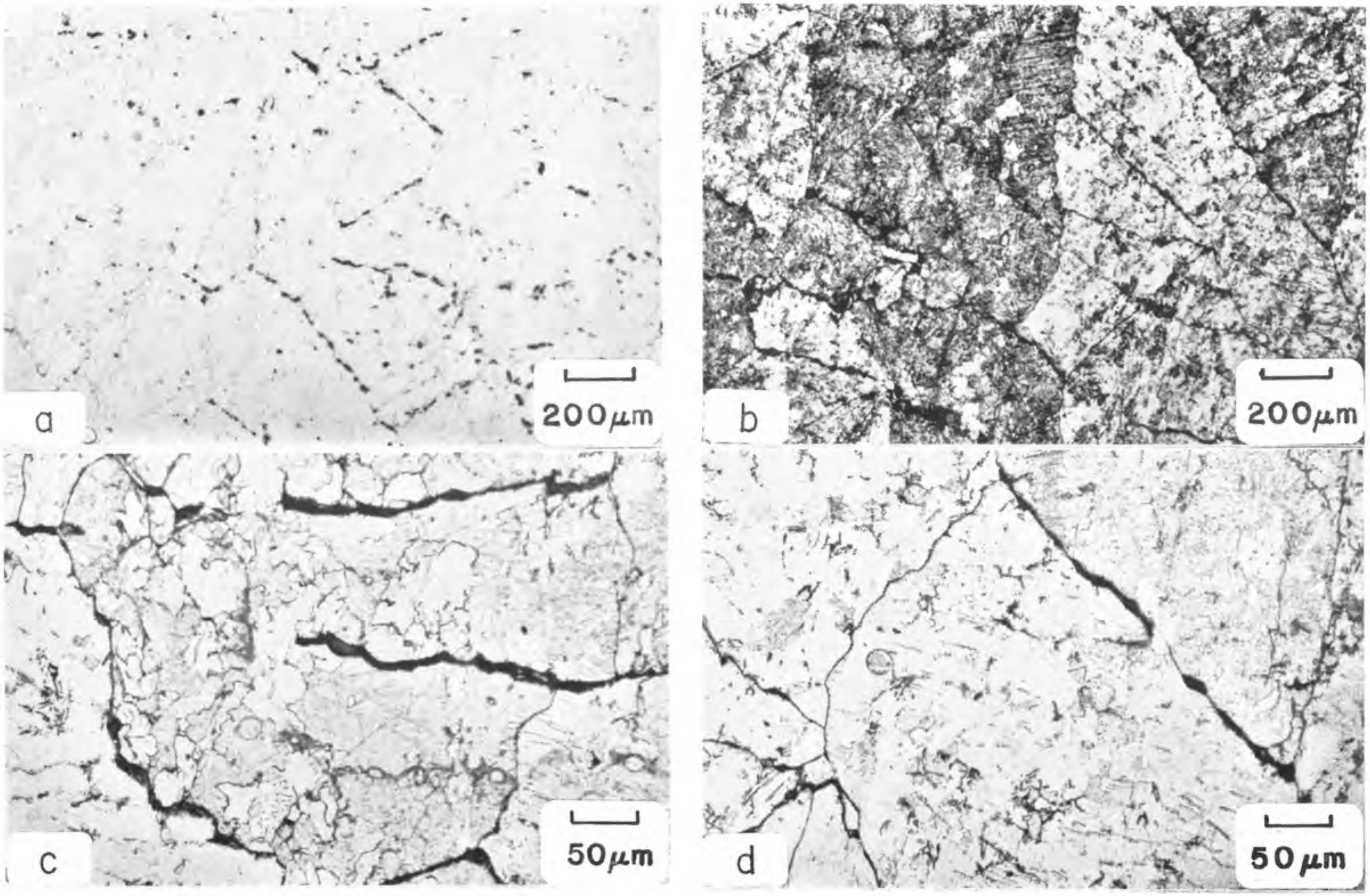

Figure 33 Deformed coating microstructure of S60HD in the flange region of a partially drawn cup. Micrograph a is unetched showing the crack orientations while micrographs b is etched. Micrographs c and are higher magnifications showing intra- and inter-spangular cracking.

unetched coating. The cracks appear to maintain the orientation of maximum shear. Figure 33b shows the etched microstructure of the coating with the orientation of the cracks. Examination of the deformed microstructure at higher magnifications showed that the microstructure resembling a wrought material exhibited interspangular and intraspangular cracking (Figure 33c). The intraspangular cracks were oriented perpendicular to the tensile axis. In some cases the cracks did not propagate though the entire spangle. The formation of cracks for shinny spangles was entirely interspangular and preferentially oriented along planes of maximum shear (Figure 33d). It has been shown that inter- and intra-spangular cracks can exist in the as-received coating, and upon deformation these cracks will widen or new cracks will nucleate [28,44]. The difference in the type of cracking observed indicates that by controlling the orientation of the solidification structure, intraspangular cracking may be avoided. To reduce the interspangular cracking, the cleanliness of the solidifying zinc would be important to reduce alloy segregation at spangle boundaries and thus limit crack nucleation sites.

The density of cracking at the die radius varied with location around the cup indicating that texture in the sheet and/or coating led to preferential zones of cracking. The highest densities of cracks were observed at locations either parallel or perpendicular to the rolling direction. The tensile strain is greatest at these locations and results in the formation of ears. Accommodation of this greater tensile strain results in a higher density of cracking.

4.2.3 Changes in Surface Morphologies of Zinc-Iron Alloy Coatings.

The deformation characteristics of two zinc-iron alloy coatings were investigated during cup drawing. The two alloy coatings, I60N40N and R40A40A, were deposited with two different methods. The first coating, a galvannealed coating, utilizes diffusional bonding similar to hot dip coatings to adhere zinc to the substrate followed by heat treatments that allow the iron to diffuse into the zinc creating the intermetallic alloy coating. The second coating is an electrodeposited alloy coating. Both coatings exhibited higher microhardnesses than the substrate (Figures 22 and 23) and have been reported to have brittle deformation characteristics [30].

The surface morphologies of the as received coatings are distinctly different. Figure 34 shows the surface

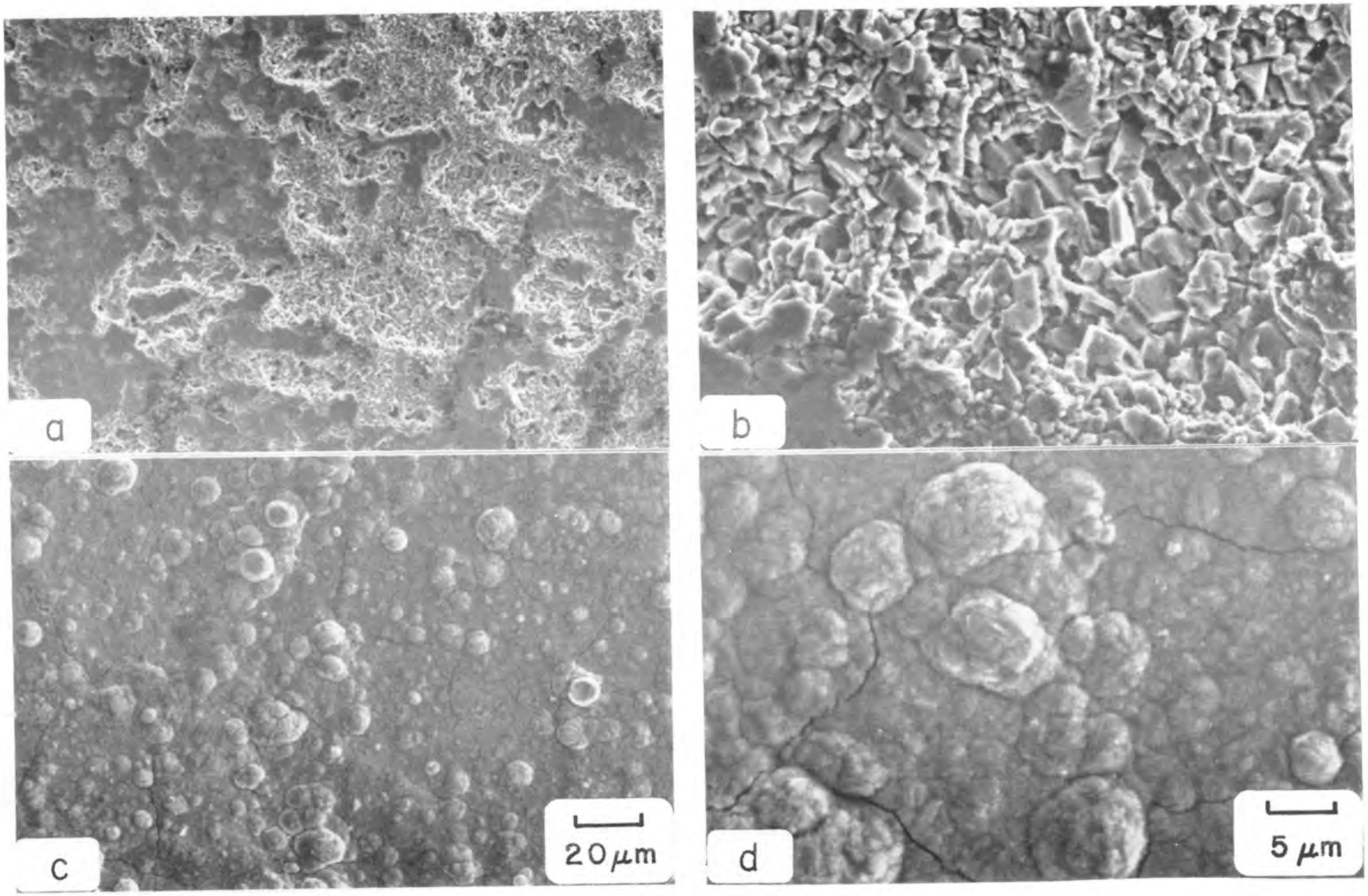

Figure 34 The surface morphologies of as-received galvannealed coating a) and b) and electrodeposited zinc-iron alloy coating c) and d) at two magnifications (SEM micrographs).

morphologies of the two coatings at two magnifications, where, Figures 34a and 34b represent the galvannealed coating (I60N40N) and Figures 34c and 34d represent the electrodeposited coating (R40A40A). The galvannealed coated sheet steel was temper rolled as evidenced by the flattened asperities apparent in Figure 34a. The surface morphology of the galvannealed coating (Figure 34b) resembles a randomly oriented structure with individual growth cells. The surface morphology of the electrodeposited alloy coating (Figures 34c and 34d) resembles a globular morphology similar to that found from sputter deposition. The electrodeposited coating exhibited numerous microcracks in the as-received state. The cracks either nucleated during the deposition process as the sheet was bent over the rollers between electrolytic cells or during final coiling.

The galvannealed coating, I60N40N, exhibited brittle characteristics during drawing. This is in direct contrast to the relatively ductile behavior of the electrogalvanized and hot dip coatings discussed previously. Visual inspection of the fully drawn cups and cleaning of the tooling revealed that some of the coating had been removed during deformation. The amount of coating removed appeared to be significantly more than observed with the electrogalvanized and hot dip coatings.

Figure 35 shows micrographs at different locations on partially drawn and fully drawn galvannealed sheets with the resulting deformation characteristics of the coating. The drawing direction is horizontal and to the left. As deformation initiates in the flange, the coating cannot accommodate the strain and subsequently cracks. The coating, unable to accommodate compressive strains simply by cracking, starts to delaminate from the substrate in the hoop direction (Figure 35a). The coating in Figure 34a has not completely separated from the substrate indicating that a critical stress needed to completely break the bond between the substrate and the coating has not yet been obtained. When a cup is fully drawn, the amount of coating loss increases with depth of draw.

The increase in coating loss with depth of draw is represented in Figures 35b and 35c located at the one-quarter and three-quarter heights respectively. The increase in coating loss can be attributed to increases in deformation and to slight ironing that occurred at the end of the drawing. Cracking of the coating perpendicular to the drawing direction accommodates the tensile strains, and partial removal of the coating allows the accommodation of the compressive strains by relieving the compressive

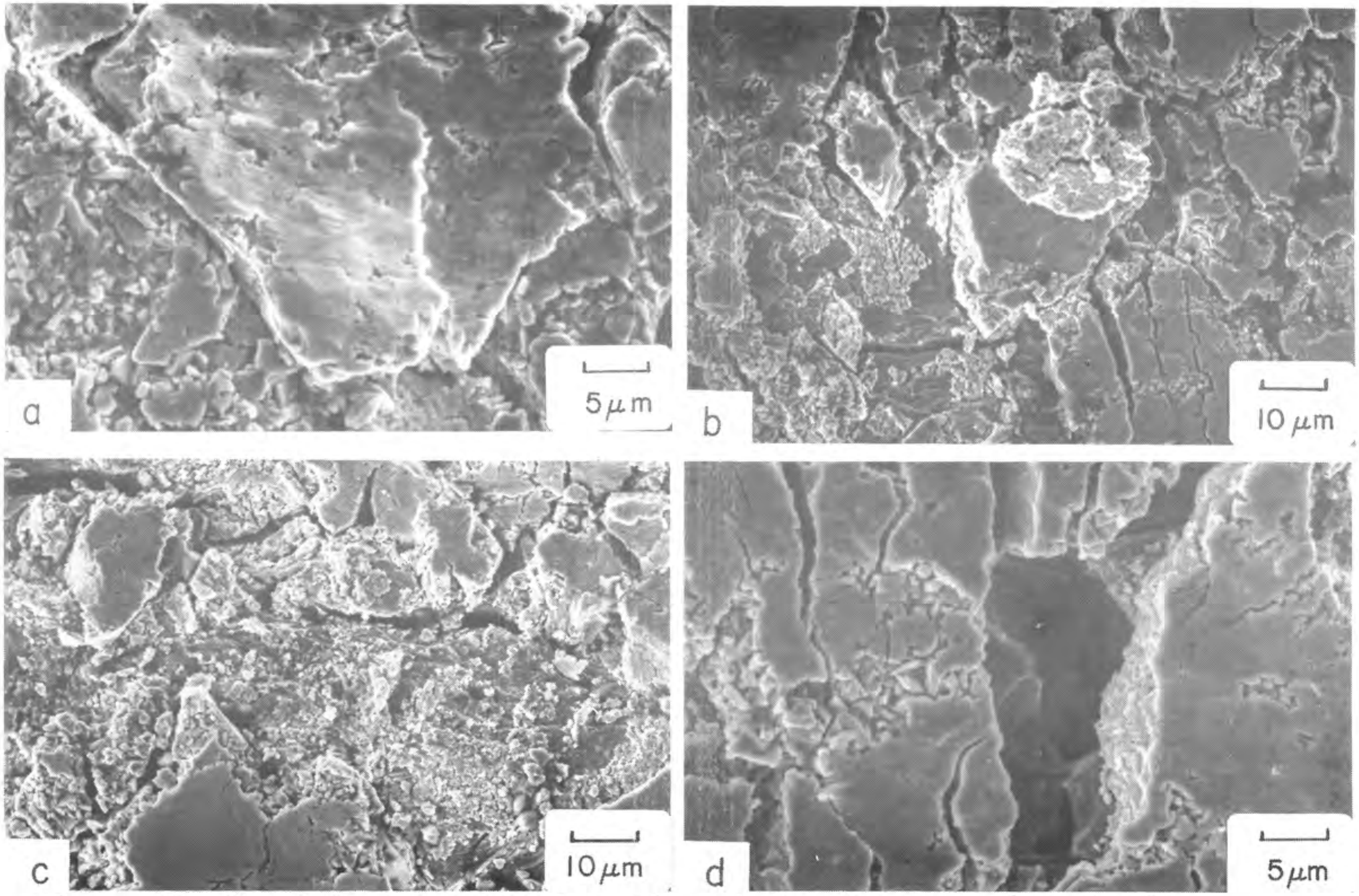

Figure 35 The deformed I60N40N coating at the flange region a) of a partially drawn cup and outside cup wall b), c) and d) of fully drawn cups (SEM micrograph).

stresses acting on the coating parallel to the sheet surface.

Although the coating peels off, part of the intermetallic layer remains attached to the substrate and is visible in Figures 35b and 35c. The presence of a thin intermetallic layer remaining on the substrate, indicates that good bonding has been achieved and the primary reason for coating loss is due to accommodation of compressive strains and stresses. Other authors have also observed that compressive strains enhance removal of galvannealed coatings [21,23]. Aoki et al. [15] stated that a change in strain path has a greater influence on the separation of the coating from the substrate than does a single strain state. Observations during this investigation support separation of the coating from the substrate being greater after a change in strain state (fully drawn cups), compared to a single strain state (the flange of partially drawn cups).

Investigations [46,47] on galvannealed coatings have shown that the γ phase is responsible for the loss of coating during deformation. However, an investigation by Nakmori and Shibuya [48], on the effects of galvannealing conditions and coating weight with respect to coating loss, concluded that the presence of the γ

phase is not the essential cause of coating loss. They attributed the high iron content δ_1 phase (12-14% Fe) with higher loss of coating.

A second observation made while investigating the drawn galvannealed sheet steel is that not only did the coating crack, but the substrate developed surface cracks beneath the coating. Figure 35d shows a micrograph of the cracked coating with a large crack in the substrate. Substrate cracks can also be observed in Figures 35b and 35c. As no consistent orientations of the substrate cracks were observed, the development of a correlation between the strain state and the cracking was not possible. Examination of cross sections of fully drawn cups, both transverse (Figures 36a and 36b) and parallel (Figure 36c) to the drawing direction, revealed surface cracks in the substrate. The micrographs shown in Figure 36 were generated using backscattered electrons on the SEM. Backscattered electrons provide atomic number contrast and since zinc has a higher atomic number than iron, the coating can be distinguished from the substrate. Figure 36a shows a crack in the substrate that appears to propagate from the cracked coating. However, the larger crack in the substrate in Figure 36b does not propagate from a crack in the coating. This corresponds to the

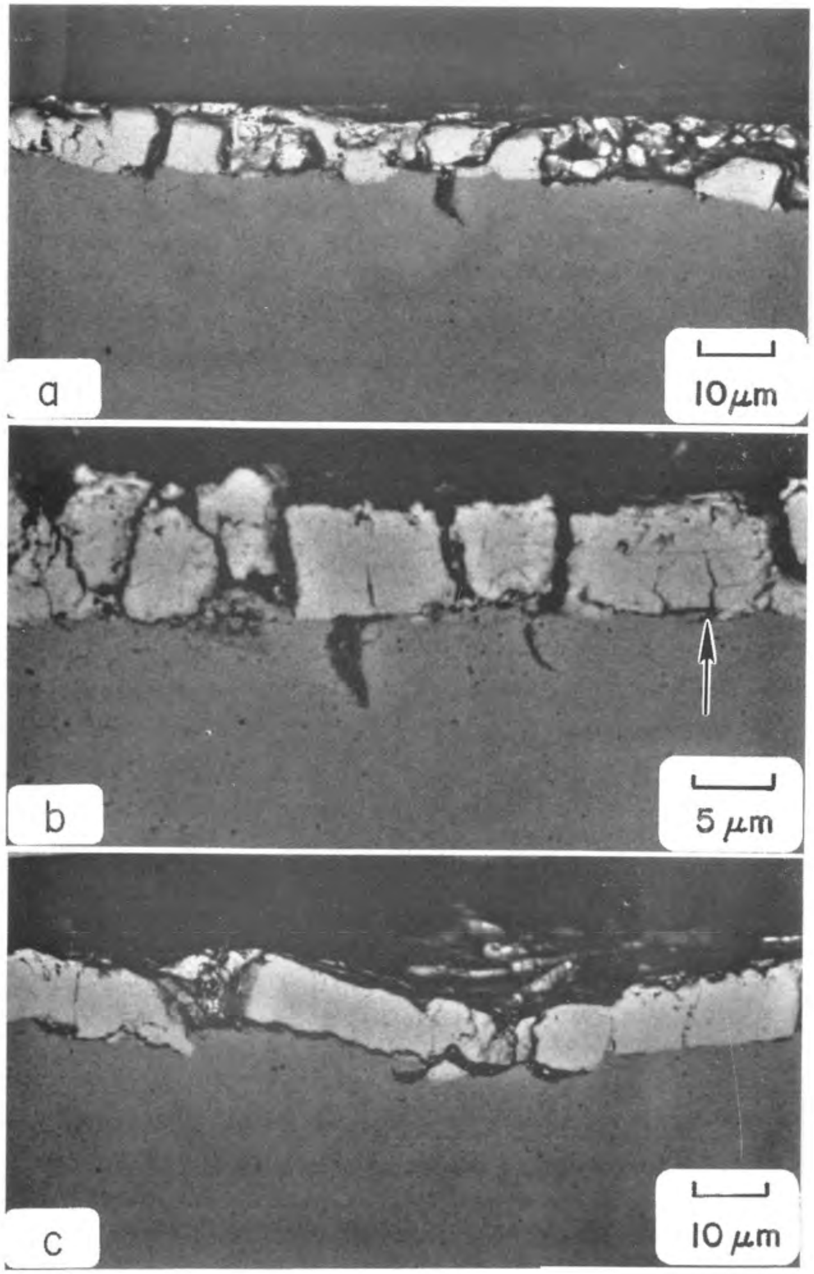

Figure 36 Cross sections through deformed I60N40N coatings. Micrographs a) and b) are parallel to the drawing direction, while micrograph c) is transverse to the drawing direction (SEM backscatter micrographs on as polished samples).

random nature of the substrate cracks observed in Figure 35. Figure 36c shows another substrate crack that does not appear to be nucleated from the coating. The arrow in Figure 36b points to cracks in the coating that appear to nucleate at the substrate/coating interface and propagate towards the free surface of the coating. This suggests that the cracks in the coating are generated at the substrate/coating interface but does not explain how the substrate cracks are developed.

The surface morphology of the deformed substrate was examined after the coating was removed by submersing the samples in 5% HCl for 20 minutes and the resulting series of SEM micrographs are shown in Figure 37. In Figure 37, micrographs a,b,c and d respectively represent one-quarter, one-half, three-quarters and fully drawn heights along the cup wall. The progression of micrographs appear to show a structure similar to elongating ferrite grains with increasing draw. Polishing and etching the substrate of adjacent regions to those shown in Figure 37 revealed similar ferrite grain boundary structures.

To determine if the structure observed in Figure 37 was an artifact of the solution used to remove the coating, undeformed I60N40N and drawn I70G70G and S60HD coatings were removed using the 5% HCl solution. The resulting

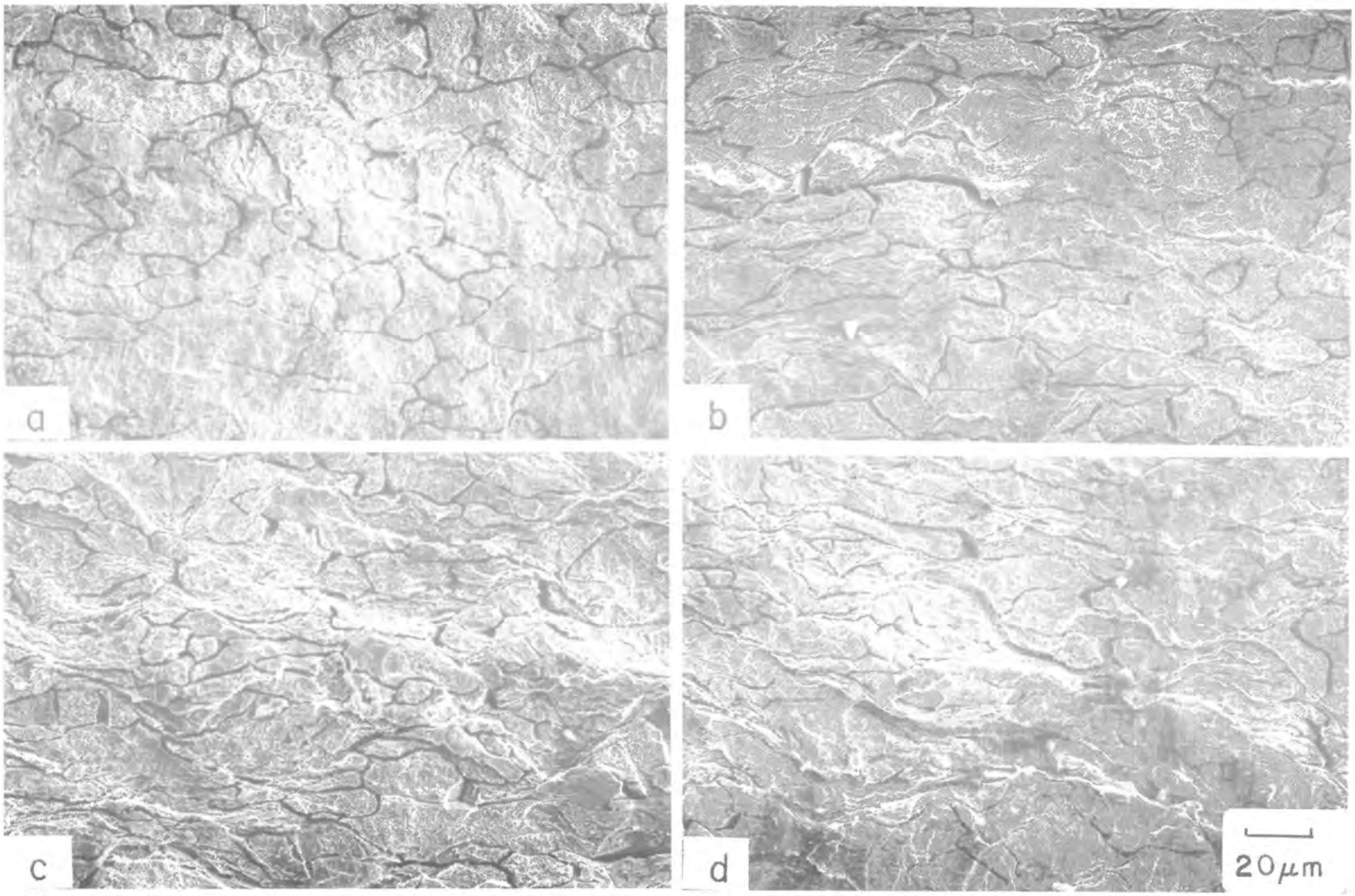

Figure 37 Surface morphology of I60N40N substrate after removal of the coating. Micrographs a-d are a sequential set of surface morphologies progressing up the outside cup wall (SEM micrographs, 5% HCl used to remove the coating).

substrate surface morphologies are shown in Figure 38 along with the substrate of deformed I60N40N. The undeformed I60N40N substrate (Figure 38a) did not exhibit the structure observed with the deformed sample (Figure 38c). Thus, the chemical removal of the coating is not believed to be responsible for resulting cracked structure. The deformed electrogalvanized (Figure 38b) and hot dip (Figure 38c) substrates did not show any indication of substantial cracking, although a few microcracks were observed. The substrate cracking observed in the galvannealed coated sheet steel is believed to be a consequence of the galvannealing process.

Gupta et al. [24] also observed cracking in the substrate along ferrite grain boundaries of galvannealed sheet steels in a iron-zinc alloy layer growth study. He stated that microcracks in the coating caused propagation of cracks into the substrate at ferrite grain boundaries with increasing strain. In Gupta's study, galvannealed sheet steels annealed for eight hours at temperatures of 399°C (750°F) and 454°C (850°F) develop cracks in the substrate at 17% tensile strain. Gupta used diffusion coefficients determined by Onishi et al. [48] to show that substantial diffusion of zinc can occur in iron, especially at grain boundaries. Allegra et al. [49] showed

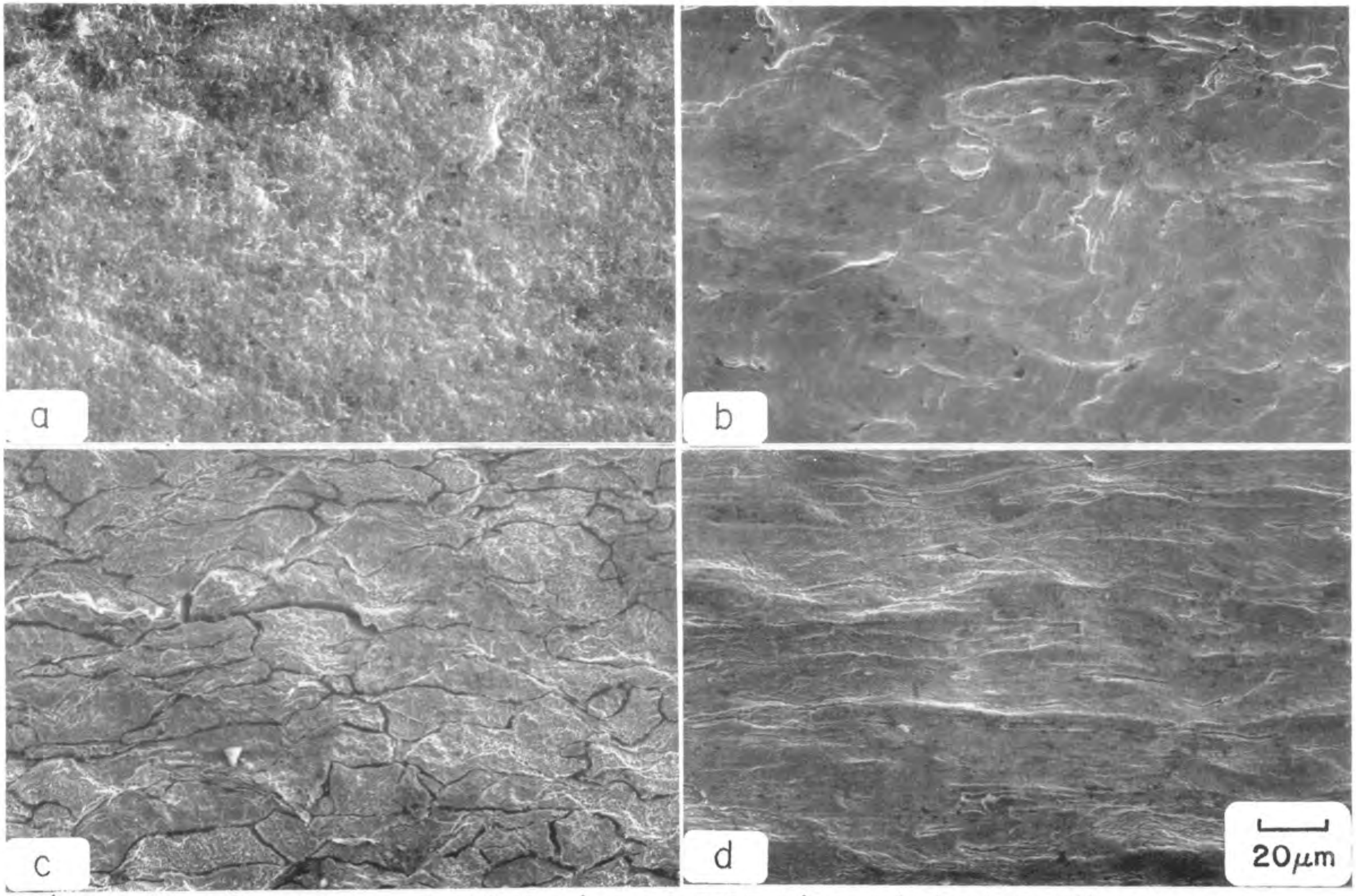

Figure 38 The surface morphologies of selective substrates after removal of the coating: undeformed I60N40N (a) and deformed I70G70G (b), I60N40N (c) and S60HD (d). The deformed samples were from the outside surface of fully drawn cups (SEM micrographs).

similar results of zinc diffusion at grain boundaries in a study on 55% Al-Zn alloy coating resulting in ferrite grain boundary cracking upon deformation.

Gupta and Allegra determined processing parameters that would prevent the substrate cracks from developing during deformation. Allegra stated that the presence of at least 0.004% phosphorus would prevent diffusion of zinc at the ferrite grain boundaries. The diffusion of phosphorus to the grain boundaries prevented grain boundary embrittlement by zinc. Gupta showed that galvannealing temperatures below 343°C (650°F) did not result in grain boundary embrittlement. Higher galvannealing temperatures resulted in grain boundary embrittlement.

The chemical composition of the substrate may influence the diffusion of zinc to the ferrite grain boundaries as was indicated by Allegra. The I60N40N substrate was an interstitial-free steel. Since only one galvanneal sheet steel was investigated, it was not determined what consequence this type of substrate would have with regard to the substrate cracking observed.

The second zinc-iron alloy coating investigated was the electrodeposited coating R40A40A. Electroplated alloys can range from 100% zinc to 100% iron. Many authors have investigated the coating performance of coatings which span the entire range of iron contents and have concluded that a coating with 15-20 % iron has the best desired properties [27]. The nominal iron content of the R40A40A was 15 %, determined by EDS on the SEM. The nominal surface iron content of the galvannealed coating was also determined to be 15 %.

The R40A40A coating exhibited numerous microcracks in the as-received condition (Figure 34d). The effect of strain during drawing on microcracking in the coating is shown in the series of SEM micrographs in Figure 39. These micrographs were taken at several different locations on a partially drawn and fully drawn cup. Figure 39a shows severe large cracking and loss of the coating occurring in the flange of a partially drawn cup. The drawing direction is horizontal and to the left for all of the micrographs in Figure 39. The exposed substrate in Figure 39a is relatively smooth and free of a thin bonding layer. The lack of evidence of bonding suggests that the bond strength is less than that of the galvannealed coating. Strong evidence that a change in strain path is detrimental to the zinc-iron alloy coating adherence is demonstrated in Figure 38b. This micrograph is taken at the mid-radius of the bottom die on the outside of a partially drawn cup. The stress/strain state changes from tensile to compressive

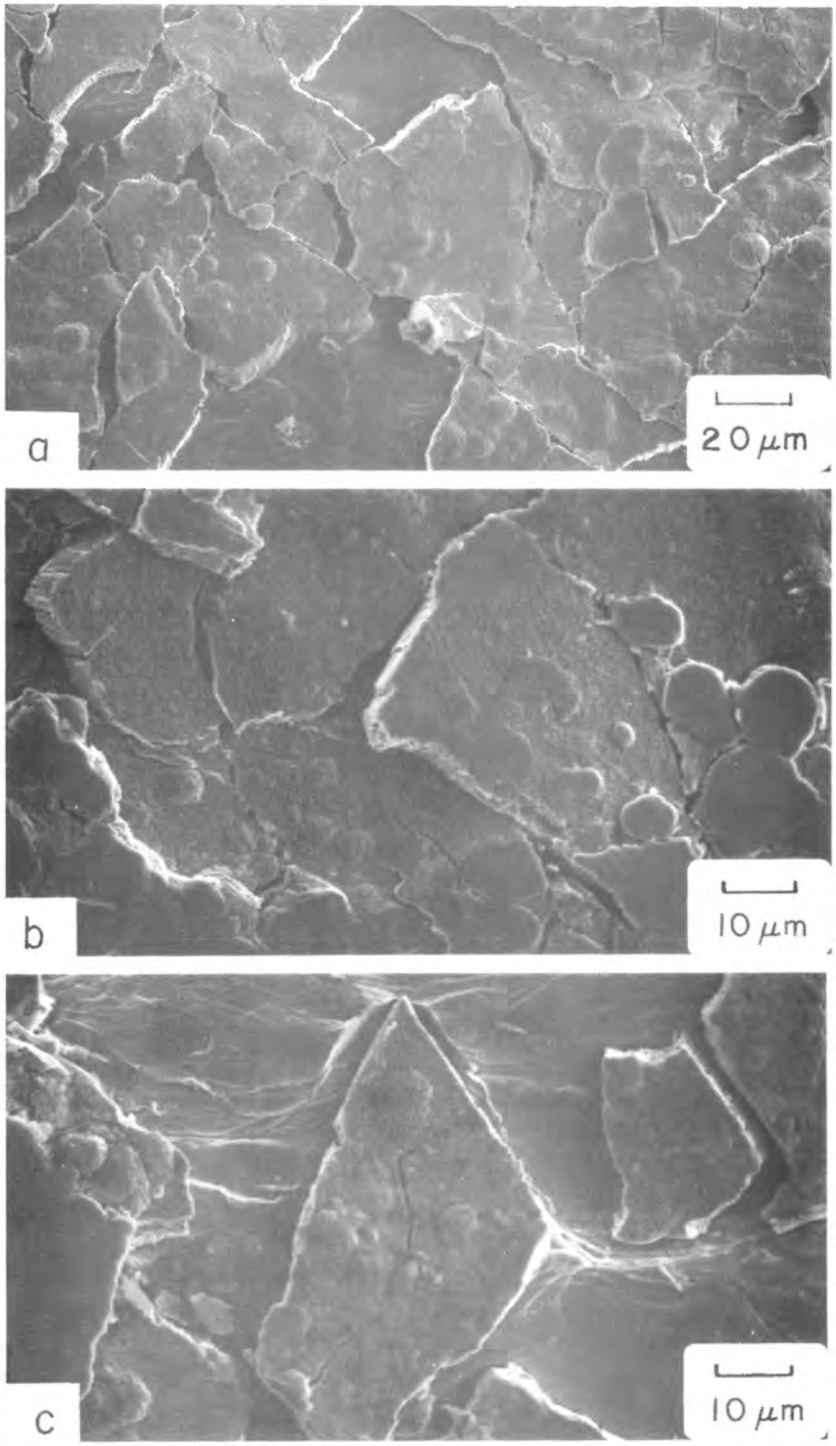

Figure 39 The deformed coating of R40A40A in the flange region (a), inside die radius (b), and outside cup wall (c) (SEM micrographs).

parallel to the drawing direction as the sheet deforms over the radius (see Figure 18c). This change in stress/strain state is reflected by the 20μm piece of coating (the large section in the center of Figure 39b) starting to flake away. Figure 39b shows the typical morphology found at the die radius.

Figure 39c presents a micrograph taken on a fully drawn cup at the three-quarter cup height. Significantly more coating loss has occurred with depth of draw. Individual islands of the coating are left attached to the substrate. Once again the substrate appears to be relatively clean and free from any evidence of a bonding interface. The substrate appears to flow around the large coating island in Figure 39c, indicating that the substrate is much more ductile than the alloy coating. The microhardness of the coating shown in Figure 23 was significantly higher than that determined for the substrate (Figure 22). The higher microhardness of the coating indicates that the substrate would deform at a lower stress than the coating. The stress required to plastically deform the coating may not be achieved if the substrate will deform first and relieve the applied stress acting on the coating.

The two alloy coatings were examined by cross sectioning with a special cryogenic fracture technique

[50]. The resulting morphologies found on fully drawn cups sectioned at mid-cup wall height, perpendicular to the drawing direction are shown in Figure 40. The substrate of the galvannealed product in Figure 40a was fairly flat and uniform. Although a few cracks are apparent near the interface between the substrate and coating, the bonding characteristics appear to be better than that of the electrodeposited coating in Figure 40b. The interface between the coating and substrate in Figure 40b was clearly defined, and in some cases, completely separated for the electrodeposited alloy coating. The deformed substrate was also rougher than that of the galvannealed sheet. The rougher surface may be a consequence of differences in sheet thickness, or a result of different hold down pressure requirements for different sheets during drawing. This rough surface probably contributed to a greater loss of coating than was observed in the galvannealed coating.

The mechanism of coating loss for the two alloy coatings during the cup drawing tests would be considered flaking per the definitions stated in section 1.3. Other investigators [29,31,48] have determined that galvannealed and electrodeposited zinc-iron alloys are susceptible to powdering. These authors either have differences in the definitions of powdering and flaking from those given in

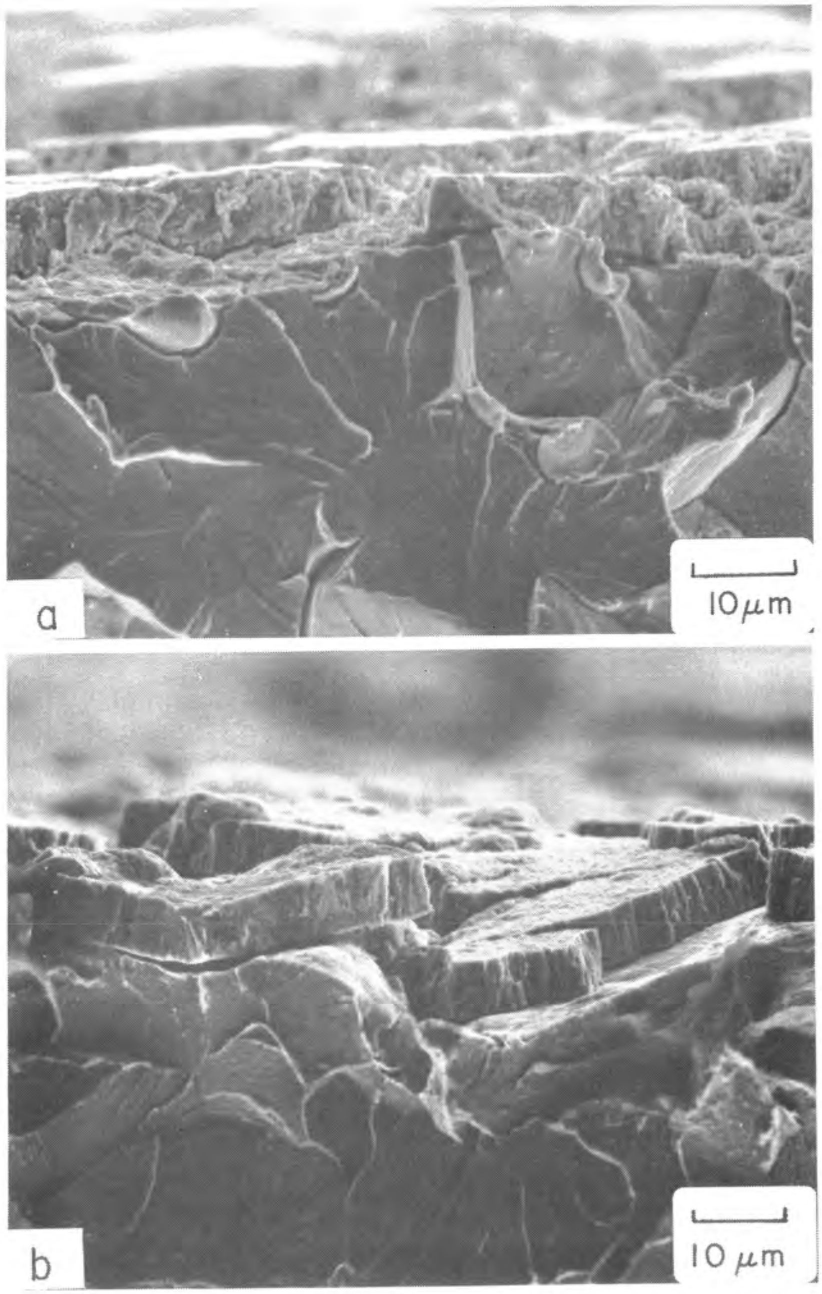

Figure 40 Cup wall cross sections of fully drawn cups for a) I60N40N and b) R40A40A revealed by the cryogenic fracture technique (SEM micrographs).

section 1.3, or no specific definition of powdering was given with their results. Clearly, from the micrographs presented earlier, the major cause of coating failure is due to the decohesion of the coating/substrate interface for the alloy coatings investigated. By definition, this type of coating failure is classified as flaking.

The deformation characteristics of the six coated sheet steels investigated have been evaluated. The next section will discuss the effects of inclusions found in the deformed electrogalvanized coatings.

4.2.4 Effect of Inclusions in the Electrogalvanized Coatings.

It has been shown that inclusions will cause damage to coatings during deformation [45]. Several inclusions were found in each of the electrogalvanized coatings. Figure 41 shows the inclusions found in each electrogalvanized coatings for fully drawn specimens. The narrow arrows in Figure 41 point to the inclusions. The drawing direction is horizontal and towards the left in each of the micrographs. Figure 41a shows an aluminum silicate inclusion found in the S70G70G sheet. Figure 41b shows an aluminum-rich inclusion found in the I70G70G sheet. Figure 41c shows an aluminum-rich inclusion found in the R60G60G sheet. Inclusion determination was conducted by EDS.

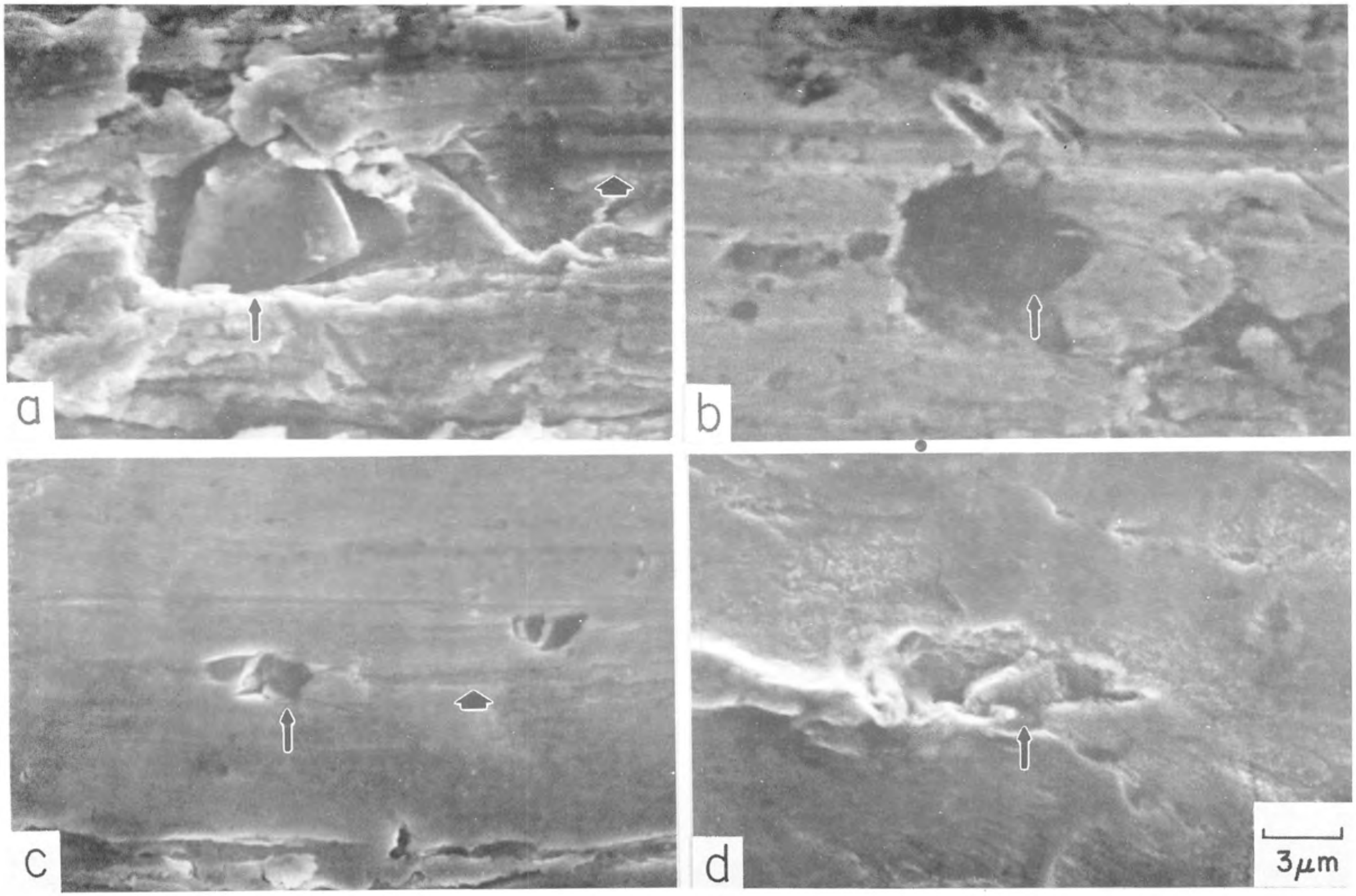

Figure 41 Inclusions in deformed coatings of a) S70G70G, b) I70G70G, c) R60G60G and in the substrate of I70G70G revealed after removal of the coating (SEM micrographs).

The large arrows in Figures 41a and 41c show ploughing left behind as the zinc fragment was removed. Figure 41c also shows a secondary zinc fragment which is partially removed just to the right of the inclusion. The ploughing of the inclusions through the coating can lead to damage similar to that indicative of galling.

If the inclusions are surface inclusions in the substrate, removal of the coating should reveal the inclusions. The coating of an I70G70G fully drawn sample was remove by using a 5% HCl solution for 15 minutes. Figure 41d shows an aluminum inclusion found in the substrate after the zinc coating was removed. This suggests that the inclusions could have evolved from the substrate. To further investigate the migration of inclusions out of the substrate, the coating of an undeformed I70G70G sheet was stripped and subsequently drawn into a cup. Aluminum rich inclusions were observed on the deformed surface and in some areas started to plough through the steel surface similar to that observed in Figure 41c. This supports that the inclusions have evolved from the substrate.

The location of the inclusions found in the cup wall of the coated sheet are of significance. A qualitative investigation on the distribution of inclusions as function of the position along the cup wall was performed. Starting at the punch region of the cup and moving up along the inside cup wall, the inclusions were not observed until the mid-height of the cup. From the mid-height to the top of the cup (the original outermost fibers of the circular disk) the density of the inclusions penetrating the coating increased. The location and variation on inclusion density with position indicates that a critical compressive strain is required for the inclusions to punch through the surface of the coating.

4.3 Models Depicting Coating Deformation.

Models depicting the deformation characteristics of the coatings examined in Section 4.2 are presented and discussed. The models were formulated from observations of the coating deformation behavior in conjunction with a consideration of the coating strength.

A model is proposed to describe the deformation behavior of the S70G70G and I70G70G coatings within the flange of the deep drawn cup. The model was developed to describe the failure processes illustrated in Figures 27a, 27b, and 27d. In the model, the substrate is assumed to deform isotropically. Within the flange uniform thickening develops in the substrate as a result of the induced compressive hoop stresses.

In the model, shown schematically in Figure 42, the zinc is assumed to deform anisotropically. Zinc crystals with slip systems preferentially orientated to thicken, locally deform which results in a nonuniform thickness in the coating. This deformation path is represented in stage I of Figure 42. As the thickness increases with depth of draw, the top of the zinc hill contacts the top platen and is constrained from further thickening. The zinc coating, which is more ductile than the substrate, flattens as illustrated in stage II of Figure 42. Contact with the top platen induces a local shear stress in the flattened portion of the coating. As a consequence of the friction generated by coating contact with the top platen, radial flow is limited and the zinc deforms to develop the overlapped morphology depicted in stage II of Figure 42. If the deformed coating can be viewed as an "I" beam, as the flange grows in width, the frictional shear stress on the flange increases in magnitude as shown in the second part of stage II. As the flange grows in width, the transferred frictional shear stress in the web reaches a critical value and failure (powdering) occurs as depicted in stage III of Figure 42.

The stages illustrated in Figure 42 were directly

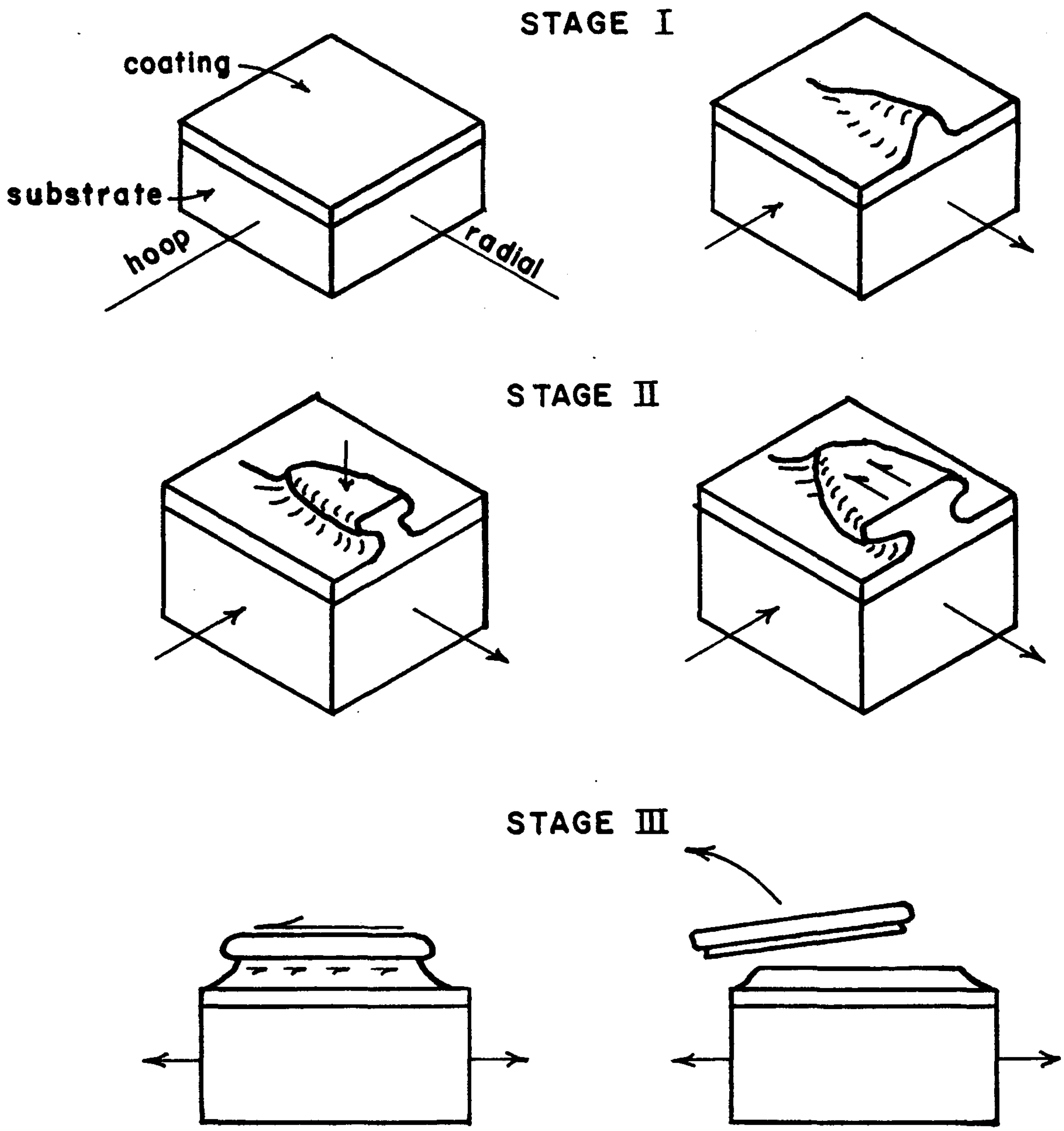

Figure 42 Schematic representation of a three stage model depicting coating removal during drawing of a sheet material with a ductile coating.

observed in Figures 27a, 27c, and 27d. In Figure 27a, the raised morphology of the coating which contacted the top platen was verified with SEM stereographic pairs and shown to be similar to the initially flattened structure shown in Stage II of Figure 42. The arrow in Figure 27c points to a overlapped region represented by the flange region in stage II of Figure 42. Figure 27d is representative of the failure shown in stage III of Figure 42.

The model depicted in Figure 42 describes the deformation behavior of ductile coatings. The next model will depict the deformation behavior of hard brittle coatings.

The microhardness evaluation (Figure 23) showed that the zinc-iron alloy coatings have a higher hardness than their substrates. The cracking of the coating during hardness testing and observations made during drawing suggest that the coating is brittle and will crack at a given stress or strain. The substrate, however, is ductile and will easily deform. The substrate is assumed to deform isotropically. As the substrate deforms, the coating tries to match the deformation to maintain integrity at the bonding interface. At a critical strain, the coating cannot maintain the bonding structure and either cracks or separates from the substrate to accommodate the deformation. The cracks initiate at the interface and propagate towards the surface due to the high stress concentration generated at the interface. A model depicting how delamination of the alloy coating from the substrate could occur, is shown in Figure 43. Stage I shows how the compressive stresses initiate delamination when the coating cannot match the deformation of the substrate. The initiation of the delamination of the coating from the substrate for the galvanneal coating is shown in Figure 35a. Stage II is a continuation of delamination due to the compressive strain. Stage III shows the coating flaking off and thus relieving stresses on the adjacent coating. The exposed substrate resulting from the delamination of the coating is shown in Figures 35c and 39a. Figures 35c and 39a also show the islands of coatings that remain attached to the substrate.

A model which illustrates the importance of tensile stresses on coating cracking is presented in Figure 44. The coatings in this model may either be brittle as with the zinc-iron alloy coatings or have crystal orientations that do not promote slip as suggested for the R60G60G coating. Stage I in Figure 44 shows the stresses which develop in the coating to accommodate applied tensile strains in the substrate. The tensile deformation of the

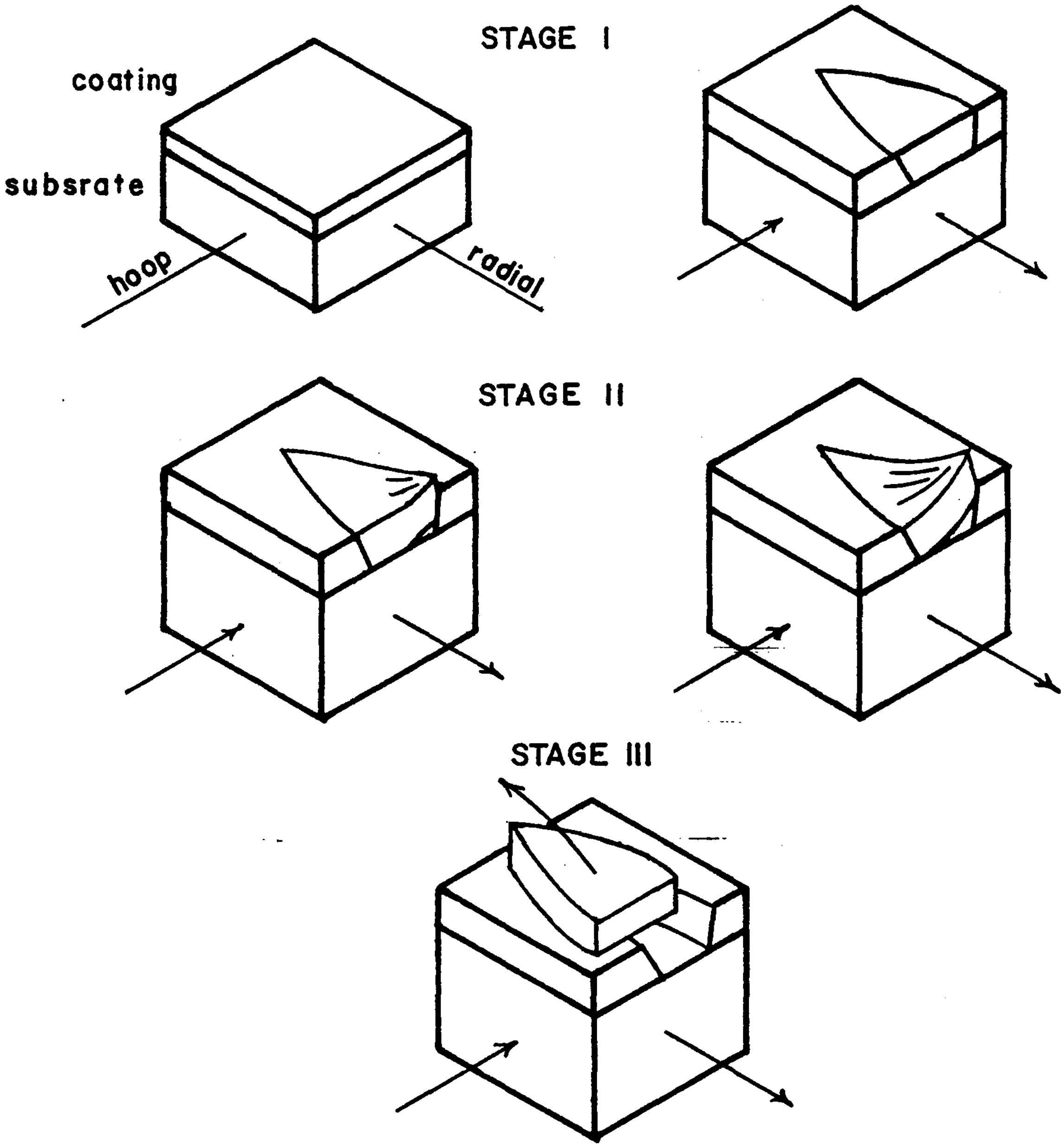

Figure 43 Schematic representation of a three stage model depicting coating removal during drawing of a sheet material with a brittle coating.

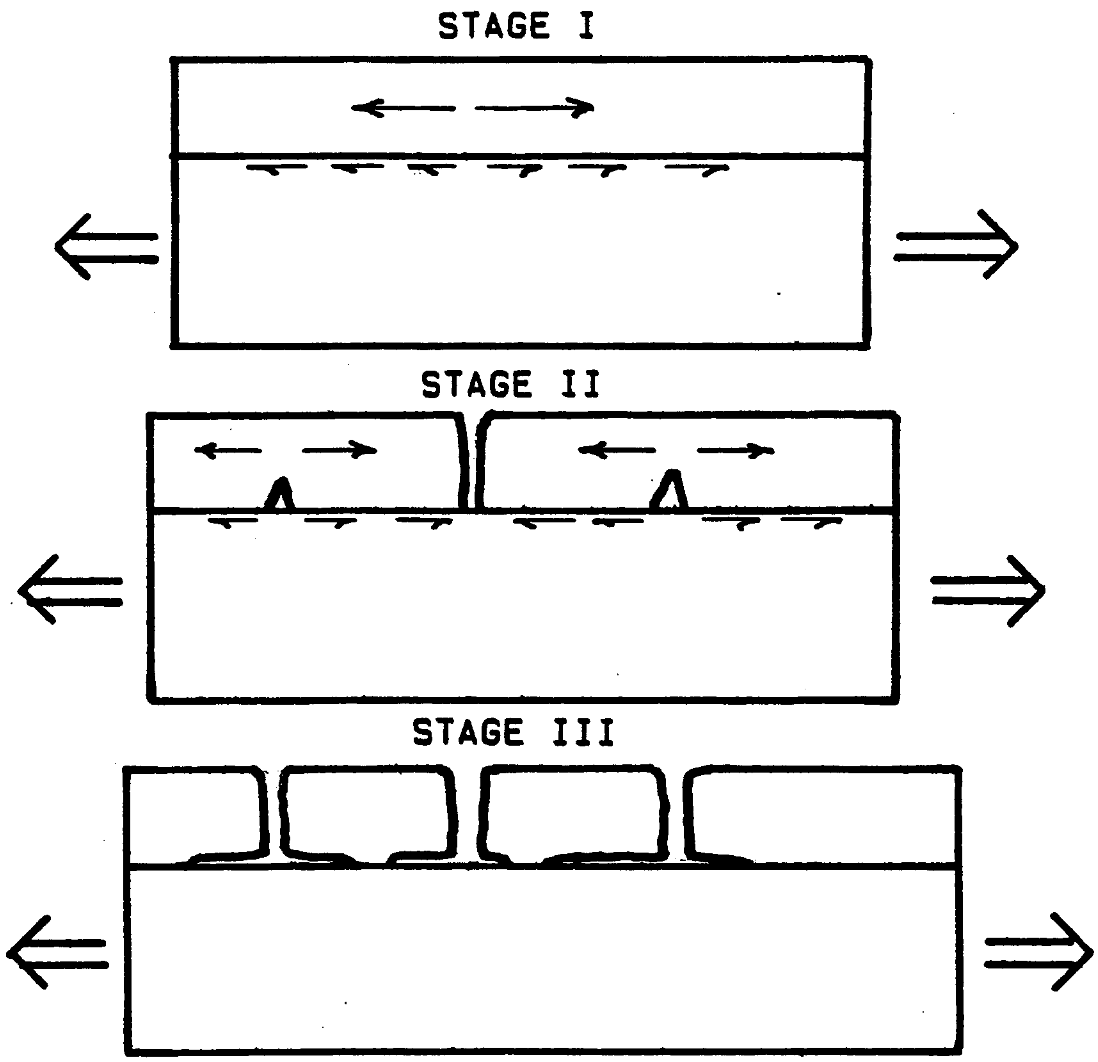

Figure 44 Schematic representation of a three stage model depicting coating cracking resulting from tensile strains.

substrate transfers a tensile stress to the coating through shear stresses at the coating/substrate interface. A stress concentration occurs at the coating/substrate interface due to the localized shear stresses. When a critical stress state is obtained at the interface, the coating cracks, and the cracks propagate toward the free surface. This process is depicted in stage II of Figure 44. Observations of cross sections through the deformed galvannealed sheet (Figure 36b) support crack initiation at the coating/substrate interface. Once the crack has propagated through the coating, the tensile stress in the coating on either side of the crack is relieved. This process continues throughout the coating and the tensile stresses in the coating are relieved.

Since the tensile stresses in the coating have been relieved by cracking, the coating acts as an elastic body and provides enough rigidity to withstand the applied shear stresses at the coating/substrate interface. As tensile deformation continues the applied shear stresses at the interface reach a critical value and cause separation between the coating and substrate. As the coating separates from the substrate the shear stresses are relieved and the separation of the coating stops. This process continues until a small region of the coating remains attached to the substrate. The small region of the coating that remains attached to the substrate is not influenced by the shear stresses and will not completely separate from the substrate. The small region of the coating that remains attached to the substrate prevents flaking. This process is shown in stage III of Figure 44. The observations made on cross sections of deformed galvannealed sheet steel (Figure 36) provide evidence that only small regions of the coating remain attached to the substrate. The micrographs in Figure 36 shows cracking between the substrate and coating, however, small regions of the coating appear to remain bonded to the substrate.

The relative bond strengths between the alloy coatings and the substrate appear to have a consequence on the spacing between cracks. The density of cracks observed in the deformed galvannealed coating appeared to be greater than that observed in the electrodeposited alloy coating. When the galvannealed coating flaked, a thin layer of the coating remained attached to the substrate in some areas (see Figure 35b and 35c). When the electrodeposited alloy coating flaked, there was no evidence of a thin layer of the coating that remained attached to the substrate (see Figure 39a). The galvannealed coating appeared to have a superior bond strength to that observed for the electrodeposited alloy coating. The microhardness of the two coatings were similar, which indicated that the strengths of the two coatings are equivalent.

If the bond strength of the galvannealed coating is stronger that the bond strength of the electrodeposited alloy coating, then the interfacial shear stresses that can be transferred to the galvannealed coating would be greater than the shear stresses transferred the the electrodeposited coating. This would result in a higher density of cracks in the galvannealed coating than in the electrodeposited coating due to the ability of the bond strength to transfer stresses. Figures 35b and 35d show the relatively close spaced cracks in the deformed galvannealed coating. Figure 39 shows an increase in spacing between the cracks in the electrodeposited alloy coating. The inferior bond strength of the electrodeposited coating results in cracking along the coating/substrate interface with larger spacing between the cracks in the coating.

To visualize how substrate inclusions damage the electrogalvanized coatings, a model which depicts the migration of inclusions through the coating is represented in Figure 45. This model depicts the observations shown in Figure 41. The surface inclusion is less ductile than the

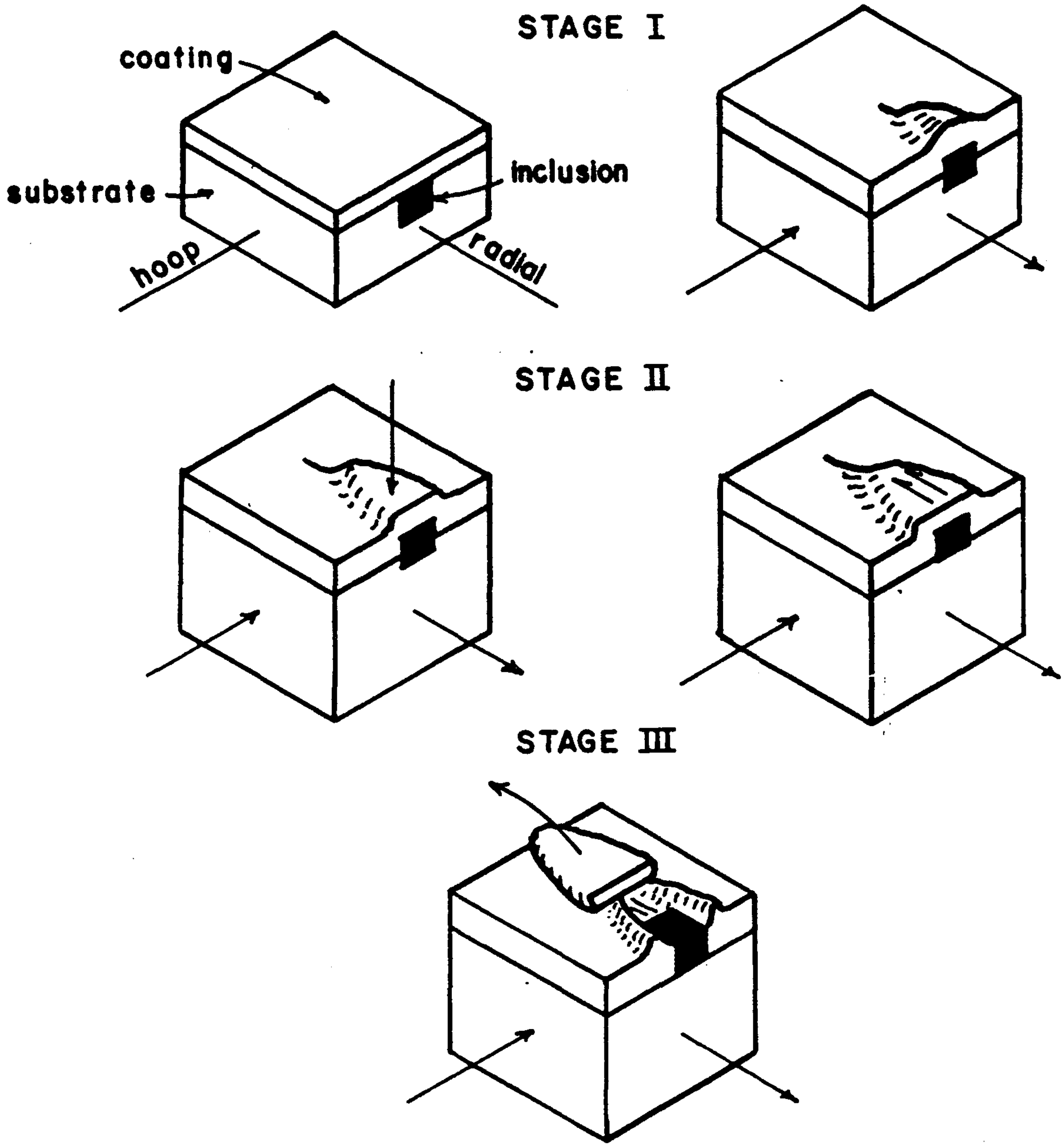

Figure 45 Schematic representation of a three stage model depicting migration of substrate surface inclusions up through the coating.

surrounding substrate and does not deform plastically when the drawing operation begins. The substrate will flow around the inclusion pushing it upward as depicted in stage I of Figure 45. The zinc coating, more ductile than the substrate, is also pushed up by the inclusion. As the inclusion migrates upward with an increased hoop compressive strain, the coating flattens when it contacts the top platen which is shown in stage II of Figure 45. As drawing continues, a frictional shear stress is applied to the coating by sliding contact with the top platen. In stage III of Figure 45, the shear stress on the zinc/inclusion interface reaches a critical value where failure occurs and the coating is removed.

The deformation characteristics of the six coated sheet steels have been presented along with models which depicted the coatings deformation behavior. The next section will summarize the conclusions from the observations presented.

5.0 CONCLUSIONS

The deformation characteristics of pure zinc and zinc-iron alloy coatings were investigated by laboratory deep drawing. The pure zinc coatings consisted of a hot dip and three electrogalvanized products with coating weights between 60 to 70 g/m^2. The alloy coatings investigated were a galvanneal and an electrodeposited zinc-iron product with coating weights between 40 to 60 g/m^2. The response of the coatings to the stress and strain states that exist during cup drawing was used to characterize coating deformation.

Definitions that describe the types of coating damage were developed in this thesis and are listed as follows:

1a. Powdering consists of particle formation by intracoating failure to produce particles with sizes less than the coating thickness. The pure zinc coatings exhibited limited powdering. Some particles of zinc appeared to fail due to cleavage along the basal plane, while other particles appeared to fail as a result of shear instability.

1b. Flaking consists of flat particle formation by decohesion of the coating/substrate interface to produce particles with sizes similar to the coating thickness. Flaking occurs by the zinc-iron alloy coatings which delaminate from the substrate to accommodate compressive stresses during drawing.

1c. <u>Galling</u> results from adhesion of coating particles to the tool surface. The adhered particles plough through the coating or bond to the coating resulting in additional coating damage with subsequent forming operations. Properly lubricated specimens prevented galling during this investigation.

1d. <u>Cracking</u> consists of through thickness fracture of the coating without particle decohesion from the substrate. Cracking is caused by the inability of coatings to plastically deform, and may nucleate at inclusions, low ductility phases or as a result of unfavorable coating texture.

Additional observations of coating deformation characteristics related to accommodation of substrate deformation during cup drawing are summarized as follows:

2a. A FEM analysis that simulated cup drawing as a function of position through the thickness of the sheet characterized of the stress states on both surfaces of the sheet during deformation. This analysis shows significant stress gradients through the sheet thickness, observations which are different from conventional membrane analysis. The FEM analysis accounted for strain hardening and thickening of the sheet during drawing which are ignored by slab equilibrium analysis.

2b. The deformation behavior of the pure zinc coatings are texture dependent. One electrogalvanized coating had an unfavorable texture and cracked to accommodate substrate deformation while the other electrogalvanized coatings had favorable textures and accommodated plastic deformation by slip. The deformed microstructure of the hot dip coating indicated that crystal orientations within spangles controlled the deformation characteristics of the coating. The hot dip coating exhibited intraspangular cracking in frosty regions with crystal orientations unfavorable for slip. Shinny spangles developed interspangular cracking to accommodate the substrate deformation.

2c. The zinc-iron alloy coatings cracked to accommodate tensile stresses and flaked to accommodate compressive stresses. The relatively higher strengths and lower ductility of these coatings compared to the substrate resulted in cracking along the coating/substrate interface in response to compressive stresses. Through-thickness cracks in the galvanneal coating nucleate at the coating/substrate interface and propagate towards the coating surface.

2d. Diffusion of zinc to ferrite grain boundaries resulted in the development surface cracks in the galvanneal substrate during deformation.

REFERENCES

1. "The Forming of Galvanized Sheet Steels", Guidelines for Automotive Applications, American Iron and SteelInstitute, AISI No. SG539 0286-10M-RI.

2. Opbroek J.B., and W.G. Granzow, "A Deep Drawing, Hot-Dipped Galvanized Steel For Difficult Forming Applications", S.A.E. Technical Paper No.850275, 1985.

3. Otterberg R., "Volvo Laboratory Study of Zinc-Coated Steel Sheet - Formability Properties", S.A.E. Technical Paper No.890702, 1989.

4. Meuleman D.J., S.G. Denner and F.L. Cheng, "The Effect of Zinc Coatings on the Formability of Automotive Sheet Steels", S.A.E. Technical Paper No. 840370, 1984.

5. American Heritage Dictionary, Second College Edition, Houghton Mifflin Company, Boston, 1985.

6. Dieter G.E., Mechanical Metallurgy, 3rd Edition, McGraw-Hill, New York, pp 671-678.

7. Taylor B., "Sheet Formability Testing", Metals

Handbook, Vol. 8, 1985, pp 547-570.

8. Leslie W., The Physical Metallurgy of Steels, McGraw-Hill, New York, 1981, pp 150-155.

9. Blickwede D.J., "The New Look of Sheet Steels", Manuscript from Yakawa Memorial Lecture at the 107th ISIJ Meeting, 1984.

10. Hosford W.F. and R.M. Caddell, Metal Forming: Mechanics and Metallurgy, Prentice-Hall, New Jersey, pp 274-291.

11. Stevenson R., "Formability of Galvanized Steels-Revisited", S.A.E. Technical Paper No. 850276, 1985.

12. Hanson P.H., N. Bay, P. Christensen, "Analysis of the Ring Compression Test using a General Friction Model and the Upper Bound Elemental Technique", North American Manufacturing Research Conference Proceedings - 16, Urbana, Illinois, May 24-27, 1988, pp 41-47.

13. Rangarajan V., D.K. Matlock, and G. Krauss, "Analysis of Friction on Coated Sheet Steels", Advanced Steel Processing and Products Research Center, Report

No.MT-SRC-089-035, September 1, 1989, pp 61-106.

14. Wilson A.E., "Friction Effects on the Formability of Electrogalvanized and Hot-Dipped Automotive Sheet Steel", Colorado School of Mines Master of Science Thesis No.T-3733, August, 1989.

15. Aoki I., T. Horita, and T. Herai, "Formability and Application of Galvanized Sheet Steels", Technological Impact of Surfaces: Reltionship to Forming, Welding and Painting, Materials/Metalworking Technology Conf. Proc., Metals Park, Ohio, ASM, 1982, p. 165.

16. Vallance D., D.K. Matlock, and C.J. Van Tyne, "Determination of Friction Coefficients of Sheet Metal by the Bending Under Tension Test", Advance Steel Processing and Products Research Center, Report No. MT-SRC-089-035, September 1, 1989, pp 39-60.

17. Bablik H., Galvanizing (Hot-Dip), 3rd Edition, John Wiley and Sons, Inc, New York, 1950, pp137-166.

18. Mackiowak J. and N.R. Short, "Metallurgy of Galvanized Coatings", Int. Met. Revs., Vol. 24, 1979, pp 1-19

19. Cameron D.I., G.J. Harvey, and M.K. Ormay, "The Spangle of Galvanized Iron", The Journal of the Australian Institute of Metals, Vol. 10, No. 3, August 1965, pp. 255-264.

20. Cameron D.I. and G.J. Harvey, "Solidification and Spangle of Galvanized Coatings", 8th International Conference on Hot Dip Galvanizing, London, England, 1967, pp. 86-97.

21. Belleau C. and D.K. Kelley, "Quality, Formability, and Productivity Considerations in Production Use of Galvanized Steels", S.A.E. Technical Paper No. 850272, 1985.

22. Mathieu S. and P. Patou, "Zinc Coating Influence on Spot-Weldability of Hot-Dip Galvanized Steel Sheets", S.A.E. Technical Paper No. 850273, 1985.

23. Belleau C. and D.K. Kelley, "Characterization of One-and-a-half Side Galvanized Steels for Automotive Applications", S.A.E. Technical Paper No. 840284, 1984.

24. Gupta I., R.S. Cline, and R.S. Patil, "Effect of Iron-Zinc Alloy Layer on the Mechanical Properties and Formability of Hot-Dip Galvanized Steels", S.A.E. Technical Paper No. 840284, 1984.

25. Jiricny V., H. Choi, J.W. Evans, "Zinc Electrodeposited Morphology Under Conditions of Fluctuating Current Density", Journal of Applied Electrochemistry, Vol 17, 1987, pp91-103.

26. Kamei K. and Y. Ohmori, "Hetero-epitaxial Growth of Zinc Electrodeposits on Low-Carbon Steel Sheets", Journal of Applied Electrochemistry, Vol 17, 1987 pp821-827.

27. Adaniya T., Y. Hara, M. Sagiyama, T. Homa, and T. Watanabe, "Zinc Iron Alloy Electroplating on Strip Steel", Plating and Surface Finishing, August 1985, pp52-56.

28. Makimatilla S. and A. Ranta-Eskola, "Behavior of Galvanized Coating During Forming", Proc. of the 13th Biennial Congress of the IDDRG, Melbourne, Australia, 1984, pp293-304

29. Ejima M., Y. Tokunga, and T. Honda, "Analysis of Formability and Some Problems in Stamping of Coated Steel Sheets", Proc. of the 13th Biennial Congress of the IDDRG, Melbourne, Australia, 1984, pp317-328.

30. Kojima H., T. Yamamamoto, K. Ito, T. Fujiwara, and T. Kanamara, "Properties of Zn-Fe Alloy Electroplated Steel Sheets", S.A.E. Technical Paper No.840214, 1984.

31. Ike H., "Fundamentals of Galling and Other Surface Damage Caused by Sliding and/or Plastic Deformation", Advanced Technology of Plasticity, Volume I, 1984, pp180-185.

32. Burford D., "Frictional and Geometric Effects in Punch-Stretch Sheet Metal Formability Testing", Ph. D. Thesis No. T-3465, SRC Research Report No. MT-SRC-087-042, Colorado School of Mines, Golden, CO, November, 1987 pp. 249-250.

33. Rangarajan V., N. Giallourakis, D.K. Matlock, and G. Krauss, "The Effect of Texture and Microstructure on Deformation of Zinc Coatings", J. Mater. Shap. Tech.,

Vol. 6, No. 4, 1989, pp. 217-227.

34. Sachs G. and K. VanHorn, Practical Metallurgy, ASM, Metals Park, Ohio, 1940, pp. 415-433.

35. Hallquist J.O., "Nike2D -- A Vectorized Implicit, Finite Deformation Finite Element Code for Analyzing the Static and Dynamic Response of 2-D Solids with Interactive Rezoning and Graphics", Lawrence Livermore National Laboratories, Report No. UCID-19677, Rev.1, December 1986

36. Doege E., "Prediction of Failure in Deep Drawing", Computer Modeling of Sheet Forming Processed, TMS, 1986, pp. 209-224.

37. Vallance D., "Analysis of Friction Behavior of Coated Sheet Steel using the Bending Under Tension Test", Master of Sceice Thesis No. T-3796, Colorado School of Mines, Golden, CO, Febuary 1990.

38. Swift, H.W., "Plastic Bending Under Tension", Engineering, Vol. 166, 1948, p. 333.

39. VanTyne C.J., Personal Communication Colorado School of Mines, Golden CO, 1989.

40. Safranek W.H., The Properties of Electrodeposited Metals and Alloys, Elsevier Publishing Company Inc., New York, 1982, pp 421-430.

41. Iwaya J., Y. Okano, and M. Miyahara, "A Study on the Friction Behavior of Coated Steel Sheet", Proc. of NADDRG Annual Meeting, November, 1989.

42. Ohwue T., K. Hashimoto, and M. Takita, "Sliding Behavior of Various Coated Steel Sheets in Room Temperature and Warm Working Condition", Proc. of NADDRG Annual Meeting, Novermber, 1989.

43. Vallance D., Personal Communication, Colorado School of Mines, Golden CO, Novermber, 1989.

44. Perry D., A. Jussiaume, and Y. Deleon, "Study of Damage Sustained by Precoated Sheet Steel During Deformation and the Effect of This on Resistance to Corrosion", Addendum to the Controlled Sheet Metal Processes of the

15th. Biennial Congress of the IDDRG, Dearborn, Michigan, 1988, pp .

45. Gronostajski J.Z., and W.J. Ali, "Analysis of Formability of Coated Steel Sheet at Complex Strain Paths", Proc. of the 15th. Biennial Congress of the IDDRG, Dearborn, Michigan, 1988 43-47.

46. Fuduzuka T., M. Urai and K. Wakawama, Kobe Steel Engineering Report, 33, 1980, pp.77-81.

47. Sudo C., T. Nakamori and M. Nishihara, Tetsu-to-Hagane, 66, 1980, pp. 73-81.

48. Nadamori T. and A. Shibuya, "Effects of Galvannealing Conditions and Coating Weight on Powdering Resistance of Galvannealed Steel Sheet", Corrosion Resistant Automotive Sheet Steels, World Materials Congress, Chicago Ill., September 1988, ASM, pp. 139-149.

49. Allegra L., R.G. Hart, and H.E. Townsend, "Intergranular Zinc Embrittlement and Its Inhibition by Phosphorus in 55 pct. Al-Zn-Coated Sheet Steel", Meetallurgical Transactions A, Vol. 14A, March 1983, pp

401-411.

50. Gallourakis N., D.K. Matlock and G. Krauss, "A Cryogenic Fracture Technique for Characterizing Zinc Coated Steels", Metallography, In press.